MODELING AND BEHAVIOR OF PRESTRESSED CONCRETE SPANDREL BEAMS

A DISSERTATION
SUBMITTED TO THE FACULTY OF THE GRADUATE SCHOOL
OF THE UNIVERSITY OF MINNESOTA
BY

Bulent Mercan

IN PARTIAL FULFILLMENT OF THE REQUIREMENTS
FOR THE DEGREE OF
DOCTOR OF PHILOSOPHY

Advisors:
Arturo E. Schultz and Henryk K. Stolarski

MAY 2011

Acknowledgements

I would like to acknowledge all of the people who have helped me in the completion of this dissertation. First and foremost, I would like to express my deepest gratitude to my advisors, Professors Arturo E. Schultz and Henryk K. Stolarski, for all of their guidance, advice, support and friendship. I have been incredibly fortunate to have advisors who gave me the freedom to discover on my own. I would also like to give a special thanks to Professors Perry H. Leo and Steven F. Wojtkiewicz for being on my committee and for their comments on this work. I would also like to thank all of the sources which provided me with the financial means to conduct my research. I am thankful to Department of Civil Engineering, University of Minnesota for the Sommerfeld Fellowship, and the Precast/Prestressed Concrete Institute for the Daniel P. Jenny Fellowship. Finally, I would like to thank my wife, Esra, for her encouragement and companionship during the preparation of this dissertation.

Dedicated to

my wife Esra

and my daughter Asya

Abstract

Spans for precast and prestressed concrete spandrel beams (or spandrels) are typically as long as 30 to 48 ft. In the near future, precasters might begin to produce spandrels with longer spans (up to 60 ft) and thinner webs (as little as 8 in.), which facilitate more cost-effective parking garages and advance the competitiveness of the precast concrete industry. However, there are likely to be spandrel dimensions beyond which excessive deformations make such designs unfeasible. In particular, lateral deformations developing at the top and bottom of a slender spandrel beam need to be investigated for short-term and long-term loading effects.

Spandrels in parking garages typically support double-tee beams (or double tees) on ledges, spot corbels, or pockets, all of which introduce lateral eccentricity as the double tee loads are transferred to the spandrels. Upon connecting the spandrels to the double tees using deck ties, these connections serve as lateral restraints for the spandrels due to the axial stiffness of the deck ties. Thus, lateral deflection of the spandrel is prevented at the connection points. However, given that the deck ties are thin steel plates, they are unable to eliminate twisting of the spandrel section. Thus, subsequent deformation of the spandrel will include both vertical and lateral deflections. Excessive lateral deflections might cause undesirable serviceability problems in the structure or even collapse of the concrete deck. For this reason the study of lateral deflections is the focus of the research presented in this dissertation.

Two approaches are pursued to study the lateral deflection response of the slender spandrels under static loads: analytical and computational. First, an approximate analytical solution for the lateral deflections of spandrels is presented. Next, the effects of various parameters on the results from finite element analyses are examined. This is followed by a detailed discussion of modeling suggestions under which computational results can be sufficiently reliable. The best possible modeling approach, deduced from such parametric studies, is used for a three-dimensional nonlinear finite element analysis

of spandrels. Finally, time-dependent (long-term) lateral deflections in spandrels having various span lengths and cross sections are investigated.

Table of Contents

List of Tables

List of Figures

CHAPTER 1

Overview

1.1. Problem Definition

Precast, prestressed concrete spandrel beams (or spandrels) have been widely used in the perimeter of precast concrete frame buildings, especially for parking ramps. The spandrels in parking garages usually support precast, prestressed concrete doubles-tee beams (or double-tees, which are used as deck beams, and are connected to column corbels at their ends. The spandrels are linked to the double tees using deck ties (i.e., welded steel plates) which serve as lateral restraints for the spandrels at the connection points. As the double tee loads are transferred to the spandrels, torsional effects are introduced due to eccentricity of loading. Given the fact that deck-ties are thin steel plates, they are unable to prevent twisting of the spandrel section entirely. The torsional loading, defined here as the product of the vertical loads from the double tees, P, and the eccentricity, e, (Fig. 1.1), interacts with the flexural loading to generate a complex pattern of deformation that includes vertical and lateral deflections, as well as twisting of the spandrel section. The presence of prestressing forces creates an even more complicated deformation pattern, which is difficult to capture in a single analytical formula.

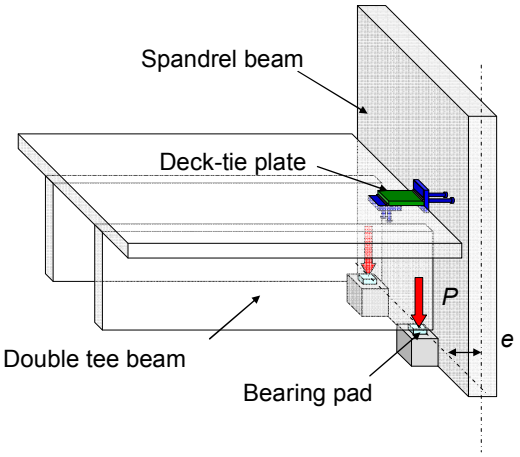

Fig. 1.1. Spandrel beam segment supporting a double tee beam

To date, most research efforts have been focused on strength design considerations for precast prestressed concrete spandrels under the combined effects of shear, torsion and

bending. Nevertheless, lateral deformation issues in these structural members have not been adequately addressed in the technical literature. Lateral deformations reduce the bearing length for the double tee supports as the bottom of the spandrel moves out (deflects laterally away from the double tee), leading to collapse of the double tees in extreme cases (Fig. 1.2). Under service conditions, unsightly distortion of the top of the spandrel might occur or the glazing assembly for the exterior of the building might be defected as the spandrel tilts inward (deflects laterally toward the double tee). Creep and shrinkage of the concrete further complicate the state of deformation, and after supporting dead loads for a sustained period of time, the magnitude of total deformations increases well above the values generated upon immediate loading. A comprehensive assessment of such deformations, as well as the parameters that affect them, has been undertaken in this thesis.

(a) Partial collapse

(b) Close-up of the failure

Fig. 1.2. Parking ramp collapse (WCNC website, Charlotte Local News Station)

1.2. Methods

From the experimental and analytical data available in literature, no information on the lateral deflection response of prestressed concrete spandrel beams can be inferred. In this regard, finite element analyses might provide opportunities for better understanding the overall behavior of these members. However, in spite of huge progress in the area of computer analysis of concrete structures, it still appears dangerous to rely on computer models alone. To study the behavior of spandrel beams relying solely on computer

simulations, it is essential to first calibrate and verify these simulations with experimental results and next have a detailed understanding of those models and their sensitivity to the parameters involved. Only then can computer simulations alone be the basis for studying behavior of concrete structures, including spandrel beams.

A slender spandrel beam might develop large deformations that affect internal equilibrium under combined loading effects, as a result small deflection theory is likely to lead to inaccurate estimation of the maximum load and deflections. Therefore, due to the nature of the problem, the finite element model should incorporate geometric nonlinearity. Material nonlinearity is another factor that needs to be considered in the finite element analysis. Concrete cracking reduces both torsional and flexural stiffness of the section and causes a significant increase in the deflections. The prestressing forces, however, tend to keep concrete uncracked under flexure. Still, the possibility of cracking cannot be excluded and a relatively accurate material model for concrete should be used to capture concrete cracking and corresponding deformations. Including all of those features in the analysis can only be accomplished using a computational approach, as practicing engineers, as well as most researchers, have to rely on commercially available computer programs. The ABAQUS finite element analysis software [1] is one of the programs capable of solving highly nonlinear problems. It provides a complex material model (damage-plasticity model) for concrete that includes crushing in compression and cracking in tension. The behavior of concrete in this model is defined with various parameters such as dilation angle, fracture energy, and tension stiffening.

A recent experimental investigation on precast, prestressed concrete spandrel beams has been conducted at North Carolina State University to elucidate resistance mechanisms in the spandrels and investigate the detailing of torsional reinforcement [2]. This unique study of full-scale spandrels is quite comprehensive in terms of geometry and loading, but it primarily addressed the configuration of transverse reinforcement and it focused on the 45-ft long spandrels under short-term loading. There are a few research efforts that investigate the response of prestressed concrete spandrel beams through finite element simulations [3]. However, those efforts are fine-tuned to justify the accompanying experimental results, and are difficult to reproduce due to the large

sensitivity of the results to the values of the parameters used in the model. Therefore, in spite of their importance, the conclusions from these valuable studies cannot be used directly to address lateral deformations in the spandrel beams.

1.3. Study Objectives

The major objectives of this study are to obtain realistic estimates of short-term and long-term deformations in the precast and prestressed concrete spandrel beams, to gain an understanding of the parameters that affect them, and to develop simplified methods of analyses that are potentially useful in design practice. To achieve these objectives, comprehensive finite element models were developed using a well-known software package, ABAQUS, which include realistic representation of spandrel geometry, loading configuration, material behavior and support conditions.

1.4. Overview of Dissertation

The dissertation is divided into five chapters describing analytical and computational studies related to the behavior of precast and prestressed concrete spandrel beams. Following this introductory chapter, approximate analytical solutions for predicting maximum lateral deflections in laterally restrained and unrestrained spandrel beams under eccentric loads are presented in Chapter 2. An equivalent loading method is proposed in order to simplify the governing differential equations of the problem. Numerical results from three-dimensional finite element analyses are also presented and found to be in close agreement with those of the proposed analytical method.

Chapter 3 investigates the major principles that should be incorporated for finite element modeling of concrete structures using the commercial software, ABAQUS. For this purpose, several finite element models are generated with concrete models embedded in the program and verified with experimental results selected from literature. The first verification study is related to the behavior of plain concrete under uniaxial tension. Next, the modeling of plain concrete under biaxial loading is discussed. The final verification example concerns the pure bending of conventionally reinforced concrete beams.

Chapter 4 focuses on nonlinear three-dimensional finite element modeling of precast, prestressed concrete spandrel beams. The numerical results obtained using ABAQUS are verified with experimental results available in the literature. The sensitivity of the spandrel beam response to various modeling parameters such as finite element type, dilation angle, fracture energy, tension stiffening, bearing stress distribution and support representation is presented.

In Chapter 5, the arc-length and explicit dynamic solution methods for nonlinear finite element analysis of prestressed concrete spandrel beams subjected to monotonically increasing loads are discussed. These two solution methods are arguably the best approaches for analysis of strongly nonlinear problems. They are compared in this chapter for numerical convergence properties, computational effort, and quality of the results. A resulting set of recommendations for the modeling of prestressing forces in the explicit dynamic and arc-length solution procedures is given.

In Chapter 6 the long-term deflection behavior of slender, percast and prestressed concrete spandrel beams is investigated. A numerical study is conducted involving a series of nonlinear finite element analyses of L-shaped and pocket spandrels for different span lengths (48 and 60 ft) and web thicknesses (8, 9, and 10 in.). All spandrels are modeled using realistic reinforcement and prestressing strand details. The sensitivity of long-term deflections in spandrels to various material and structural properties such as spandrel type, span length, beam width, concrete curing method, the level of long-term effects, loading eccentricity and magnitude is presented.

1.5. Overall Conclusions

The original contribution of this research to the overall knowledge of the behavior of prestressed concrete spandrel beams is the incorporation of lateral deflection issues to this topic, which is very important for the integrity of structures using spandrel beams and has not been addressed in previous research adequately. To this end, three-dimensional finite element modeling techniques for the prediction of lateral deflections in spandrels are employed. The sensitivity of the spandrel response to various modeling parameters is

extensively investigated. The findings and contributions can be listed as follows:

- A simple closed-form approximate solution for the maximum lateral deflection and angle of twist in eccentrically loaded rectangular beams is proposed and found to be adequate in analysis of some designs. In particular, the results for spot-corbel and pocket type spandrels are in good agreement with those of proposed analytical solutions.
- The results from three-dimensional finite element analyses of precast, prestressed concrete spandrels under vertical loading are found to be sensitive to several input parameters. Those include the type of element, the dilation angle for the concrete, bearing stress distribution at the supports, and deck-tie stiffness. For those reasons commercial computer programs have to be used with caution when employed in the analysis of problems with the material behavior as complex as those of concrete.
- The arc-length and explicit dynamic methods, two viable approaches, are used for the finite element analysis of geometrically and materially nonlinear problems, such as the prestressed concrete spandrel beams. The arc-length method provides more accurate results, but experiences convergence problems depending upon the choice of mesh configuration and the selection of concrete post-cracking response parameters. The explicit dynamic solution procedure provides acceptable solutions in cases when the arc-length approach fails, however solution accuracy may be slightly lower and computation effort may be significantly larger. Overall, the experience gained in the course of this research suggests that the arc-length method is preferable as long as the solution converges and required especially for the deflection responses including snap-backs and significant strength degradation.
- Three-dimensional finite element models of a series of prototype spandrels in various span lengths and thickness, including realistic reinforcement and strand details, are generated using ABAQUS for the long-term deflection study. The analysis results showed that the maximum lateral deflections in the long (60-ft) spandrel beams at the end of two years for total loads equal to the dead and fifty-percent of live loads are always less than L/500. This conclusion should guide the design of the details necessary to safely support the double tees.

CHAPTER 2

Elastic Solutions for Eccentrically Loaded, Slender, Rectangular Spandrel Beams

2.1. Introduction

Spandrel beams in precast concrete buildings are widely used to support double-tee deck beams, particularly in parking garages. Spandrel beams of deep cross sections, resisting eccentric loads from double-tee beams, can be susceptible to excessive lateral deformations and serviceability failures before reaching their strength limits. However, closed-form solutions for estimating lateral deflections in such members are not available in the technical literature. In this chapter, approximate analytical solutions for the deflection of beams with thin rectangular sections are derived from second order elastic analysis, and they are proposed for use in estimating maximum lateral deflections in spandrel beams under eccentric and uniformly distributed loads. Continuous lateral support is provided at the elevation of the floor deck in spandrel beams, thus two cases are considered, one for laterally restrained beams under typical service conditions, and a second for laterally unrestrained beams prior to the establishing the floor deck connections, or if those connections fail during extreme loading. An equivalent loading method is proposed to obtain the approximate analytical solutions, in which the differential equations of equilibrium governing the problem are simplified by replacing the actual loading in the spandrel beams with a substitute loading. Numerical solutions are also obtained from three-dimensional finite element analyses, and their results are found to be in close agreement with those of the analytical solutions for two of the three common types of load-bearing precast, prestressed concrete spandrel beams.

2.2. Background

Precast and prestressed concrete spandrel beams (Fig. 2.1) are usually used in the perimeter of precast concrete buildings, particularly in parking garages, to support precast double-tees serving as deck beams. There are three common types of spandrel beams depending upon the manner in which the double tees are supported; spot-corbel spandrels (Fig. 2.1.a) with discontinuous ledges, L-shaped spandrels with continuous ledges (Fig.

2.1.b) and pocket spandrels (Fig. 2.1.c) with rectangular cutouts. Of these types, the L-shaped spandrel was the first to be used on a regular basis, but the next generation of longer spandrels (spanning up to 60 feet (18.3 m)), often utilizes the pocket or corbel types to minimize weight, and in the case of the pocket corbel, to minimize the eccentricity of vertical loads. The spandrel beam resists eccentric loading which stems from vertical double-tee loads acting through the horizontal offsets provided by corbels or pockets. Simple vertical support is provided to spandrel beams at their soffits by the column corbels. Torsional restraint is provided at the ends of the spandrels by an additional connection to the columns by means of threaded inserts (i.e., tie-back bolts) at two elevations above the column corbels and which prevent twisting of the spandrel ends. The load bearing spandrel beam is also laterally restrained along the mid-height level of its web by spandrel-to-double-tee connections (i.e., deck tie plates). Given that these connections are made of thin welded steel plates, they cannot provide any restraint against twisting of the spandrel.

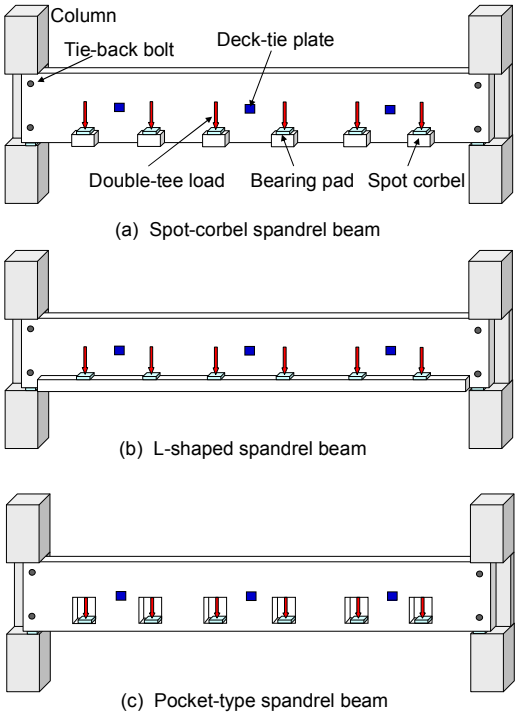

Fig. 2.1. Precast and prestressed concrete spandrel beams

2.3. Previous research

Study of the interaction of and design for combined shear, torsion and bending in reinforced or prestressed concrete flexural members is well-established [4]-[6]. However, this work has focused on stress and strength design considerations, and mention is seldom made of lateral deflection and serviceability of these flexural members. Only a limited amount of research on the stability of tall, slender 'reinforced' concrete beams is found in the technical literature, including experimental studies from the 1950s and 1960s conducted in the U.S. [7]-[9] and more recent ones [10]-[12]. However, all of these studies aimed at exploring the lateral instability of concentrically loaded reinforced concrete beams. Historically, lateral deflections have often been ignored in the design of precast and prestressed concrete spandrel beams, as well as many other concrete members, since they are assumed to be too stocky for lateral instability to supercede stress or force considerations. However, due to technological improvements and industry needs, a new generation of longer spandrel beams (up to 60 ft (18.3m)) with thinner webs (as little as 8 in. (203mm)) are being introduced to the market. Based on this current trend, lateral deflections for slender spandrel beams need to be evaluated.

Analytical solution for maximum lateral deflections in elastic beams with thin rectangular sections requires the establishing of governing differential equations of equilibrium. To this end, the differential equations for the lateral-torsional buckling problem in concentrically loaded elastic beams, which are homogenous, isotropic and prismatic, can be used. The solution reported by Timoshenko in 1936 [13] is well known [14]-[17]. The differential equations of equilibrium can be easily extended to include torsional effects and solved to obtain expressions for lateral deflection and angle of twist.

Linearly elastic material behavior is often assumed for prestressed concrete members under service loads, but the actual response of concrete to larger load regimes is highly nonlinear. Prestress in concrete usually eliminates or significantly reduces tensile stresses in the members under service loads, thus enhancing the resistance to cracking. However, concrete exhibits a nonlinear stress-strain relationship for compressive stresses greater than about one-half of its compressive strength, so a reduced modulus of elasticity E_r can be used to represent compression softening (i.e., plasticity) in concrete when using

linear, elastic material models. Sant and Bletzacker [8] recommend a reduced modulus E_r equal to $0.687E_c$ to account for concrete compression softening in tall, slender reinforced concrete beams.

In this work, second-order elastic analyses were conducted to evaluate lateral deflections and angle of twist in restrained and unrestrained rectangular beams subjected to eccentric vertical loading. Finding the closed-form solution to the differential equations governing this problem was not possible. Therefore, an equivalent loading procedure was proposed which simplified the governing differential equations to obtain approximate expressions for deflection and angle-of-twist. Finally, analytical results were verified with those obtained from the nonlinear finite element analyses of typical spandrel beams.

2.4. Lateral restraints with deck-tie plates

Load-bearing spandrel beams typically have deck-ties placed discretely along its span length to provide a lateral connection between spandrel and double tees (Fig. 2.2). However, in practice, some engineers do not rely on the deck-ties to provide reliable lateral support for spandrel beams. There are valid reasons for this; first, the ties are not proportioned to meet an engineering design goal (e.g., ensuring sufficient strength to avoid failure under expected maximum lifetime loads or accidental loads); second, deck-tie stress/force or strain/displacements requirements are not computed; third, the influence of cyclic loading on fatigue life is not considered; fourth, adequate protection from corrosion may not always be provided; so the ability of these connections to provide reliable lateral connection between spandrel and double-tees is not known.

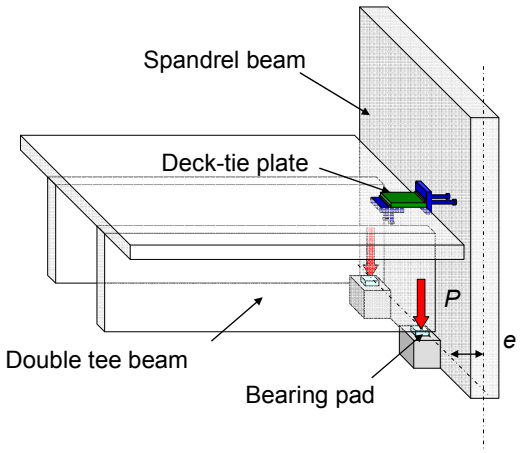

Fig. 2.2. The spandrel-to-double-tee connection

A typical deck-tie connection, as illustrated in Fig. 2.2, is built on site by welding a steel plate to two other steel elements (e.g., plates or angles) which are embedded into the spandrel web and the double-tee flange in the precast plant. Deck-ties connecting the spandrel web to the double-tees are often placed near the neutral axis elevation of the spandrel section, in which case they do not restrain twisting deformations. However, once these connections are established, the pattern of lateral deflections changes since the beam cannot deflect laterally at the level of the double tee connections as long as the deck-tie welds are intact. Yet, the welding of the deck-tie plates does not take place immediately upon placing the double tees. So, there is a risk in relying on these connections while the structure is being erected if unexpected loading occurs. Moreover, high-cycle fatigue (from vehicle loading), low-cycle fatigue (from extreme loading), stresses from volumetric effects (temperature, creep and shrinkage of concrete) and corrosion raise further doubts on the reliability of the deck-tie connections. Regarding the case of extreme loading, recent analytical and experimental research suggests that the deck tie connections would fail at early stages of seismic loading in a typical parking garage diaphragm [18]. Therefore, the lateral deflection of a spandrel beam should be investigated for two idealized cases (Fig. 2.3); (a) the unrestrained beam and (b) the restrained beam. In the latter, lateral deformations are prevented by the deck-ties installed at the mid-height of the spandrel along its span length.

In extreme cases of large twisting angles, the supports of the double tees can be lost,

leading to the collapse of the structure. Fig. 2.3 shows the deformed shapes of spandrel webs of restrained and unrestrained beams. If the lateral deflection at the bottom of the restrained beam is larger than the overlap distance at the bearing pad (Fig. 2.2), the double-tee beams can slip off the spandrel ledge (or pocket or corbel) and collapse. There is less likelihood of such collapse mechanism for laterally unrestrained beams since lateral deformations are often directed toward the double-tees. Still, unrestrained beams can experience large lateral deflections before reaching their design capacities and fail to satisfy deflection serviceability requirements.

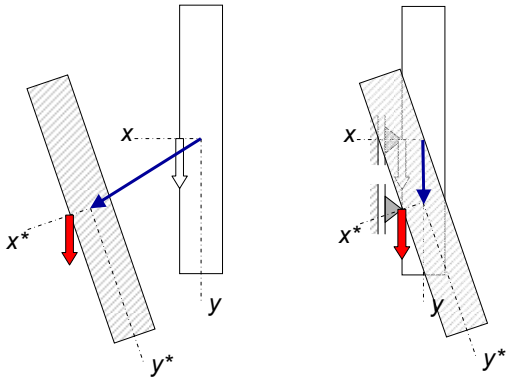

(a) Unrestrained beam (b) Restrained beam

Fig. 2.3. Deformations of laterally restrained and unrestrained beams (double-tee beams align in the positive *x*-axis and the positive deflections are inward)

2.5. Laterally unrestrained and concentrically loaded beams

In general, slender elastic beams with deep and narrow rectangular cross sections do not experience lateral deflections when concentric vertical loads (i.e., without lateral eccentricity producing torsion) are resisted. At a critical load (buckling load), slender beams undergo sudden large lateral deformations through the phenomenon known as combined lateral and torsional buckling. This type of instability likely occurs when the flexural rigidity of a beam in the plane of bending is significantly larger than that in the out-of-plane direction. The theory of lateral-torsional buckling of slender beams under concentric loads is well known and has been extensively investigated for steel beams [14]-[17]. Before considering the behavior of eccentrically loaded beams, a short

discussion on concentrically loaded beams is necessary for several reasons; (a) differential equations of equilibrium derived for a concentrically loaded beam can be easily extended to the case of an eccentrically loaded beams, (b) the use of the buckling load parameter in the derivations will significantly simplify the analytical expressions, and (c) the influence of eccentric loading on the lateral response will be more meaningful when it is compared with the response of a concentrically loaded beam.

A deep and narrow rectangular beam subjected to strong-axis bending-moment couples M_o at the ends becomes unstable, deforms laterally and twists, as depicted in Fig. 2.4.a, when the moment M_o attains a critical value M_{cr}. In order to determine the critical buckling moment, governing equilibrium equations are established for a slightly deformed shape (or buckled shape) of the beam. The smallest value of M_o that maintains the equilibrium of the beam in such buckled shape is equal to the critical value of buckling moment M_{cr}.

The global and local coordinate axes, x-y-z and x^*-y^*-z^*, respectively, are selected, as shown in Fig. 2.4.a. The vertical deformation of the centroid of the beam cross section v, the lateral deformation u, and the angle of twist ϕ are defined in the buckled shape of the beam, as illustrated in Fig. 2.5. The angle of twist ϕ is assumed to be positive when the cross section rotates from the x- to the y-axis, or when the rotation vector defined using 'right-hand rule' is parallel to the positive direction of z. The deformations, u, v, and ϕ, are very small and, thus, higher-order terms will be neglected. The governing differential equations of equilibrium are established in the buckled shape of the beam. Therefore, the curvatures of the centerline of the beam in y^*z^*- and x^*z^*- planes and the moments M_{x^*}, M_{y^*}, and M_{z^*}, are required. The positive directions of internal moments are shown in Fig. 2.4.b. Since the angle of twist is very small, the curvatures in the y^*z^*- and x^*z^*- planes are assumed to be equal to the curvatures in the xz- and yz-planes (i.e., d^2u/dz^2 and d^2v/dz^2, respectively). Likewise, only the dominant terms of the components of M_x (or M_o) in the local coordinate axes, x^*-y^*-z^*, are retained in the transformation from x-y to x^*-y^* as seen in Fig. 2.6.

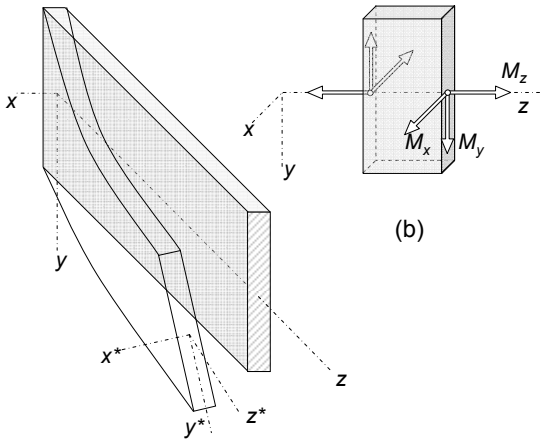

Fig. 2.4. (a) Global and local coordinate systems and (b) sign convention for positive internal moments

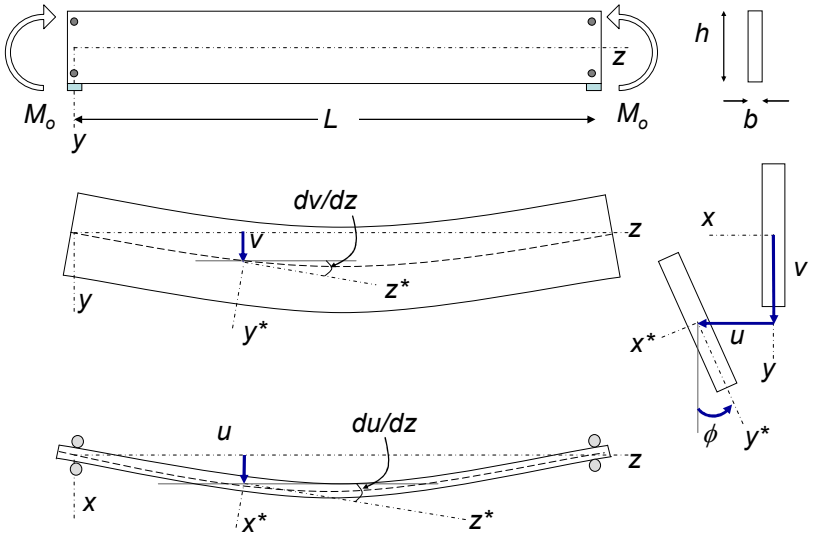

Fig. 2.5. Deformations in x-y, y-z and z-x planes

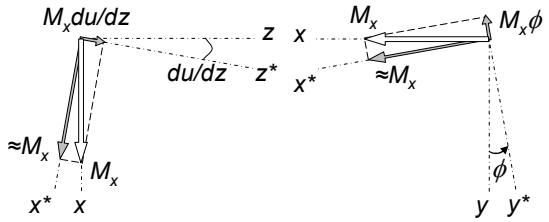

Fig. 2.6. Components of bending moment *Mx* along local axes, *x*,y** and *z**

This leads to the differential equations of equilibrium in the form:

$$-EI_x v'' = M_{x*} \cong M_o \tag{1}$$

$$EI_y u'' = M_{y*} \cong -\phi M_o \tag{2}$$

$$GJ\phi' = M_{z*} \cong u' M_o \tag{3}$$

where E is the modulus of elasticity; I_x is the moment of inertia of the beam section about the strong-axis of bending; I_y is the moment of inertia about the weak-axis; G is the shear modulus of elasticity; J is the torsional constant for the beam section. The warping torsional resistance is negligible for beams with deep and narrow rectangular cross-sections and so the warping effect does not appear in Eq. (3). Note that lateral torsional buckling involves torsion even though there is no torsional loading. The internal torsional moment arises as a second-order effect (i.e., a component of the deformation pattern) and hence Eq. (3) is necessary. Equations (2) and (3) are coupled through the angle of twist ϕ. After simplification, a second-order linear differential equation for the angle of twist ϕ with constant coefficient can be obtained. The solution of this differential equation gives the critical buckling value (M_{cr}) of the end moments M_o:

$$M_{cr} = \frac{\pi}{L}\sqrt{EI_y GJ} \tag{4}$$

Eq. (4) is derived for the loading case of equal and opposite end moments. For cases with moment gradient, the critical moment can be adjusted using the bending coefficient C_b, based on approximate expressions [17]. The coefficient C_b is equal to unity for uniform bending (i.e., equal end moments) and 1.13 for uniformly distributed vertical loads. Incorporating the C_b factor, the critical moment given by Eq. (4) becomes:

$$M_{cr} = C_b \frac{\pi}{L}\sqrt{EI_y GJ} \tag{5}$$

2.6. Laterally unrestrained and eccentrically loaded beams

In order to investigate the influence of eccentric loading on the lateral deflection of spandrel beams, a simplified structural system (Fig. 2.7.a) comprising a slender beam with rectangular cross section is subjected to uniformly distributed load q with an

eccentricity e. The bending moment M_x has a parabolic distribution along the span length, $M_x=(qL^2/2)[z/L-(z/L)^2]$. Due to the torsionally fixed supports, as well as the symmetry of the beam and loading pattern, the torsional reactions at the ends ($M_T=qeL/2$) are equal, but in opposite directions. The distribution of internal torsion along the length of beam is a linear function of z, $M_z = M_T(1-2z/L)$, with the left end of the beam undergoing positive torsion.

Timoshenko's solution does not explicitly address beams with torsional loading (i.e., lateral eccentricity), but the the governing differential equations can be extended to include torsional loading. The components of the torsion along the x^*, y^*, and z^* axes in the deformed position must be included in the three moment equilibrium equations, Eqs (1), (2), and (3). As illustrated in Fig. 2.7.b, a positive beam slope du/dz in the horizontal x-z plane produces a torsional component $M_z\, du/dz$ in the local x^* axis which is negative according to the sign convention described in Fig. 2.4.b. Thus, positive torsion M_z acting through a positive horizontal slope du/dz generates a negative moment contribution for x-axis equilibrium in Eq. (1). Similarly, in Fig. 2.7.b, a positive beam slope dv/dz in the vertical y-z plane produces a torsional component $M_z\, dv/dz$ in the local y^* axis which opposes positive bending as indicated in Fig. 2.4.

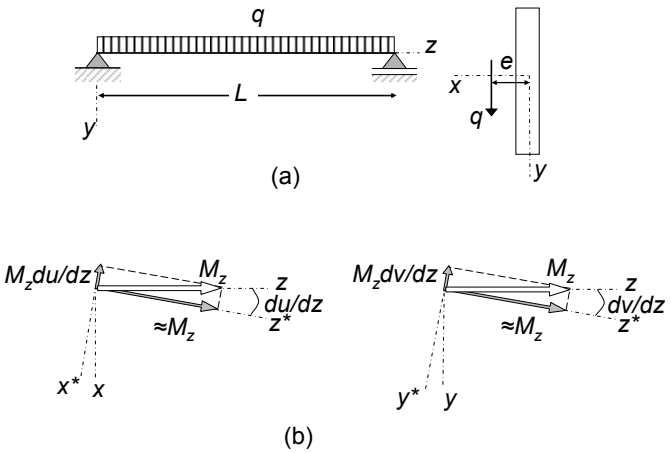

Fig. 2.7. (a) Laterally unrestrained beam under eccentric loading and (b) components of moment M_z in the local axes

Thus, positive torsion M_z acting through a positive vertical slope dv/dz produces a negative moment contribution for y-axis equilibrium in Eq. (2).

$$-EI_x v'' = M_x - u'M_z \tag{6}$$

$$EI_y u'' = -\phi M_x - v'M_z \tag{7}$$

$$GJ\phi' = u'M_x + M_z \tag{8}$$

The case of a laterally unrestrained beam under eccentric loading introduces a parabolic function of length z for bending moment M_x and a linear function of z for torsion M_z, which makes coefficients of Eqs. (6), (7), and (8) variable. As a result, closed-form solution of Eqs. (6), (7), and (8) becomes difficult, if not impossible. Still, an approximate closed-form solution can be found if the actual loading in the beam is replaced with an equivalent loading, shown in. Fig. 2.8 The actual loading (Fig. 8.a), uniformly distributed load q acting over an eccentricity e, is replaced by a substitute loading (Fig. 8.b), end moments M_o ($=q_oL^2/8$) and a uniformly distributed torque mo modified by the load parameter q_o, ($q_o=q/C_b$ where C_b is the bending coefficient mentioned above). The assumed moment Mo in the substitute loading ensures the same maximum value for the actual loading condition. The substitute loading yields a differential equation of equilibrium with constant coefficients and enables an closed-form solution. The accuracy of the substitute loading approach will be investigated later by means of numerical analysis.

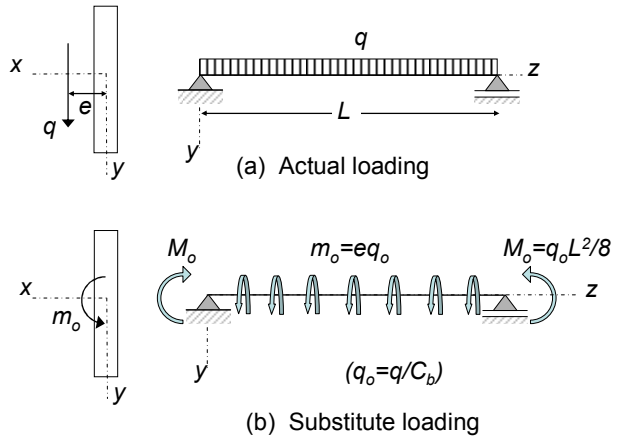

Fig. 2.8. Actual and equivalent loadings for laterally unrestrained beam

The differential equations can be simplified by neglecting the last terms of Eqs. (6) and (7), ($-M_z du/dz$ and $-M_z dv/dz$), due to the fact that the torsional moment M_z is

generally very small relative to M_o. Under this condition, for the case of laterally unrestrained and eccentrically loaded beam (with the equivalent loading), the differential equations of equilibrium are:

$$-EI_x v'' = M_o \tag{9}$$

$$EI_y u'' = -\phi M_o \tag{10}$$

$$GJ\phi' = u' M_o + \frac{eq_o L}{2}\left(1 - 2\frac{z}{L}\right) \tag{11}$$

Solving Eq. (10) for ϕ and substituting its derivative $d\phi/dz$ into Eq. (11), we find

$$u''' + u' \frac{(M_o)^2}{EI_y GJ} = -\frac{eq_o L}{2}\left(1 - 2\frac{z}{L}\right)\frac{M_o}{EI_y GJ} \tag{12}$$

Considering Eq. (4)

$$M_{cr} = \frac{\pi}{L}\sqrt{EI_y GJ},\ M_o = \frac{q_o L^2}{8},\ \text{and}\ \alpha = \frac{M_o \pi}{M_{cr} L} \tag{13}$$

Eq. (12) is transformed into

$$u''' + \alpha^2 u' = -4\alpha^2 \frac{e}{L} + 8\alpha^2 \frac{e}{L}\frac{z}{L} \tag{14}$$

The solution of equation (14) gives the following formula for the lateral deflection u as a function of the position z along the beam.

$$u(z) = A_1 \cos(\alpha z) + A_2 \sin(\alpha z) + A_3 + 4\frac{e}{L}\left(\frac{z^2}{L} - z\right) \tag{15}$$

The constants, A_1, A_2 and A_3, are obtained using the following boundary conditions; $u(0) = \phi(0) = 0$ and $u'(L/2) = 0$.

Considering that

$$\phi = -\frac{EI_y}{M_o}u'' = \frac{EI_y}{M_o}\left(A_1\alpha^2 \cos(\alpha z) + A_2\alpha^2 \sin(\alpha z) - 8\frac{e}{L^2}\right) \tag{16}$$

the constants, A_1, A_2 and A_3, can be determined:

$$z = 0,\ \phi = 0,\ \frac{EI_y}{M_o}\left(A_1\alpha^2 + 0 - 8\frac{e}{L^2}\right) = 0,\ A_1 = \frac{8e}{\alpha^2 L^2} \tag{17}$$

$$z = 0,\ u = 0,\ \frac{8e}{\alpha^2 L^2} + 0 + A_3 + 0 = 0,\ A_3 = -\frac{8e}{\alpha^2 L^2} \tag{18}$$

$$z = \frac{L}{2},\ u' = 0,\ -\frac{8e}{\alpha^2 L^2}\alpha \sin(\alpha L/2) + A_2 \alpha \cos(\alpha L/2) + 0 = 0,\ A_2 = \frac{8e}{\alpha^2 L^2}\tan(\alpha L/2) \tag{19}$$

From Eqs. (15), (16), (17), (18), and (19) the following formulas for u and ϕ are obtained.

$$u = \frac{8e}{\alpha^2 L^2}\cos(\alpha z) + \frac{8e}{\alpha^2 L^2}\tan(\alpha L/2)\sin(\alpha z) - \frac{8e}{\alpha^2 L^2} + 4\frac{e}{L}\left(\frac{z^2}{L} - z\right) \tag{20}$$

$$\phi = \frac{EI_y}{M_o}\frac{8e}{L^2}\left(\cos(\alpha z) + \tan(\alpha L/2)\sin(\alpha z) - 1\right) \tag{21}$$

Loading and geometry is symmetric with respect to the midspan of the beam. Thus, in order to get the maximum lateral deflection parameter u_m for this laterally unrestrained beam, we substitute z=L/2 in Eq. (20), obtaining

$$u_m = e\left(\frac{8}{\alpha^2 L^2}\frac{1}{\cos(\alpha L/2)} - \frac{8}{\alpha^2 L^2} - 1\right) \tag{22}$$

Introducing the parameters in equations (13), into Eq. (22), maximum lateral deflection u_m of the centroidal section at midspan of the beam can be written as

$$u_m = u\left(\frac{L}{2}\right) = e\left\{\frac{8/\pi^2}{(M_o/M_{cr})^2}\left[\sec\left(\frac{\pi}{2}\frac{M_o}{M_{cr}}\right) - 1\right] - 1\right\} \tag{23}$$

while the maximum angle of twist ϕ_m is

$$\phi_m = \phi\left(\frac{L}{2}\right) = 2\frac{e}{L}\frac{1}{M_o/M_{cr}}\left[\sec\left(\frac{\pi}{2}\frac{M_o}{M_{cr}}\right) - 1\right] \tag{24}$$

The above expressions will be used later to reveal the relationship between the maximum lateral deflection and the bending moment for various values of eccentricity.

2.7. Laterally restrained and eccentrically loaded beams

Here we assume that regularly-spaced deck-ties along the length of a spandrel beam provide a nearly continuous support sufficient to prevent lateral displacements at the mid-height level of the spandrel as long as the connections remain intact. However, the beam is free to rotate around the horizontal line of the deck-ties. In the case of a deep beam

subjected to eccentric loading, such twisting deformation may result in large lateral displacements at the top and bottom of the beam section, which may put the safety of the structure at risk. Therefore, the maximum lateral deflection in a laterally restrained beam under eccentric load (Fig. 2.9.a) is analyzed herein.

Unlike unrestrained beams, laterally restrained beams are subjected to horizontal reaction forces at their lateral supports, yielding a weak axis bending moment M_y along their span length. The moment M_y is unknown at the beginning of the analysis and varies along the length of the beam. To obtain the governing differential equations of equilibrium for this case, we first determine the components of the bending moment vector M_y in the x^*, y^*, and z^* coordinate system, as shown in Fig. 2.9.b, and then add them to the differential equations of equilibrium Eqs (6), (7), and (8), previously derived for the case of laterally unrestrained beams.

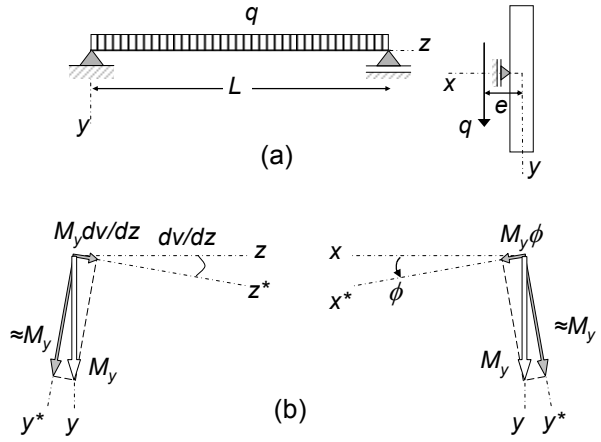

Fig. 2.9. (a) Laterally restrained beam subjected to eccentric loading and (b) components of moment M_y in the local axes

Thus the differential equations of equilibrium for restrained beams are

$$-EI_x v'' = M_x - M_z u' + M_y \phi \tag{25}$$

$$EI_y u'' = -M_x \phi - M_z v' + M_y \tag{26}$$

$$GJ\phi' = M_x u' + M_z + M_y v' \tag{27}$$

An approximate solution of this problem can be obtained by neglecting higher order terms; $M_z u'$, $M_y \phi$, $M_z v'$, and $M_y v'$. In general, M_y and M_z are relatively small compared to

M_x (or M_o) and their products with the slopes (i.e., *du/dz* and *dv/dz*) or the angle of twist ϕ are even smaller. While these assumptions are introduced to obtain an approximate closed form solution (verified later by finite element analyses), their introduction can be also rationalized on physical grounds. Namely, for laterally restrained beams, lateral curvature and thus lateral bending moment are small. Also, the moment M_x is dominant in comparison with M_z. Further simplification can be made using the substitute loading approach, which was previously described for the case of unrestrained beams. The lateral deflection *u* disappears in the differential equations since it is fixed by deck-ties close to the centroidal axis of the beam (true only if deck ties are close to the centroidal elevation). Under these assumptions, the differential equations become

$$-EI_x v'' = M_o + M_y \phi \tag{28}$$

$$M_y = M_o \phi \tag{29}$$

$$GJ\phi' = \frac{eq_o L}{2}\left(1 - 2\frac{z}{L}\right) \tag{30}$$

We emphasize here that M_y is an unknown function, which defines the variation of the weak axis bending due to the reaction forces at the lateral supports.

Integrating Eq. (30) with respect to *z*, and considering that ϕ=0 at *z*=0, we find

$$\phi = \frac{eq_o L}{2GJ}\left(z - \frac{z^2}{L}\right) \tag{31}$$

The angle of twist attains its maximum value ϕ_m at the mid-span of the beam and is equal to

$$\phi_m = \frac{eq_o L^2}{8GJ} \tag{32}$$

With the notation specified in equations (13), one has

$$\phi_m = \frac{eM_o}{GJ} = \frac{eM_o}{M_{cr}}\frac{\pi}{L}\sqrt{\frac{EI_y}{GJ}} \tag{33}$$

Assuming G=0.4E, J=hb^3/3 and I_y=hb^3/12 in the equation above, we find the approximate value of the maximum angle of twist

$$\phi_m = 2.5 \frac{e}{L} \frac{M_o}{M_{cr}} \tag{34}$$

2.8. Bending moment-lateral deflection curves

In the previous discussion of laterally unrestrained beams, the maximum lateral deflection u_m of the centroidal line of the beam was calculated. However, the additive effects of lateral translation and twist create the largest lateral deflection, u_{mt}, at the top of the spandrel (see Fig. 2.3a), For serviceability considerations, it is necessary to find the magnitude of the maximum deflection. Considering that deformation of the analyzed beam involves twist, the lateral deflections vary linearly along the depth of the beam. To describe this variation, the top (u_{mt}) and bottom (u_{mb}) deflections are computed

$$u_{mt} = u_m + \phi_m \frac{h}{2} \;\; and \;\; u_{mb} = u_m - \phi_m \frac{h}{2} \tag{35}$$

where h is the height of the cross section. The maximum lateral deflection occurs at the top of the mid-span section and its magnitude can be calculated using the following equation, derived by substituting Eqs. (23) and (24) in Eq. (35).

$$u_{mt} = u_m + \phi_m \frac{h}{2} = e \left\{ \frac{\left[\sec\left(\frac{\pi}{2} \frac{M_o}{M_{cr}} \right) - 1 \right] \left[\frac{8/\pi^2}{M_o / M_{cr}} + \frac{h}{L} \right]}{M_o / M_{cr}} - 1 \right\} \tag{36}$$

However, in the case of restrained beams, lateral deflections at mid-height are not possible. Therefore, due to twisting of the beam (Fig. 2.3), lateral deflections are developed at the top and bottom of the section (i.e., u_{mt} and u_{mb}). These deflections are equal, but in opposite directions and computed as follows:

$$u_{mt} = \phi_m \frac{h}{2} \;\; and \;\; u_{mb} = -\phi_m \frac{h}{2} \tag{37}$$

Using Eq. (34), derived for the angle of twist at the mid-span of the beam, the maximum lateral deflections at the top and bottom of the cross section of a restrained beam are:

$$u_{mb} = -\phi_m \frac{h}{2} = e\left(-1.25\frac{M_o}{M_{cr}}\frac{h}{L}\right) \tag{38}$$

Using Eqs. (36) and (38) with the height-to-length ratio h/L=0.11, relationships between maximum lateral deflections (u_{mt} and u_{mb}) and bending moment M_o for laterally unrestrained and restrained beams subjected to eccentric loading are shown in Fig. 2.10 for values of eccentricity ratios e/L equal to 0.002, 0.007, and 0.015. Positive deflections u_{mt} occur for laterally unrestrained beams, which means that beams move toward the double-tees. These curves, on the positive region of the graph, illustrate the high sensitivity of the unrestrained beam to the eccentricity of the load, with lateral deflection, u_{mt}, growing in an unbounded manner as the critical value for bending moment M_{cr} is approached. However, M_{cr}, which corresponds to the horizontal asymptote for the family of curves shown in Fig. 2.10, is the same for all values of e/L. The torsional effect due to the eccentricity, in fact, serves merely to perturb the relationship between M_o and u_{mt} in the same manner as would an initial imperfection (i.e., out-of-straightness). Thus, torsional loading only increases the lateral deflection of the beam prior to buckling (i.e., when it is still in a theoretically stable configuration).

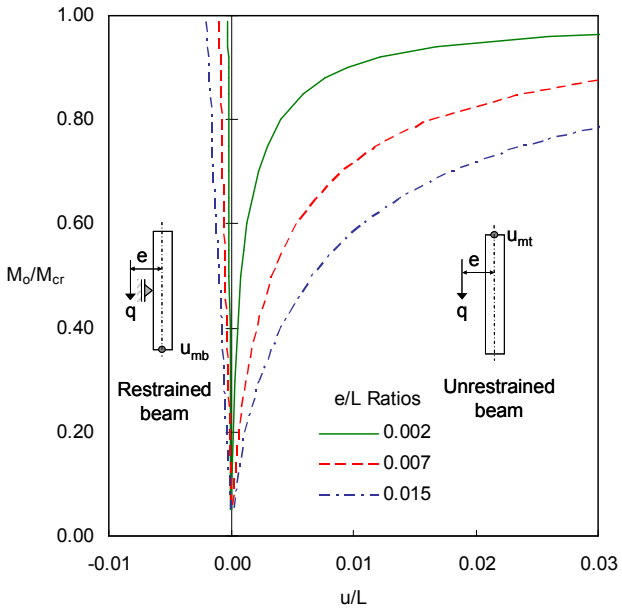

Fig. 2.10. Bending moment-maximum lateral deflection curves for rectangular beams with various values of eccentricity (h/L=0.11)

In Fig. 2.10, negative deflections u_{mb} are noted for the laterally restrained beams. The bottom of the mid-span section of the beam moves outward. The relationships between lateral deflections u_{mb} and bending moment M_o are shown for different eccentricity ratios. With an increase of the eccentricity, magnitudes of lateral deflection increase for restrained beams, but remain much smaller than those for unrestrained beams with the same M_o/M_{cr} ratio. Based on Eq. (38), it can also be concluded that lateral deflections are proportional to both the height-to-length ratio h/L and the eccentricity e.

In order to compare lateral deflections at the centroid and top of the mid-span section of a laterally unrestrained beam, bending moment-lateral deflection curves for various eccentricity parameters are plotted in Fig. 2.11, using Equations (23) and (36), respectively. The figure shows that the centroid of the section undergoes slightly smaller lateral deflections than the top of the section due to the twisting of the beam. Even though the lateral distance between these two points at the section increases with an increase of eccentricity, twisting of the beam contributes only slightly to the maximum lateral deflection.

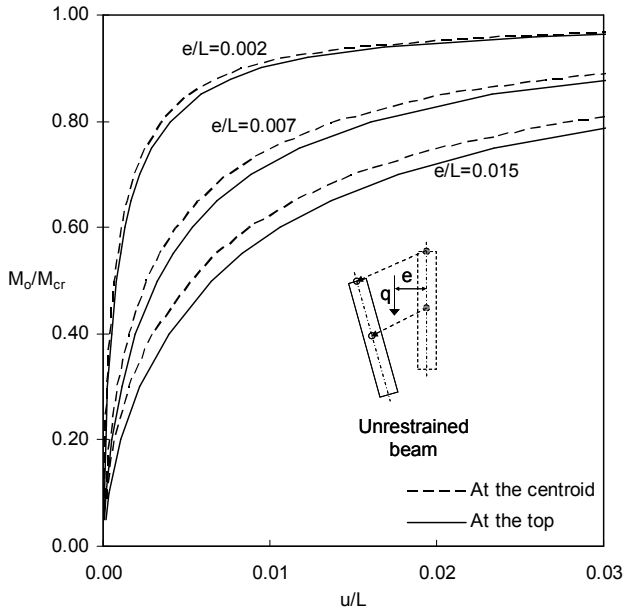

Fig. 2.11. Lateral deflections at the top and centroid of the laterally unrestrained rectangular beams (*h/L*=0.11)

The effect of slenderness ratio *h/L* on maximum lateral deflection (at the top) in a laterally unrestrained beam is also investigated. The slenderness ratio *h/L* of beams is assumed to vary from 0.08 to 0.24. Fig. 2.12 shows bending moment-lateral deflections curves for various eccentricity parameters (*e/L*=0.002, 0.007 and 0.015). Bending moment-lateral deflection curves for beams with small values of eccentricity parameters (i.e., *e/L*=0.002) are not significantly affected by different slenderness ratios. However, the lateral response of an unrestrained beam is more sensitive to its slenderness ratio if the eccentricity increases (i.e., *e/L*=0.015).

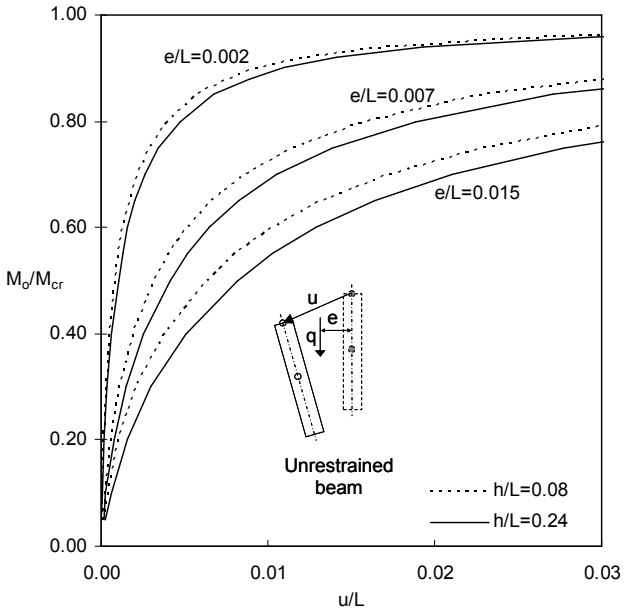

Fig. 2.12. The response of unrestrained rectangular beams for different slenderness ratios (*h/L*=0.08 and 0.24)

2.9. Finite element analysis

The lateral deflection response of eccentrically loaded concrete beams is a complicated problem that is not well represented in the technical literature. Even though experimental and analytical studies in the pertinent literature and design codes provide a rational guidance to the designer for predicting vertical deflections, little, if any, attention is paid to the lateral deflections. The approximate closed-form solutions presented in this paper for lateral deflection in laterally restrained and unrestrained rectangular beams subjected to eccentric loading are the only such available formulas. Because of their applicability to two of the most common types of precast, prestressed concrete spandrel beams, the accuracy of the approximate closed-formed solution are investigated for eccentrically loaded rectangular beams and typical spandrel beams with finite element analyses using the commercial software package ABAQUS [19].

Derivation of the preceding approximate closed-formed solutions for elastic rectangular beams required several simplifications as follows:

(a) higher-order terms and some less important terms in the governing differential

equations were neglected,

(b) modified loads (labeled as 'substitute' loads) were used,

(c) rectangular beams were assumed instead of spot-corbel, pocket or L-shape spandrels, as shown in Fig. 2.1,

(d) and material nonlinearity (i.e., concrete cracking and crushing), steel reinforcement and prestressing strands were ignored.

Assumptions (a) and (b) were necessary to enable closed-form solutions for the differential equations governing the problem. Assumptions (c) and (d) were used to transform the problem from the realm of precast, prestressed concrete spandrels to that of elastic, rectangular beams.

The error introduced by assumptions (a) and (b) were evaluated by comparing the results of analytical method and finite element analyses. Restrained and unrestrained rectangular beams were modeled in ABAQUS using quadratic beam elements, subjected to actual loads (uniformly distributed load acting eccentrically). Geometric and mechanical properties of the beam selected for this numerical study were: L=534 in. (13.56m); h=60 in. (1.52m); b=8 in. (203mm); e=4 in. (102mm); I_x=144,000 in^4 (5.994×10^{10}mm^4); I_y=2,560 in^4 (1.066×10^{9}mm^4); J=10,240 in^4 (4.262×10^{9}mm^4); E=4,800 ksi (33.1GPa); G=1,920 ksi (13.2GPa). The beams consisted of simple supports at their ends for vertical loads and deflections, as well as fixed torsional constraints. Lateral restraints were provided by fixing the horizontal displacements of the nodes along the centerline of the beam elements in the model for the case of the restrained beams. The material model for prestressed concrete was assumed to be linearly elastic. Large deformations were included and solved using the Modified Riks Method (Arc-Length Method) [19] as a solution procedure for FE analyses.

The critical buckling moment M_{cr} was calculated as 91,440 k-in (10,330kN-m) using Eq. (4) for the beam subjected to equivalent loading (end bending moments). However, the critical buckling moment M_{cr} increased by the factor of C_b when the actual loads (uniformly distributed load) act on the beam, and it was equal to 103,330 k-in (11,670kN-m) for C_b=1.13 which corresponds to uniformly distributed loads. From the finite element analysis, the buckling moment of the beam was found to be 103,787 k-in (11,730kN-m).

The critical moment M_{cr} (under uniformly distributed loads) is needed simply as a normalization factor for the moment data obtained from the finite element analysis, because it appears as a normalization factor for the deflection and twisting angle formulas obtained earlier. Seldom, if ever, will a spandrel beam be designed for moments M_o that approach the critical value M_{cr}.

Fig. 2.13 shows the relationship between the moment ratio M_o/M_{cr} and the deflection parameter u/L for each of the analysis cases of restrained or unrestrained beams having two different values for normalized eccentricity, e/L=0.007 and 0.015 (these values correspond to e=4 in. (102mm) and 8 in. (203mm), respectively). Analytical results obtained using Eqs. (36) and (38) are also shown as solid lines in this figure. Lateral deflections at the top of the mid-span section of the laterally unrestrained beams are in the positive direction (toward the loads), whereas lateral deflections at the bottom of the mid-span section of the laterally restrained beams are in the negative direction. Results are presented using dimensionless parameters, the moment ratio M_o/M_{cr} where M_o is the maximum bending moment in the beam (i.e., $qL^2/8$) and the deflection parameter u/L.

Fig. 2.13 indicates that numerical and analytical results are in very good agreement for both restrained and unrestrained beams. The analytical results for the substitute loading closely match the numerical results from the FE model under the actual loading, which proves that neglecting higher order terms when finding the analytical solutions does not lead to significant error. For laterally unrestrained beams, Fig. 2.13 also shows that there are only minor differences between actual and substitute loading cases (the difference is less than 10%). Consequently, the proposed analytical procedure, using 'substitute' loading, is seen to be a powerful tool for estimating the lateral deflections in laterally restrained and unrestrained slender rectangular beams under uniformly distributed eccentric loads. Noted that the h/L ratio of the beam studied here was 0.11, and comparison of numerical and analytical responses observed for other e/L and h/L ratios, not shown here for the sake of brevity, indicate similar trends.

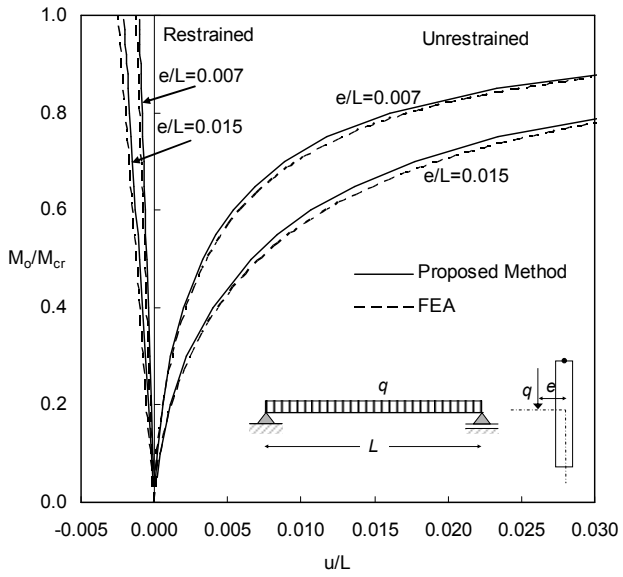

Fig. 2.13. Numerical vs. analytical results for maximum lateral deflections for rectangular beams (h/L=0.11)

The proposed analytical method assumes that an eccentric load is applied along the centerline of the beam. However, a typical spandrel beam (Fig. 2.1) carries loads at the corbels, pockets or ledges located below the beam mid-depth. It is known that the buckling capacity and deformation response of a beam depend on the position of the loads. Therefore, it is necessary to study the applicability of the proposed analytical method to different loading positions. Three-dimensional models of rectangular beams eccentrically loaded at different locations were generated using 20-node elements with reduced integration in ABAQUS. The beam geometry and material characteristics were the same as those previously given. Due to symmetry, only one-half of the beam was modeled. In the first model, the beam was eccentrically loaded (e=b/2= 4 in.) at its mid-height level, as shown in Fig. 2.14. In the next model, the same eccentricity was maintained, the point of load application was moved to the bottom of the beam. The buckling moment of the beam for the case of mid-height loading was obtained from FE analyses as 103,089 k-in (11,647 kN-m), whereas the theoretical value from Eq. (5) is 103,787 k-in (11,726 kN-m). For the case of loading at the bottom of the beam, FE analysis resulted in the buckling moment of 109,256 k-in (12,344 kN-m). Yet, the

theoretical capacity given by Eq. (5) should be modified by a coefficent C_y to reflect the influence of vertical location of load application. Park and Paulay [20] report a solution for C_y equal to $\left(L-1.74y_w\sqrt{EI_y/GJ}\right)/L$ in which y_w is the vertical distance of load application above the centroid of the section. This formula yields C_y=1.07728 and, consequently, a corrected critical M_{cr}=111,808 k-in. (12,632 kN-m). Thus, the buckling capacity of the unrestrained beam increases when the load is applied at the bottom instead of the mid-depth.

Fig. 2.14 shows the lateral-deflection results from FE analyses (for both mid-height and bottom loading) and analytical method (for mid-height loading only). Even though the absolute values for bending moments and lateral deflections were different for two loading conditions, the normalized results are in very close agreement. They are also very close to the proposed approximate analytical solution. For laterally restrained condition, for which the beams had lateral fixity in the mid-depth, the variation of the results from FE analyses and analytical method was negligible.

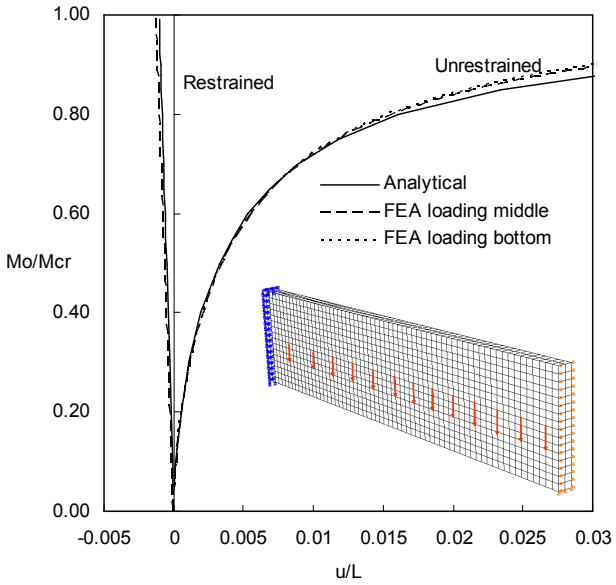

Fig. 2.14. Influence of the loading position

Next, the elastic, three-dimensional models of spot corbel and pocket type spandrels were generated in ABAQUS by modifying the previous rectangular beam model. Cube-

shaped corbels were added with a side dimension of 8-in. (203mm), and were equally spaced (6-ft (1.83m)) along the spandrel beam, as seen in Fig. 2.15. Similarly, in the pocket spandrel model, pockets that are 9-in (229mm) long, 20-in (508mm) deep and 4-in (102mm) wide were located with the same equal spacing (6-ft (1.83m)), as shown in Fig. 2.16. Given the symmetry of the beams, only one-half of the beams were modeled. The loading eccentricity was defined as 8 in. (203mm) for the spot corbel spandrel, assuming the load acted at the middle of the width of each corbel. However, the eccentricity was defined only as 4 in. (102mm) for the pocket type spandrel, assuming the extreme condition of the double-tee loads acting on the outside edge of pockets. Both laterally restrained and unrestrained cases were considered. Finite element estimates of M_{cr} for the spot-corbel and pocket spandrels, respectively, were computed as 106,646 k-in (kN-m) and 98297 k-in (kN-m). These differ somewhat from the theoretical value of M_{cr} for a rectangular section (103,787 k-in. (11,726 kN-m)) by virtue of the material that is added or removed, respectively, from the corbel and pocket.

Fig. 2.15 indicates that the proposed analytical solution is in good agreement with the predicted response for spot-corbel spandrel obtained from FE analysis. The spot corbel spandrel exhibits stiffer response and larger buckling capacity from the finite element analysis than the approximate solution for a rectangular beam. However, the discrepancies between the solutions are not large. Fig. 2.16 shows the results from the finite elements analyses of the pocket type spandrel. The discrepancies between FE and analytical results are larger, which is attributable to the significant effect of rectangular cutouts on the lateral deflections in the spandrel (30% difference). In this case the finite element model of the pocket type spandrel is more flexible than the approximate analytical solution for a rectangular beam. The approximate solutions both the corbel and pocket spandrels can be improved by using a more accurate estimate of M_{cr}.

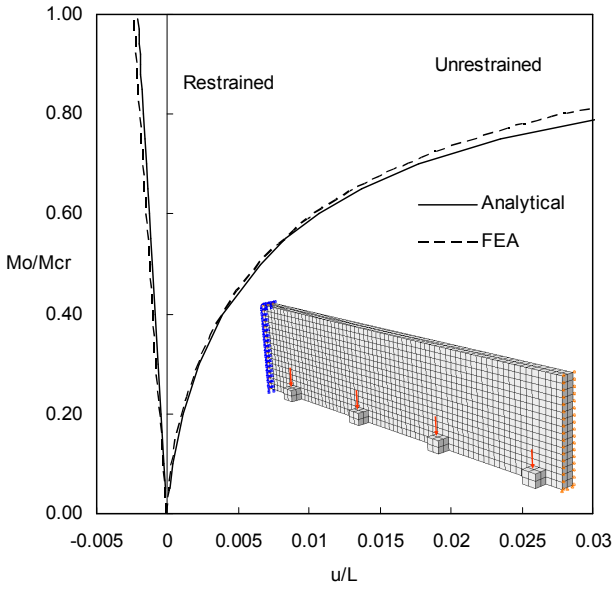

Fig. 2.15. Behavior of spot corbel spandrels

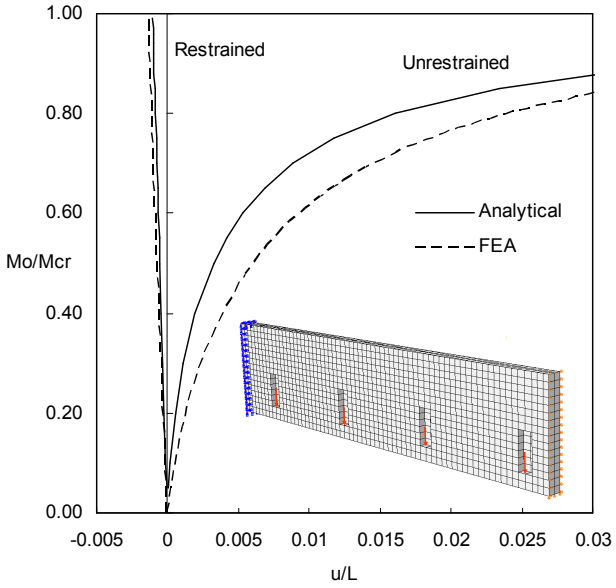

Fig. 2.16. Behavior of pocket-type spandrels

The lateral response of eccentrically loaded L-shaped spandrel beams exhibits even more complicated behavior than that for rectangular beams or for the other types of spandrels discussed above. L-shape spandrels are subjected to more significant amounts of asymmetric bending, which drastically affect the lateral deflection response. For this

reason, the proposed analytical solution is not valid for L-shapes. Further study of such beams is necessary for the formulation of accurate deflection solutions.

2.10. Conclusions

Slender, precast and prestressed concrete spandrel beams under eccentric loading are susceptible to large lateral deformations and possible serviceability failure before reaching their strength limits. Depending of the strength and reliability of deck-tie connections, spandrel beams may be treated as a laterally unrestrained beam (i.e., free to deform laterally), or as a laterally restrained beam (i.e., assumed to have continuous lateral support along the centroidal line of the beam). In this study, approximate analytical solutions for maximum lateral deflections in laterally restrained and unrestrained rectangular beams under eccentric loading were derived using second-order elastic analysis with several simplifying assumptions.

To obtain a simple closed-form approximate solution for the governing differential equations of the problem, a 'substitute' loading approach is proposed, in which the eccentric load (actual load) is replaced with end bending moments and uniform torque (substitute loads). After finding the maximum angle of twist in restrained and unrestrained rectangular beams, the following observations were made: (a) the maximum lateral deflection was shown to occur at the top of the mid-span section of the laterally unrestrained beam, (b) all sections in laterally unrestrained beams under eccentric loads were shown to move laterally toward the loading side, (c) the laterally restrained beam was shown to undergo only twisting due to the eccentricity, or rotation about its longitudinal direction, (d) deflections of restrained beams are much smaller than those of unrestrained beams, and (e) the lateral deflection at the bottom of restrained beam moves outward, which can cause the double-tee beams to lose their supports. Additionally, the differences in lateral deflections between laterally unrestrained and restrained beams are so large that it seems necessary to pay increased attention to the analysis, design and durability of the deck-ties if they are going to be assumed effective over the life of the spandrel.

Numerical solutions were also provided from three-dimensional finite element analyses of laterally restrained and unrestrained elastic spandrel beams. The results from spot-corbel and pocket type spandrels were found to be closely comparable with those of proposed analytical solutions.

Finally, noting the lack of information in the technical literature regarding with lateral deflections in spandrels, the elastic deflection solutions proposed here represent a pioneering contribution on a topic which is presently devoid of alternatives short of finite element analysis. As such, and the solutions can be used for deflection serviceability checks in design, but also to provide guidance in future research studies on this subject.

2.11. Notation

b	=	width of beam
C_b	=	bending coefficient
e	=	eccentricity
E	=	elastic modulus
E_c	=	elastic modulus of concrete
E_r	=	reduced elastic modulus of concrete
G	=	elastic shear modulus
h	=	height of beam
I_x	=	moment of inertia about the strong axis
I_y	=	moment of inertia about the weak axis
J	=	torsional constant
L	=	length of beam
m	=	uniformly distributed torsion
M_{cr}	=	critical bending moment
M_i	=	moment in global axes for $i=x,y,z$; local axes for $i=x^*,y^*,z^*$
M_o	=	bending moment couples about strong-axis at the ends of beam
m_o	=	equivalent distributed torsion
q	=	uniformly distributed load
q_o	=	equivalent distributed load
u	=	lateral displacement
u_m	=	maximum lateral displacement of beam centerline
u_{mb}	=	maximum lateral displacement at the bottom of beam section
u_{mt}	=	maximum lateral displacement at the top of beam section
v	=	vertical displacement
y_w	=	vertical distance of load application above the centroid of the section
ϕ	=	angle of twist
ϕ_m	=	maximum angle of twist

CHAPTER 3

Finite Element Modeling and Test Verifications

3.1. Introduction

Recent improvements in the field of computer technology have offered an opportunity to implement numerical solution methods to increasingly more detailed and complicated engineering problems. Even tough experimental methods still play a key role in research, and numerical methods are getting more attractive due to their lower cost and time comparing to experiments. Highly nonlinear problems might be solved by using numerical methods such as finite element methods. On the other hand, finite element methods require the knowledge of how various modeling parameters might affect the results and what values for these parameters should be used to properly describe a specific problem such as the response of a spandrel beam under various loading conditions. Inadequate attention to these parameters might lead to worthless results.

For this purpose, the results obtained from various experimental studies, reported in literature on concrete structures, were verified with those of finite element models generated with a commercially available computer program, ABAQUS [21]. At first, the response of plain concrete prism under uniaxial tension was studied to determine how accurately a tensile failure can be predicted with the concrete damage-plasticity model, an advanced material model for concrete in ABAQUS. The next study included the modeling of concrete under biaxial loading and a discussion on the influence of various modeling parameters. The final verification example was associated with the pure bending of conventionally reinforced concrete beams, presenting the effects of finite element type and size, concrete-rebar interactions, and steel ratio.

3.2. Behavior of Concrete

Concrete is an inhomogeneous material which consists of aggregate and cement paste (cement, sand and water) in various ratios. Experimental measurements show that fundamental properties of concrete such as elastic modulus, compressive strength and tensile strength vary in a broad range, which reduces the accuracy level of analysis and

design predictions. The behavior of concrete under compression has a nonlinear ascending branch up to ultimate strength, f'_c, followed by a pseudo strain hardening region as seen in Figure 3.1. However, in tension, concrete cracks under very low stress level (around $0.1f'_c$ for normal strength and $0.05f'_c$ for high strength concrete). Cracking by itself has not been a well-understood phenomenon and is still a popular research topic. For reinforced concrete members, the concrete-rebar interaction, especially the so-called bond-slip, has to be taken into account. Multiaxial stress states and corresponding failure modes in concrete are other difficulties and usually treated with the theory of plasticity. However, unlike metals, concrete experiences large volumetric changes under compression which is unique to granular materials. Therefore, plasticity theory is usually employed with some modifications for concrete.

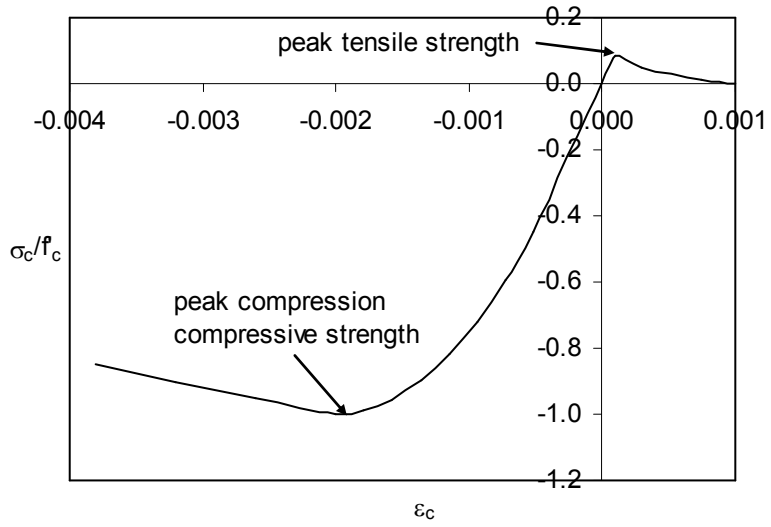

Figure 3.1 Uniaxial behavior of concrete

The accuracy of computer analyses depends primarily on how precisely the material model is defined. When material exhibits very complex behavior, as in the case of concrete, defining a material model with high level of accuracy can be a very difficult task. A simple linear-elastic material model is not adequate for most applications of concrete, particularly when the limit load on the structure is to be determined. To be able to perform more detailed analysis of concrete structures, the material model used in the finite element analysis should include various unique features of concrete such as

cracking, crushing, stiffness degradation, volumetric change etc. [24].

Even though micro- and macro-cracking properties of concrete under different loading conditions describe the behavior of concrete, predicting the initiation and development of such cracks is quite difficult. Concrete under tension is relatively brittle, because the aggregate–mortar interface has a very small tensile strength. Confined concrete however shows more ductile behavior than unconfined concrete under uniaxial stress state. The ultimate strain capacity of concrete gets larger with increases in lateral stress. However, after a certain value of lateral stress (confining stress), strain at failure gets smaller. Volumetric expansion of concrete is also observed due to its composite nature when micro-cracks are observed to noticeably increase in the mortar [24].

Properly formulated plasticity theory can be used to define the behavior of concrete even though the theory was originally developed for metals. This is so because both materials exhibit some similarities in overall response, such as irreversible deformation and ductile behavior assuming confined concrete. Extensive experimental data is required to properly define the behavior of concrete with mathematical models. Today, some types of experiments, for example uniaxial compression, can be conducted with sufficient accuracy and provide information for better understanding of concrete behavior. Nevertheless, some tests such as triaxial loading are still difficult to perform and only a limited amount of data is available for the strength, stiffness and deformation characteristics of concrete under this loading state.

Stress-strain curves of concrete under cyclic loading have an envelope which is similar to uniaxial stress-strain curve under monotonic loading. Biaxial compression strength of concrete is at least equal to the uniaxial compression strength. This is valid for biaxial tension strength as well. Towards the peak-stress value of concrete under compression, volumetric change increases. Compaction of concrete under triaxial loading is the main reason for deformation. Confining compression stress leads to large deformation or ductility. The tensile strain limit can be considered as a failure criterion of concrete under uniaxial or biaxial stress state [24].

Typical load-deflection curve of a reinforced concrete member consists of linear and nonlinear regions. In the linear region, cracks are not observed and the member is elastic.

In general, the early stages of the nonlinear region include crack formation and propagation. In the next stage, nonlinear behavior is defined by plastic responses of concrete (crushing) and rebar (yielding). There are some other features of the reinforced concrete member, which contribute to the nonlinear response. They can be classified as time-independent (e.g., bond-slip and aggregate interlock) and time-dependent factors (e.g., creep, shrinkage and temperature expansion/contraction). A generalized material model is necessary to describe the main characteristics of the reinforced concrete member mentioned above. The generalized model might be defined in three steps: First, the reinforcement can be represented by one-dimensional element carrying axial load only and hence the behavior of steel can be defined with a uniaxial stress-strain relationship only. Second, a model for the multidimensional behavior of concrete should be assumed. But this is the most difficult problem and one which is not completely solved. Finally, concrete-rebar interaction is defined by modeling the bond-slip phenomenon. In some cases, assuming perfect bonding and no slip provides reasonable results [24].

3.3. Damage-Plasticity Model of Concrete

The behavior of concrete including cracking can be described using one of three material models in ABAQUS; the concrete damage-plasticity (CDP) model, the concrete smeared cracking (CSC) model and the brittle cracking model. Concrete models are differentiated based on the loading conditions (monotonic or cyclic) and controlling failure types (tensile cracking, compressive crushing). The smeared cracking model in ABAQUS/Standard was essentially developed for concrete under monotonic loading, experiencing either tensile cracking or concrete crushing. The brittle cracking model in ABAQUS/Explicit emphasizes the tensile cracking of concrete rather than concrete crushing as an essential material behavior. The concrete damage-plasticity model is a constitutive model for concrete which is generally used in the analysis of reinforced concrete structures under cyclic loading.

The damage-plasticity model is based on the limit states of concrete crushing in compression and cracking in tension. In other words, concrete behaves in brittle manner.

High confining pressure causes concrete to respond as a ductile material. In this case, the propagation of micro-cracks instead of large cracks determines the response of concrete. The concrete damage-plasticity model does not deal with such a ductile behavior of concrete. The model is based on the assumption of scalar isotropic damage. The plastic-damage model in ABAQUS relies on the models proposed by Lubliner *et al.* [25] and by Lee and Fenves [26].

In the incremental theory of plasticity, the total strain rate, $\dot{\varepsilon}$ is decomposed into the elastic and plastic parts, $\dot{\varepsilon}^{el}$ and $\dot{\varepsilon}^{pl}$, respectively (3.1).

$$\dot{\boldsymbol{\varepsilon}} = \dot{\boldsymbol{\varepsilon}}^{el} + \dot{\boldsymbol{\varepsilon}}^{pl} \tag{3.1}$$

Next, the stress-strain relationship can be established in the following form:

$$\boldsymbol{\sigma} = \boldsymbol{D}^{el} : (\boldsymbol{\varepsilon} - \boldsymbol{\varepsilon}^{pl}) \tag{3.2}$$

where $\boldsymbol{D}^{el}$ represents the degraded elastic stiffness tensor which is of the fourth rank and $\boldsymbol{\sigma}$ is the stress tensor. Based on the concept of the plastic damage theory, the degraded elastic stiffness tensor $\boldsymbol{D}^{el}$ means that the effective load-carrying area reduces as the concrete reaches one of the failure mechanisms (compressive crushing or tensile cracking). In general, the isotropic degradation damage is assumed with a scalar variable d ranging from 0 to 1.

$$\boldsymbol{D}^{el} = (1-d)\boldsymbol{D}_o^{el} \tag{3.3}$$

where $\boldsymbol{D}_o^{el}$ is the undamaged elastic stiffness.

Equivalent plastic strains in tension and compression, $\tilde{\varepsilon}_t^{pl}$ and $\tilde{\varepsilon}_c^{pl}$, which are the so called hardening variables, are used to describe damaged states of micro-cracking and crushing in concrete. The evolution of the yield surface and the degradation of the elastic stiffness are controlled by these hardening variables, which can be described as follows:

$$\tilde{\varepsilon}^{pl} = \begin{bmatrix} \tilde{\varepsilon}_t^{pl} \\ \tilde{\varepsilon}_c^{pl} \end{bmatrix} \tag{3.4}$$

and

$$\dot{\tilde{\varepsilon}}^{pl} = h(\bar{\sigma}, \tilde{\varepsilon}^{pl})\dot{\varepsilon}^{pl} \tag{3.5}$$

A yield function, as seen in equation (3.6), can be expressed in terms of the effective

stress $\bar{\sigma}$ and the equivalent plastic strains, $\tilde{\varepsilon}^{pl}$. The yield function is defined in the effective stress space and is bounded by tensile cracking and compressive crushing. These two failure modes are taken into account using the equivalent plastic strains in tension and compression, $\tilde{\varepsilon}_t^{pl}$ and $\tilde{\varepsilon}_c^{pl}$.

$$F(\bar{\boldsymbol{\sigma}}, \tilde{\boldsymbol{\varepsilon}}^{pl}) < 0 \tag{3.6}$$

The flow rule is defined with a flow potential *G*, which ensures that the flow direction is always uniquely defined as in equation (3.7). The parameter $\dot{\lambda}$ is the non-negative plastic multiplier. The concrete damage-plasticity model assumes that the flow potential *G* is defined with the non-associated Drucker-Prager hyperbolic function (ABAQUS).

$$\dot{\boldsymbol{\varepsilon}}^{pl} = \dot{\lambda} \frac{\partial G(\bar{\boldsymbol{\sigma}})}{\partial(\bar{\boldsymbol{\sigma}})} \tag{3.7}$$

3.4. Smeared Cracking Model of Concrete

Similar to the concrete damage-plasticity model, the smeared cracking model of concrete is valid for the case of low confining pressure. However, this model is only applicable to concrete under monotonic loading. Concrete cracking is assumed to be the governing failure mode. Cracking develops when the stresses reach a failure surface, so-called "crack detection surface" [21]. Rather than tracking micro-cracks in concrete, a smeared crack model is based on the idea that the presence of cracks reduces the stiffness and strength values associated with an integration point in the finite element model.

When concrete is dominantly subjected to the principal compressive stresses, failure is defined with a simple yield surface based on the first two stress invariants. The model assuming associated flow and isotropic hardening simplifies the actual response of concrete since the third stress invariant required to predict the inelastic volume strain is simply ignored in this model. Even though there are limitations as noted above, the smeared cracking model still provides adequate prediction ability for various problems. The most important advantage of using this model is the reduction of the computational cost since the assumption of associated flow introduces symmetry in the material stiffness matrix [21].

3.5. Uniaxial Tension of Plain Concrete

3.5.1. Description of the Experiment

In general, the resistance of cracked concrete is ignored in many design applications for the sake of simplicity. However, neglecting the post-cracking behavior of concrete may not be accurate in the nonlinear finite element analysis of concrete structures. Post-cracking response of concrete plays an important role in predicting deflection, crack width, bond-slip, and shear transfer [27]. It is quite difficult to conduct uniaxial tensile tests of concrete, and the data obtained from different tests are often conflicting. Testing difficulties are caused by several reasons; the failure of concrete due to multi-dimensional stress conditions around the grips and the unstable post-peak response of concrete. Gopalaratnam and Shah [27] developed a testing method to obtain more reliable test results of concrete in tension and investigated the load-deformation behavior of plain concrete in tension, including the post-peak softening branch. They also proposed an analytical model to predict the response of concrete in tension.

Rectangular direct tension specimens with different mix proportions and the dimensions of 3 x ¾ x 12-in. and 3 x 1½ x 12-in. were used. They were subjected to monotonically increasing displacement at a rate of one micro-strain per second. Total testing duration was generally around one half-hour. Some specimen had notches with the depth of 0.5-in. and the width of 0.1-in. Test results were also presented for the case of cyclic loading bounded by the monotonic envelope and zero stress. Compression tests of 3 x 6-in. cylinders were also conducted and some material properties such as compressive strength, strain at the peak-stress, initial modulus were reported. Stress-displacement curves with a gage length of 3.25-in. were provided based on the test results [27].

The test results showed that the stress-displacement curve was independent of the notch presence. Elastic modulus in the tension and compression were similar. Based on the strain values monitored at various locations on a specimen, it could be concluded that the ascending branch of the stress-strain curve was independent of the gage length and there was a unique stress-strain relation in this region. However, the post-peak response

did not show any unique stress-strain relation due to the localization of deformations. Instead an average stress-average crack relationship was used to uniquely define the post-peak behavior [27].

3.5.2. Description of the Finite Element Model

One of concrete specimens tested by Gopalaratnam and Shah [27] was selected and modeled using ABAQUS/Standard and next analysis results were compared with test results. A cubic eight-node brick element with reduced integration was used to model the test specimen. The edge length of the brick element was assumed to be equal to 3.25-in which was the gage length used for the test measurements. The damage-plasticity model was used to define the behavior of cracked concrete. Tension stress applied to one face of the cubic element was defined as pressure and the opposite face of the cube was restrained in the loading direction only. Since the specimen was subjected to both loading and unloading during the test, displacement-controlled static analysis was performed.

Major properties of the selected specimen are listed in Table 3.1. They were extracted from experimental data. However, the data listed in this table are not enough to fully define damage-plasticity model for concrete. Therefore, it was necessary to make some assumptions for certain model parameters. The elastic modulus of concrete varied in tension and compression, as seen in Table 3.1. However, an elastic modulus value of 4.853×10^6 psi based on the tensile test was used in the model for both compression and tension behavior. In fact, the compressive behavior of concrete had no effect on the uniaxial tensile response, and a linear stress-strain relation was used for concrete in compression. Poisson's ratio was taken equal to 0.15. The dilation angle was considered to be 30 degrees. Tension stiffening of concrete was defined (1) using the test data for stress-cracking displacement and (2) a fracture energy of 0.322 lb/in.

Tension damage parameters used in the concrete damage-plasticity model were also determined using the test data. Using the stress-displacement response of the concrete specimen, the slopes of unloading response at various stress levels were approximately estimated. Comparing the initial elastic modulus with unloading elastic modulus for a

stress value, the tension damage parameter d_t were obtained. Tension damage parameters for five cycles were tabulated in Table 3.2. However, in concrete damage-plasticity model, tension damage d_t must be defined in terms of cracking displacement of concrete. A stress-cracking displacement curve was used to determine the cracking displacement for a certain stress level and damage parameter.

Table 3.1 Average concrete properties for mix proportions of 1:2:2:0.45 (cement:sand:aggregate:water) [27]

Tension Test				Compression Test		
Strength	Modulus	Strain	Fracture	Strength	Modulus	Strain
f_t	$E_t x10^6$	$\varepsilon_t x10^{-6}$	G	f'_c	$E_c x10^6$	$\varepsilon_c x10^{-6}$
psi	psi	-	lb/in	psi	psi	-
525	4.853	120	0.322	6364	4.41	1843

Table 3.2 Tension damage parameters

Cycle	Stress / Tensile Strength (σ/f_t)	Tension Damage Parameter d_t
1	0.54	0.18
2	0.32	0.52
3	0.23	0.68
4	0.16	0.80
5	0.12	0.85

3.5.3. Results and Discussions

The results of finite element analysis of pure concrete specimen were first compared with the test results for the study of mesh sensitivity. Three different configurations; (1) a 3.25-in cubic brick element, (2) a 3.25-in cubic mesh subdivided into eight brick elements and (3) a 1.625-in cubic brick element were taken into account. The tension stiffening region of the concrete in these finite element models was based on the test results of the specimen with the gage length of 3.25in. In Figure 3.2, the results of Case (1) and test were plotted. The results of the finite element analysis agree reasonably well with those of test. The reduction in initial elastic modulus due to tension damage can be clearly observed in the response of model during loading and unloading. However,

results were not obtained accurately for Case (2) as seen in Figure 3.3. In the elastic region, the mesh configuration has no effect. In the tension stiffening region, the cracking-displacement value at a certain stress level was approximately twice the value obtained in the test. It means that each element in Case (2) follows the stress-cracking displacement curve that was defined for tension-stiffening region in concrete damage-plasticity model. Figure 3.4 shows the results of Case (3) in which the 1.625-in brick element closely followed the test results for large displacement values. Even though the model maintained the fracture energy, the area under the stress-displacement curve, as in the Case (1), the results for the small displacement values was quite different from the test results. This was due to the fact that the length of the brick element in Case (3) was no longer equal to the gage length of 3.25-in, which was used for experimental measurement. These results also showed that smaller brick elements, Cases (2) and (3), had to undergo larger strain values than larger element, Case (1), to maintain the same tension-stiffening response.

Tension stiffening of concrete can be defined using either stress-cracking displacement relation or fracture energy. Figure 3.5 compares these two approaches for the cubic brick element with a length of 3.25-in, Case (1). The fracture energy used in the finite element analysis was 0.322 lb/in, which was reported by Gopalarantnam and Shah [27]. The fracture energy approach yielded linear tensile strength reduction. However, the area under curves obtained with two approaches resulted in the same value of 0.322 lb/in.

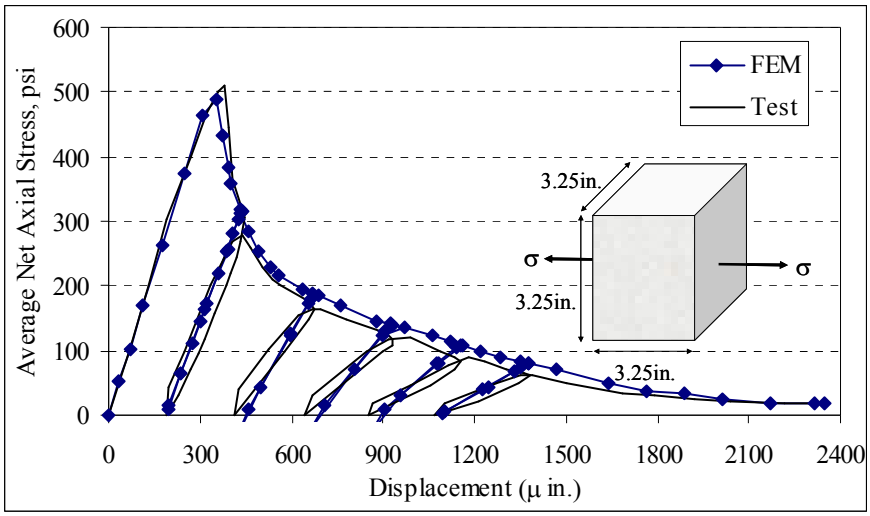

Figure 3.2 Response of brick element (1)

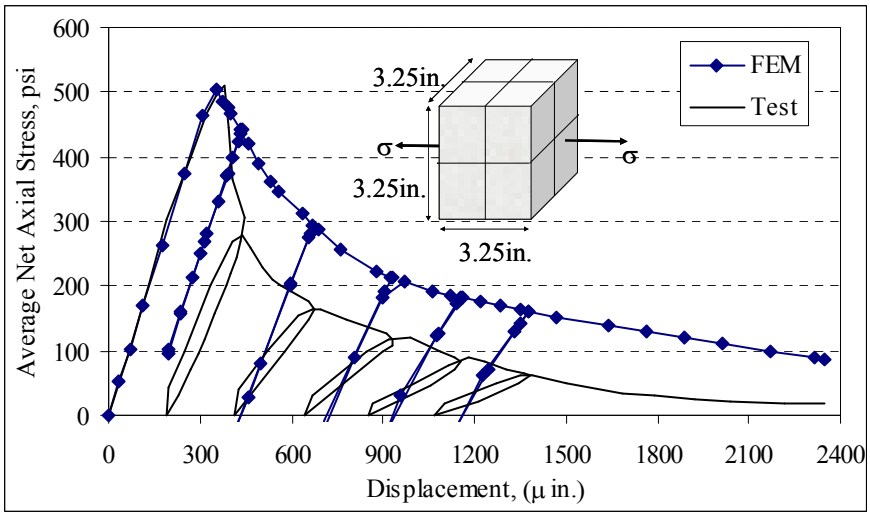

Figure 3.3 Response of finite element mesh (2)

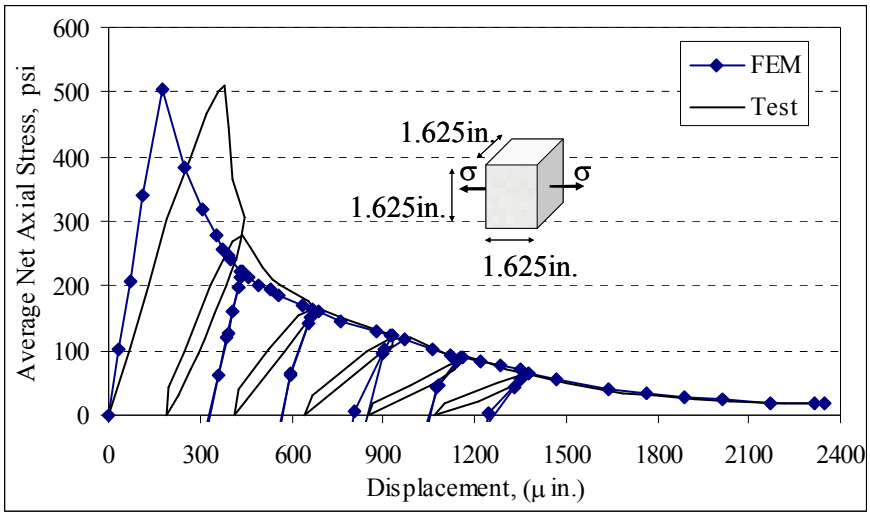

Figure 3.4 Response of brick element (3)

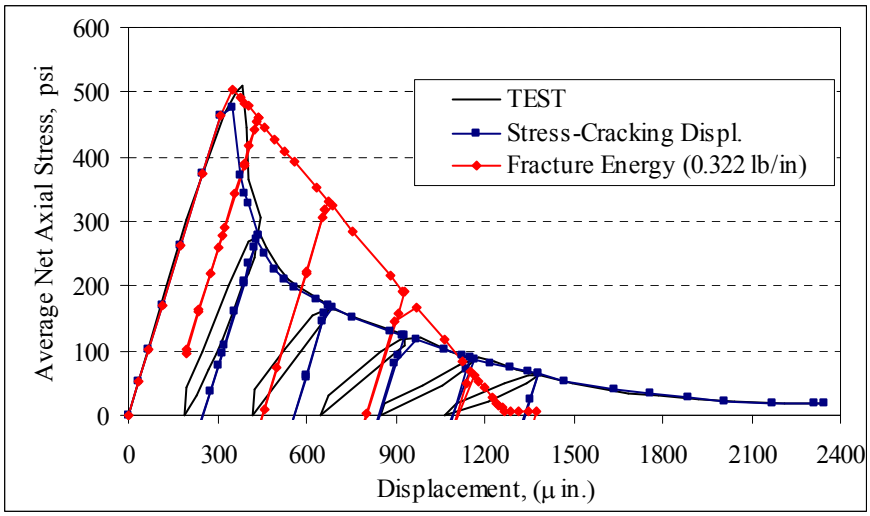

Figure 3.5 Comparison of tension stiffening assumptions

Some other aspects of concrete behavior based on damage-plasticity model were also investigated with finite element analysis. Results were independent of dilation angle which is typical of the response for concrete under uniaxial loading. Tension damage slightly increased the net axial stress at a certain displacement value and decreased the slope of the unloading path. It might be concluded that stress-displacement envelopes in both damaged and undamaged cases were relatively close and defining damage for concrete might be useful in the case of cyclic loading.

It could be concluded that when tension stiffening of concrete is defined with the

fracture energy approach, the value used for the fracture energy should be modified depending on the characteristic length of the finite element to remove mesh sensitivity of results. The characteristic length of a brick element was assumed the cube root of the integration point volume in ABAQUS. This is the reason why the element having a large aspect ratio can show differences in behavior depending on the cracking direction.

3.6. Biaxial Loading of Plain Concrete

3.6.1. Description of the Experiment

Kupfer, Hilsdorf and Rusch [29] studied the behavior of concrete under various states of biaxial stress. One of the major technical difficulties in testing of concrete in biaxial stress state is caused by applying accidental stresses into concrete specimen. This is the reason why there is a broad variation in the results reported by different researchers. Kupfer first had to develop suitable equipment for testing concrete under biaxial stress.

Next, concrete specimens with dimensions of 7.9x7.9x2 in. were tested for the cases of biaxial compression, compression-tension and biaxial tension. Four different stress ratios were applied in each loading case. They monitored load and concrete strains in the three principal directions. Uniaxial compressive strengths of tested concrete specimens were 2700, 4450 and 8350 psi.

Test results showed that the compressive strength of concrete increases 16 percent in the case of equal biaxial compressive stresses, and tensile strength remains almost constant for the case of biaxial tensile stresses. For the case of compression-tension stresses, compressive strength decreases due to the presence of tensile stress. The elastic modulus and Poisson's ratio are not influenced by the biaxial stress ratios.

3.6.2. Description of the Finite Element Model

To investigate the capabilities of ABAQUS/Standard in modeling of concrete behavior under biaxial loading, a finite element model was first generated and compared with test results reported by Kupfer *et al.* [29]. An eight node brick element with reduced integration was used with dimensions as shown in Figure 3.6. The element was

subjected to pressure in the 1- and 2-directions. Static, Riks analysis was performed for three loading cases such as uniaxial compression, biaxial compression and compression-tension.

The damage-plasticity model was first used to define the behavior of concrete. Compressive and tensile strengths of the selected concrete specimen were 4650 and 315 psi, respectively. The uniaxial stress-strain relation of concrete was defined based on test data reported by Kupfer *et al.* [29]. However, the behavior of concrete was assumed to be linear up to 45 percent of the uniaxial compressive strength ($0.45f'_c$= 0.45×4650=2093psi). The elastic modulus of concrete was obtained as 4500 ksi from the slope of the linear branch. The fracture energy was assumed to be equal to 0.3 lb/in. The dilation angle was first considered to be 30 degrees, but the effect of various dilation angles was also investigated during finite element analyses. The ratio of equi-biaxial compressive strength to unixial compressive strength of concrete, σ_{bo}/σ_{co} was taken 1.15, which was a value measured during the experiment. As no test data were available for the cyclic loading in this experiment, it was not possible to define compression damage parameters.

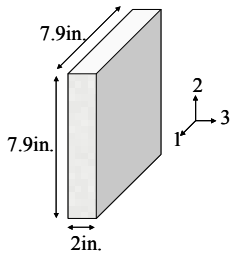

Figure 3.6 Specimen dimensions

The smeared cracking model for concrete was also implemented in the finite element analysis. The behavior of concrete under uniaxial loading was taken from the experimental measurement as in the case of damage-plasticity model. Other parameters required to define smeared cracking model are tabulated in Table 3.3. Failure ratios are paramaters used to define yielding. The ratio of equi-biaxial compressive strength to uniaxial compressive strength of concrete was taken equal to 1.15 and the ratio of uniaxial tensile strength to uniaxial compressive strength of concrete was taken as 0.068,

both which were measured during the experiment. Other ratios represent typical values for concrete. Shear retention is ignored for this example as it is generally used when loading and unloading is present. Finally, the maximum cracking displacement of concrete was defined to describe the post-cracking response. To be consistent with the concrete damage-plasticity model, the maximum cracking displacement of concrete was determined by assuming linear tension stiffening. The maximum cracking displacement was obtained as 0.0019 in. (=2×0.3/315) for a fracture energy of 0.3 lb/in and a tensile strength of 315 psi.

Table 3.3 Parameters of concrete smeared-cracking model

Failure Ratios			
$\frac{\sigma_{cu}^{biaxial}}{\sigma_{cu}^{uniaxial}}$	$\frac{\sigma_{tu}}{\sigma_{cu}}$	$\frac{\varepsilon_{pu}^{biaxial}}{\varepsilon_{pu}^{uniaxial}}$	$\frac{\sigma_{tu}^{biaxial}}{\sigma_{tu}^{uniaxial}}$
1.150	0.068	*1.280*	*0.330*

3.6.3. Results and Discussions

Finite element analysis for plain concrete under uniaxial tension showed that the results were sensitive to mesh configuration. A similar study was performed for concrete under uniaxial and biaxial compression. Two types of mesh configurations were taken into account. Mesh (1) included a single eight-node brick element with reduced integration, whereas Mesh (2) included four brick elements. Figure 3.7 shows the results of uniaxial compression. The stress-strain relation in the 1-direction followed exactly the curve obtained by test. However, a small divergence from the test data was observed for inelastic strains in the 2- and 3-directions. On the other hand, the results were not mesh sensitive. The response of concrete in equi-biaxial compression ($\sigma_1=\sigma_2$) is presented in Figure 3.8. No mesh sensitivity was observed in this loading case either. Finite element analysis yields slightly different response from the experimental measurements for inelastic strains in all directions.

Responses of concrete damage-plasticity and smeared cracking models for the case of tension-compression ($0.0052\sigma_1=\sigma_2$) are plotted in Figure 3.9 and Figure 3.10,

respectively. The model based on concrete damage-plasticity failed at a stress level which was almost one-half of the measured strength. However, the smeared cracking model yielded very good agreement with test results. Even though not presented herein, it should be noted that concrete smeared cracking model accurately predicted the behavior of concrete under uniaxial and biaxial compression, as well.

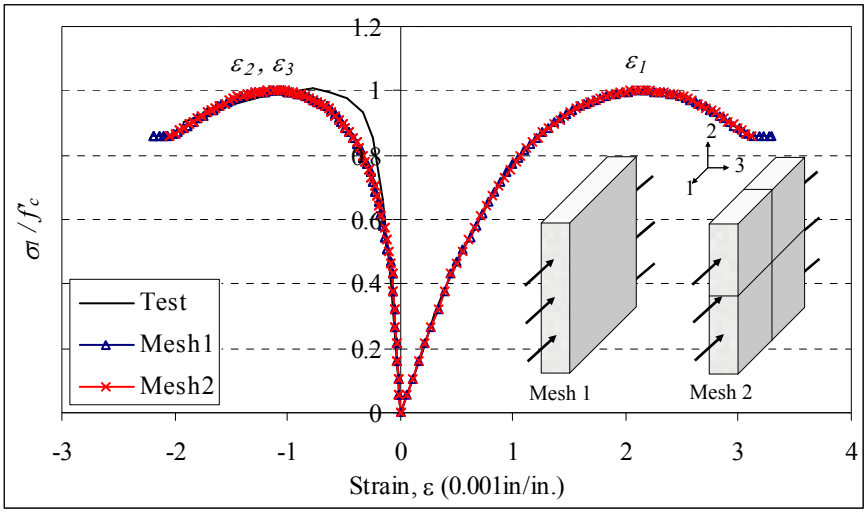

Figure 3.7 Mesh sensitivity in uniaxial compression-CDP

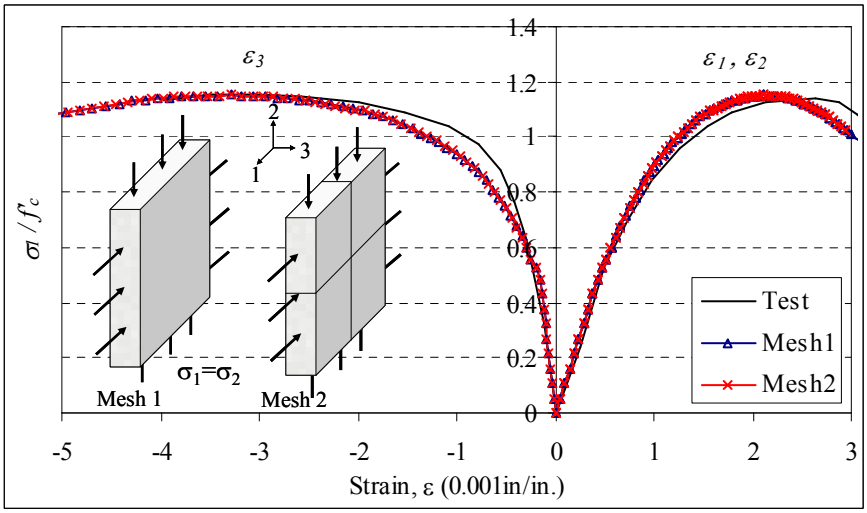

Figure 3.8 Mesh sensitivity in biaxial compression-CDP

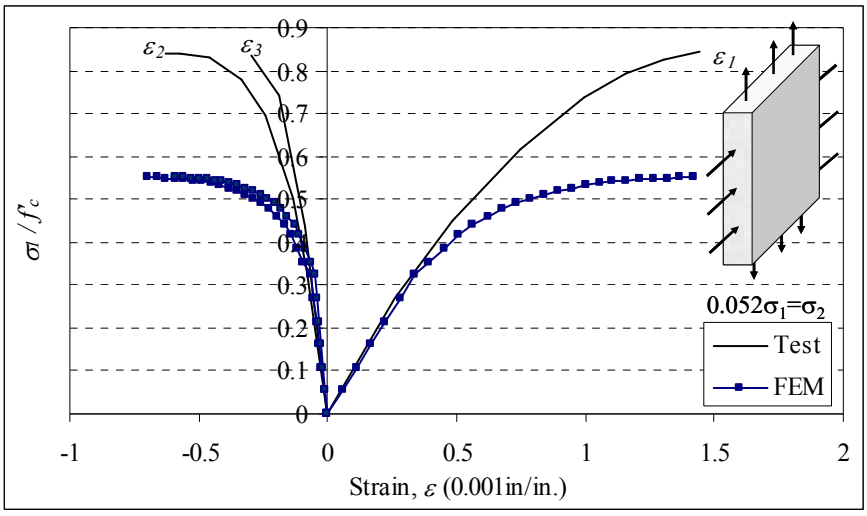

Figure 3.9 Response of CDP model in tension-compression

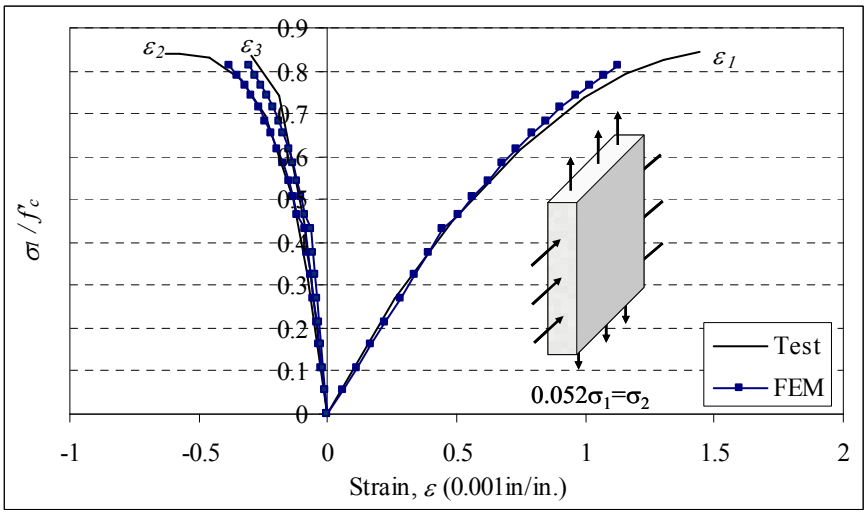

Figure 3.10 Response of CSC model in tension-compression

Dilation angle is an important parameter affecting the behavior of concrete especially in the unloaded directions. Finite element analysis results obtained for various dilation angles of concrete in uniaxial compression are compared with test results in Figure 3.11. The variation of the dilation angle was found to have no effect on the response in the loading direction (i.e., the 1-direction). However, the response of model in the 2- and 3-directions depended upon the value of dilation angle. An increase in the dilation angle made the inelastic response of concrete in 1- and 2- directions softer. The influence of dilation angle of concrete in equi-biaxial compression is similar to that of uniaxial

compresison. In this case, the response for strain values in the 3-direction varied depended on the dilation angle. However, in the loading directions (1 and 2), the variation of dilation angle did not produce any difference.

Fracture energy is another parameter that might cause a variation in the response of concrete model. Finite element analysis (not shown here for brevity here) indicated that the behavior of concrete in equi-biaxial compression for various fracture energy values (0.3, 1.0, and 10.0 lb/in) was independent of the values used for fracture energy. This was due to the fact that the failure mode in this case was the crushing of concrete and it was not related to the tension stiffening of concrete.

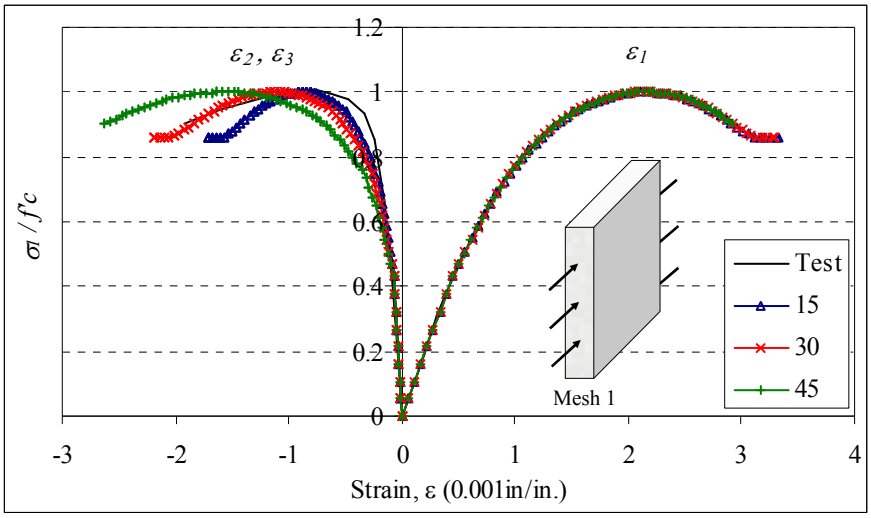

Figure 3.11 Effect of dilation angle

3.7. Pure Bending of Reinforced Concrete Beam

3.7.1. Description of the Experiment

Janney *et al.* [28] investigated the flexural behavior and strength of rectangular beams with different types of tension reinforcement. Beams were divided into five groups with respect to reinforcement type: (1) pre-tensioned reinforcement, (2) post-tensioned grouted reinforcement, (3) post-tensioned unbonded reinforcement, (4) post-tensioned unbonded reinforcement with additional conventional reinforcement, and (5) conventional

reinforcement. Each group consists of beams with different tension reinforcement ratios.

Janney *et al.* [28] tested 19 beam specimens with a cross section of 6x12-in. Longitudinal steel was located in such a way that the effective depth in all beams were approximately 8.3-in. All beams had a length of 10-ft. and were subjected to third point loading. Each beam had a 9-foot long clear span. Prestressing strands were 3/8-in. seven-wire strand and pulled up to 120-ksi. The strands were not stress relieved and exhibit nonlinear behavior at very low load levels. Typical concrete compressive strength was 5500-psi. As the main purpose of the experiment was to investigate the flexural strength of reinforced concrete beams, they attached clamp-on stirrups in the outer thirds of the beams to prevent the shear failure. They monitored deflections and concrete and reinforcement strains.

Test results showed that the behavior of beams were highly affected by the stress-strain relationship of reinforcing steel and the bond properties between concrete and steel. Mid-span deflections tend to be small in the prestressed concrete beams for the service load conditions. However, conventionally reinforced concrete beams had larger deflections than prestressed concrete beams at failure. With an increase of the reinforcement ratio, mid-span deflections at failure tend to be smaller (Janney, Honestad and McHenry 1956).

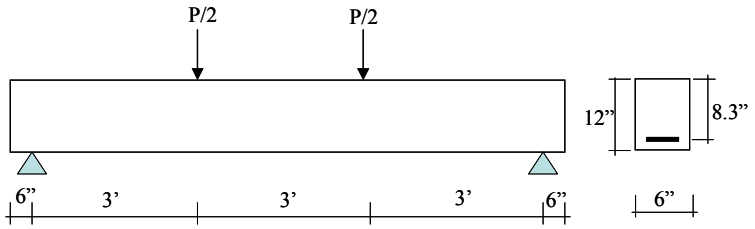

Figure 3.12 Beam dimensions

3.7.2. Description of the Finite Element Model

A finite element model was first generated with ABAQUS/Standard for one of the beams tested by Janney *et al.* [28] consisting of conventional reinforcement and next, analysis results were compared with test results. Eight-node brick elements with reduced integration were used to model concrete. Reposted properties of the beam listed in Table

3.4 were not enough to describe the behavior of concrete using damage-plasticity or smeared cracking model. Some assumptions were made for those parameters required by the concrete models, but which not measured during experiment.

The Modified-Hognestad concrete model was used to define the uniaxial stress-strain relation of concrete under compression. However, the stress-strain relation was assumed linear up to a stress level of $0.45f'_c$. The slope of this line (4722ksi) was assumed to be equal to the elastic modulus of concrete. The dilation angle required in the concrete damage plasticity model was taken equal to 30 degrees. No damage parameters were taken into account in the analysis. The tensile strength of plain concrete and the fracture energy of reinforced concrete were assumed to be equal to 440 psi and 0.01 k/in, respectively. Fracture energy of reinforced concrete is generally larger than that of plain concrete due to the interaction between concrete and rebar. Since no test data was available for the failure ratios of concrete smeared cracking model that were briefly mentioned in the previous verification example, the default values in ABAQUS were implemented. The ratio of uniaxial tensile strength to compressive strength was taken 0.081 (=440/5420). The maximum cracking displacement was obtained as 0.045 in ($=2G_f/f_t$) with the assumption of linear post-cracking response.

Longitudinal reinforcement, 3No8, was modeled as 2D truss element and was embedded into concrete. No slip between concrete and rebar was allowed in the model. Elastic-perfectly plastic material model were used for steel with the yield strength of 56.1 ksi. As mentioned in the description of the experiment above, the outer thirds of the beams were fixed with clamp-on stirrups to prevent the shear failure. Instead, closely spaced stirrups were located in those regions of the beam for modeling purposes. Static, Riks analyses were performed with the load increment and loads were distributed along the width at one-third locations of the beam.

Table 3.4 Major properties of the selected specimen

Beam Group	Reinforcement		Concrete Strength f'_c	Effective prestress, f_{se}	Yield Strength f_y
	Steel	Percent	psi	ksi	ksi
5-0.492	3No8	4.75	5420	0	56.1

3.7.3. Results and Discussions

The sensitivity of finite element results to mesh configuration was first investigated by using 1.5-in. and 3-in. cubic brick elements for concrete. In Figure 3.13 the finite element results obtained with two mesh configurations were compared with the test results for the applied moment normalized with respect to calculated moment capacity versus vertical deflection at the mid-span of the beam. Analyses, which were based on the damage-plasticity model for concrete, were terminated when the longitudinal reinforcement began yielding. As opposed to the tensile response of plain concrete, the analyses results showed that the response of reinforced concrete under tension was not mesh sensitive. This is attributed to the dominant effect of reinforcing steel in the cracked concrete since concrete can carry much less tensile stress than reinforcing steel in the cracked zone.

Figure 3.14 shows the comparison of the beam responses obtained with damage-plasticity and smeared cracked model. Both models provided results in good agreement with experimental results. Even though finite element analyses seem to give a slightly stiffer response, the stiffness of the cracked member was still close to the test results. This might be due to the effect of the tensile strength of concrete that was assumed in the finite element model, as the cracking moment obtained by analysis was slightly larger than obtained by experiment.

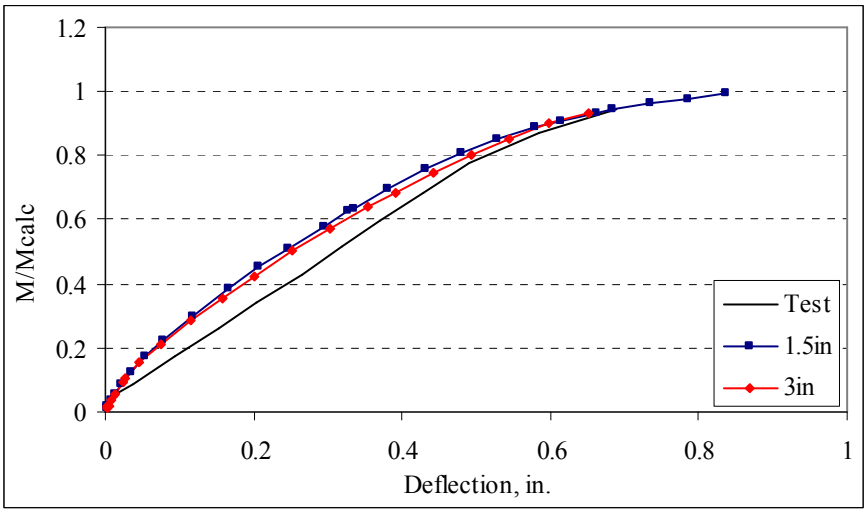

Figure 3.13 Mesh Sensitivity (CDP model)

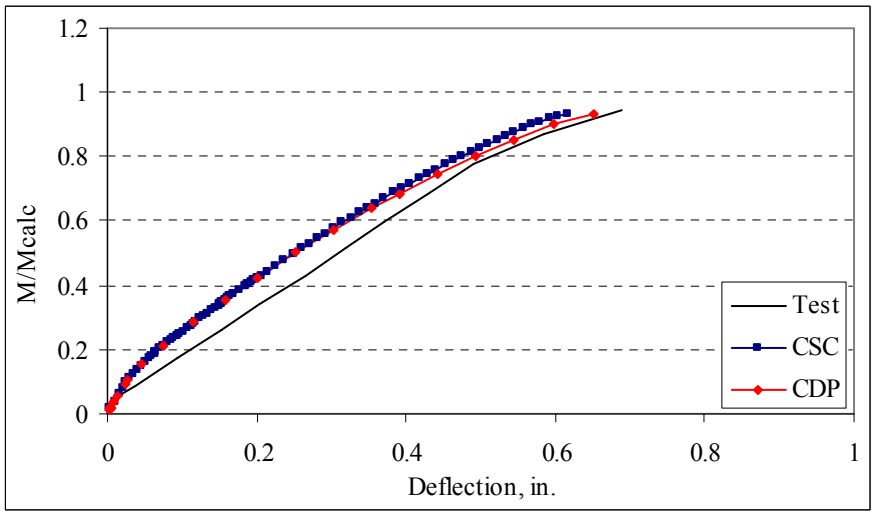

Figure 3.14 Comparison of concrete models

CHAPTER 4

Nonlinear Finite Element Modeling of Prestressed Concrete Spandrel Beams

4.1. Introduction

Nonlinear three-dimensional finite element modeling of precast, prestressed concrete spandrel beams is a challenging task and requires exploration of the effects of material parameters and modeling assumptions. To this end, the numerical results obtained using the commercial software ABAQUS/Standard were compared with existing experimental data. The sensitivity of the spandrel beam response to various parameters such as finite element type, dilation angle, fracture energy, tension stiffening, bearing stress distribution and support representation was investigated. The behavior of precast, prestressed concrete spandrels under vertical loading was found to be sensitive to the type of element, the dilation angle for the concrete, bearing stress distribution at the supports, and deck-tie stiffness. Many of the findings reported are believed to be applicable to other types of reinforced concrete structures.

4.2. Background

Precast, prestressed concrete spandrel beams have been widely used in the perimeter of precast concrete frame buildings, especially for parking garages. The spandrels usually support precast, prestressed concrete doubles-tees, which are used as both deck beams and floor diaphragms, and are supported by column corbels at their ends. Spandrel beams are typically 1.5 to 2 m deep, and they have span lengths ranging from 9 to 15 m, with recent trends focusing on spans as long as 18 m. Web thicknesses are typically 0.2 to 0.3 m. Spandrel beams are often categorized by the features of their configuration which serve to support the deck members. For example, "L-shaped" spandrels have a continuous horizontal ledge (Fig. 4.1), "pocket" spandrels have rectangular cutouts, and “spot corbel” spandrels feature a discontinuous ledge. The latter two configurations provide support only at the locations of the double-tee webs.

The cross section of a spandrel beam is under the combined effects of shear, torsion and bending moment, the latter about the strong axis, which complicates the analysis and

design of these beams. The asymmetric shape of L-shaped cross sections also introduces minor-axis bending moment under vertical loads. The torsional effect stems from the eccentric transfer of vertical loads from the double-tees. Thus, besides vertical deflection, lateral deformation due to the combination of eccentric loading and asymmetric geometry may develop in an L-shaped slender spandrel beam. The lateral deformation has the potential to trigger lateral-torsional instability of the beam under flexure, if it is sufficiently slender, and the presence of prestressing forces further complicates the loading conditions.

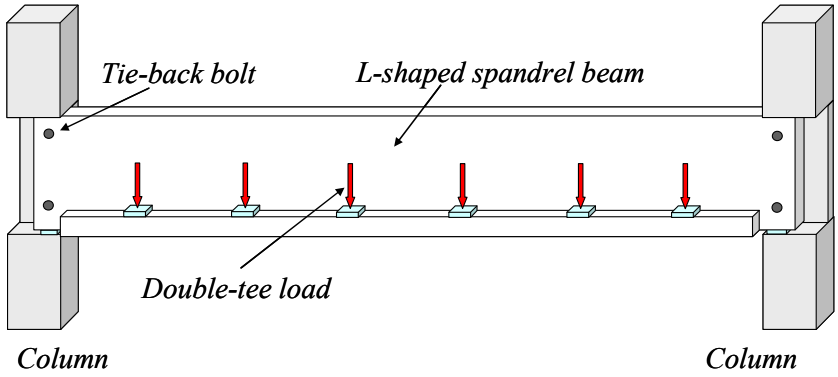

Fig. 4.1. Double-tee loads, tieback forces and support reactions on an L-shaped spandrel beam

To date, most research efforts have been focused on strength and design considerations for precast prestressed concrete spandrels under the combined effects of shear, torsion and bending [30]-[34]. Lateral deformation issues are seldom mentioned in the technical literature for reinforced concrete beams subjected to concentric loading [35]-[40], and no test data are available on the lateral-torsional instability in prestressed concrete beams. In this regard, finite element analyses might provide opportunities for better understanding of the overall behavior of highly slender, L-shaped, prestressed concrete spandrel beams. There are a few research efforts that investigate the response of prestressed concrete spandrel beams through finite element simulations [33]. However, those efforts were intended to verify the accompanying experimental results. Moreover, the finite element simulations are difficult to reproduce given the high sensitivity of some of the spandrel responses to the values of the parameters used in the model.

Consequently, in spite of the huge progress in computer analysis of concrete structures, relying on computer models to predict the lateral deformations of precast, prestressed concrete spandrels can be risky because such models require validation with experimental data. Therefore, this study contributes to the understanding of the models and their sensitivity to the parameters involved so as to enable computer simulation of the behavior of spandrel beams. A three dimensional finite element simulation, which includes realistic material behavior, inherently introduces some numerical and modeling challenges. Thus, the other contribution of the study presented herein is a discussion of the challenges and potential pitfalls associated with three-dimensional finite element simulation of prestressed concrete spandrel beams using the commercial software, ABAQUS/Standard [41] and to suggest some ways to avoid these problems. Although important in its own right, the conclusions reached in the analysis of spandrel beams have broader implications. The experiences described here in the context of spandrel beam analysis by finite element should be equally applicable to other reinforced and prestressed concrete structures and they constitute the principal motivating factor to prepare this manuscript.

4.3. Scope of the Study

Due to the nature of the problem, the finite element model of a spandrel beam should incorporate both material and geometric nonlinearities. ABAQUS/Standard is capable of solving extensively nonlinear problems, comprising both geometric nonlinearity and a complex material model for concrete that includes plasticity in compression and cracking in tension. The geometric nonlinearity should be considered to not only to estimate deflections accurately, but also to predict changes in internal forces due to distortion of member geometry. Linear analysis theory is based on the assumption that deflection remains small after loading and the equilibrium equations can be established in the undeformed shape of the member. However, a slender spandrel beam might develop sufficiently large deformations that affect internal equilibrium under combined loading effects, and small deflection theory may lead to inaccurate estimation of deflections.

Material nonlinearity is another essential factor that needs to be considered in the finite element analyses of concrete. Concrete cracking reduces both torsional and flexural stiffness of the section and causes significant increase in the deflections. Although prestressing forces tend to keep concrete uncracked under flexure, this will occur only if the loading is sufficiently low. A relatively accurate material model for concrete should be used to capture concrete cracking and corresponding deformations when the ultimate capacity is to be determined. ABAQUS/Standard offers several concrete models defined with various parameters such as dilation angle, fracture energy, and tension stiffening. The damage-plasticity model of concrete was implemented in this study and the sensitivity of spandrel response to the pertinent parameters for that model will be discussed.

4.4. Description of the model problem

The finite element modeling techniques investigated with ABAQUS/Standard were first compared with the results of full-scale tests found in literature [32]. The main objective of these experiments was not to evaluate the magnitude of lateral deflections in spandrel beams, but to investigate the influence of alternative transverse reinforcement schemes on the torsional resistance of spandrel beams. However, data generated in this experimental study is useful to analyze the sensitivity of the spandrel beam deflections to various modeling parameters as well.

Fig. 4.2 shows the test setup. The 13.7 m (45 ft) long specimen (specified as SP4 in [32]) with a depth of 1.5 m (5 ft) and a web thickness of 0.2 m (8 in.) was chosen in the present study for verification of the finite element model. The cross section of the spandrel ledge was 0.2 × 0.2 m (8 × 8 in.). The ledge was terminated at a 0.3 m (12 in.) distance from both ends of the spandrel web. Low relaxation, 1860 MPa (270 ksi), 12.7 mm (½ in.) diameter strands were used in this specimen, as seen in Fig. 4.3. The cylinder strength for concrete in compression was measured as 49.6 MPa (7.19 ksi). A 152 × 152 mm (6 × 6 in) - W4 × W4 mesh of welded wire fabric was placed on both sides of the spandrel web. The web also included 10M (No. 3) L-shaped bars at 0.15 m (6 in.)

spacing. The ledge reinforcement was provided as 13M (No. 4) C-shaped bars with a 0.2 m (8 in.) spacing. The entire reinforcement assembly is not shown for brevity, but can be found in [32].

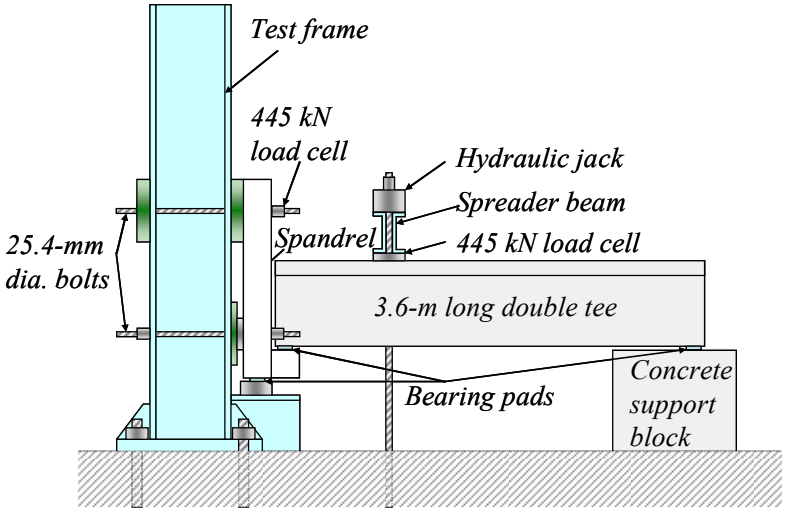

Fig. 4.2. Test setup, adapted from [32]

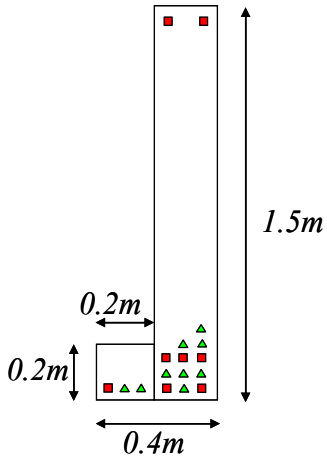

▲ *12.7 mm dia. straight strand pulled up to 100 kN*

■ *12.7 mm dia. straight strand pulled up to 70 kN*

Fig. 4.3. Strand details, adapted from [32]

The web of the spandrel beam was laterally connected to the vertical support at the ends with 25.4 mm (1 in.) diameter bolts. The bolts were located 0.15 m (6 in.) away from the ends and 0.3 m (12 in.) away from the top and bottom. Teflon-coated bearing pads were provided to reduce friction at the end supports, and the spandrel web was

connected to the double-tee deck by means of embedded steel plates. The location of these plates corresponds approximately to the mid-height of the beam. Due to the self weight of the beam and testing equipment, the support reaction was measured to be 98 kN (22 kips) at the beginning of the test. Except for three initial cycles of loading and unloading, monotonic loading was applied to the beam in increments. Loading during the increments was kept constant for 5 to 10 minutes during testing for observations except for the third initial loading-unloading cycle during which there was an increment with a 24-hour duration when the spandrel was loaded at the estimated value of full factored loading. There were nine loading points with 1.5 m (5 ft) spacing on the ledge and the first loading point was 0.5 m (1 ft 8 in) away from the ledge ends [32]. The test results showed that the maximum lateral deflection was approximately two times larger than the vertical deflections. Even though lateral stability was not investigated in the experiments, based on these results, it might be concluded that slender spandrels may be prone to lateral stability problems [32].

The behavior of the L-shaped, precast, prestressed spandrels was also investigated through nonlinear finite element analysis in [33], an accompanying study to [32]. As with the experimental study, the main objective was to show the feasibility of open web reinforcement in L-shaped spandrels. The model developed for the slender spandrels was used to evaluate compact spandrels for various configurations of web reinforcement. The ANATECH Concrete Analysis Program (ANACAP) was used to model the nonlinear behavior of spandrel beams. The concrete model provided in ANACAP is based on the smeared cracking approach. Furthermore, the sensitivity of the lateral deflections in spandrel beams to various modeling parameters was not reported in [33].

4.5. General description of finite element model

In the present study, a finite element model of the spandrel beam tested at North Carolina State University was generated in ABAQUS/Standard using carefully selected geometric and mechanical properties. The results of this analysis were required as a basis for investigation of optimal model parameters.

Due to the symmetry of the specimen with respect to the mid-span, only one-half of the spandrel was modeled using ABAQUS/Standard, as shown in Fig. 4.4. Symmetry boundary conditions were assigned to the mid-span surface of the spandrel beam. The end of spandrel beam was fixed at the mid-point of the bottom surface of the web against vertical displacements at the bearing pads. However, since restraining only one point in such a three-dimensional finite element model may lead to singularity problems, the bottom surface 0.3 × 0.2 m (12 × 8 in.) of the web at the support region was forced to remain plane during analysis by defining constraint equations. Lateral tiebacks were taken into account as spring elements. They were provided at a distance 0.3 m (12 in.) away from the top and the bottom of the web, and 0.15 m (6 in.) from the end. The value of spring stiffness was assumed to be equal to 100 kN/mm (570 k/in) after computing the axial stiffness (*EA/L*) for one-meter long tie-back bolts with a diameter of 25mm (1 in.). Also, deck-ties comprising steel plates 76 × 152 × 9.5 mm (3 × 6 × 3/8 in.) prevented lateral displacement at the mid-height of the spandrel. Two deck ties were located at the mid-height of the front face of the spandrel as shown in Fig. 4.4. To accommodate for a finite size of the connections, each deck-tie was modeled using two adjacent spring elements with an axial stiffness of 1900 kN/mm (10,875 k/in) each, corresponding to one-half of the steel plate stiffness (*EA/L*) value.

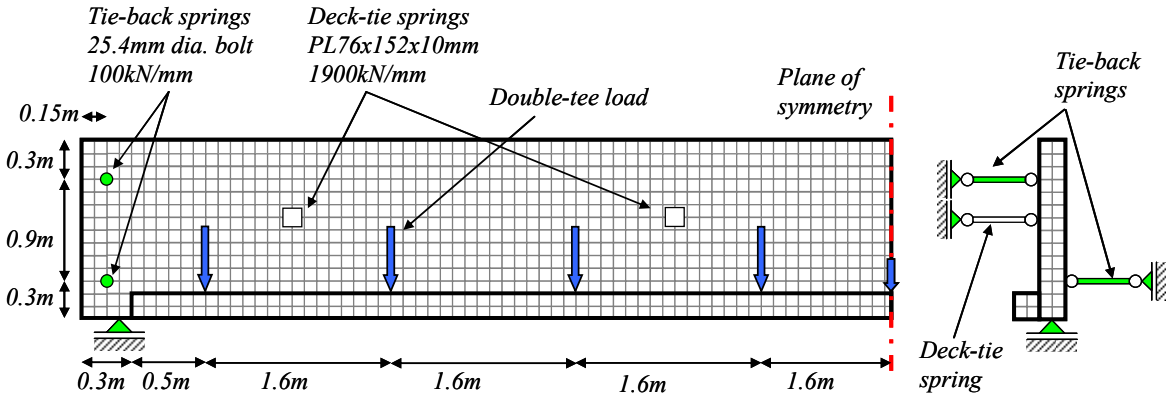

Fig. 4.4. Finite element mesh

The concrete was modeled using 8-node brick elements with reduced integration and hourglass control. The maximum element size for concrete brick elements was around

100 mm (4 in.). Two-node linear 3D truss elements were used to model both non-prestressed reinforcement and prestressing strands. Typical element size for reinforcement, welded wire mesh and strands were 50 mm (2 in.). To properly model transfer length of strands in the end regions, the strands were divided into five segments whose cross sectional area gradually increased from the tip of a strand along the transfer length. The transfer length was assumed to be equal to 0.51 m (21 in.) and loss of prestressing force was assumed to be 15%, which was reported in [33]. The prestressing forces were introduced by defining initial stresses in the 3D truss elements representing the strands, which is an option available in ABAQUS/Standard. Rebar and prestressing strand were embedded into the concrete solid, assuming perfect bond between strand and concrete [41]. The interaction between cracked concrete and reinforcement that is known as 'bond-slip' was indirectly included by modifying the post-peak behavior of concrete (i.e., the so-called 'tension stiffening' effect for concrete in tension). The concept of tension stiffening will be discussed in more detail in Section 4.7.

Elastic modulus of concrete was determined as 33.1 GPa (4800 ksi) according to Sec. 8.5.1 of the ACI Committee 318 building code document [42] for the reported concrete compressive strength of 49.6 MPa (7.19 ksi). The damage-plasticity model for concrete was preferred in this study to take into account the behavior of cracked sections (see Section 4.7 for details). The dilation angle was taken as 55 degrees. Default values were used for the rest of the parameters required by ABAQUS/Standard to define the damage-plasticity model. These parameters are 1.16 for the ratio of initial equibiaxial compressive yield stress to initial uniaxial compressive yield stress and 0.667 for the ratio of the second stress invariant on the tensile meridian to that on the compressive meridian [41]. The stress-strain relationship for concrete under uniaxial compression was assumed as shown in Fig. 4.5. Post-peak behavior of concrete in tension was described by means of concrete fracture energy of 1.75 kN/m (0.01 k/in) and a tensile strength of 3.5 MPa (0.51 ksi). Fracture energy defines the energy to form a unit area of crack. For example, for plain concrete with a compressive strength of 40 MPa (5.8 ksi), the value of the fracture energy is around 0.12 kN/m (0.0007 k/in) [41]. However, reinforced concrete involves much higher fracture energy than plain concrete due to the influence of the

reinforcement. A detailed discussion of fracture energy for plain and reinforced concrete will be presented in Section 4.7

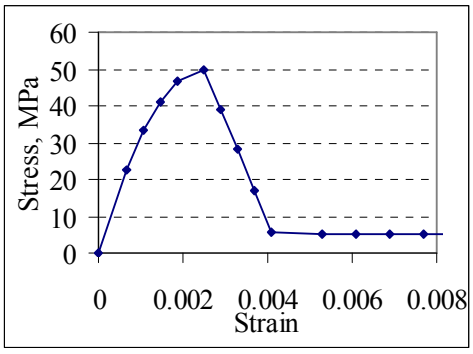

Fig. 4.5. Stress-strain relationship for concrete

The yield strengths of mild steel, welded-wire-mesh reinforcement and prestressing strands were taken 445 MPa (64.5 ksi), 675 MPa (98 ksi) and 1689 MPa (245 ksi), respectively. The material model for all steel elements was based on elastic-perfectly plastic behavior. The elastic modulus was assumed to be 200 GPa (29,000 ksi).

Concrete damage due to loading and unloading of the specimen during the experiment was not considered in the model and monotonic loading was applied. At some level of loading, concrete weakens after crushing in compression or cracking in tension. Thus, when unloading occurs in the tension or compression softening regions, concrete damage results in a degradation of initial elastic stiffness. This is of particular importance for cyclic loading. But such effect is generally insignificant for monotonic loading and was neglected in this study by assuming constant properties for the elastic component of concrete material model.

Finally, the spandrel beam was first analyzed with a general static procedure for the self-weight and the initial conditions due to the prestressing forces. The subsequent analysis was performed with Riks procedure in ABAQUS/ Standard for double-tee loads acting at the spandrel ledge.

The Riks (arc-length) method allows evaluation of the load-deflection path of a nonlinear structural response including descending branches. The method can efficiently account for material and geometric nonlinearity and detect unstable postbuckling

behavior, and an additional equation is necessary for the solution of simultaneous equations governing the problem. Both the magnitude of the load and displacements are unknown in the Riks method. This equation describes the arc length of the load-displacement path. The load magnitude P_{total} is defined with equation (4.1) in which P_o is the dead load, which is applied to the structure at the beginning of the Riks analysis and remains constant, P_{ref} is the reference load vector and λ is an unknown load magnitude factor [41]. Nonlinear equilibrium equations are typically solved iteratively using Newton's method at each Riks step. As this method is neither displacement nor load controlled, a maximum value for the load proportionality factor or the displacement value is necessary to specify the end of the procedure.

$$P_{total} = P_o + \lambda(P_{ref} - P_o) \tag{4.1}$$

4.6. Geometric description

4.6.1. Element sensitivity

For three dimensional applications, the element type selected for the concrete plays an important role in the finite element analysis, particularly if both geometric and material nonlinearity are present. Isoparametric elements in three-dimensions of the first and second order were used in this work. First order elements maintain constant strain and the 8-node element in three dimensions is one of the elements in this class. However, second-order elements include some or all linear strain components and the 20-node element in three dimensions represents this class of elements. For this reason, the 20-node elements provide smoother deformed shape in bending. However, both elements inherently introduce shear locking for bending of thin members and result in very stiff response. To solve this problem, reduced integration is employed and the number of integration points reduced from 8 to 1 for the 8-node brick element and from 27 to 8 for the 20-node brick element [43]. On the other hand, the 8-node brick element with reduced integration method exhibits the so-called kinematic modes since it uses only one integration point. However, this problem can be overcome using hourglass control. Similar difficulties plague the 20-node element with reduced integration. But, in this

case, kinematic modes disappear for an assembly of elements.

The spandrel beam model described above was analyzed using three different element types for the concrete, the 8-node brick with reduced integration, the 8-node brick with full-integration and the 20-node brick with reduced integration. Results for these three models were compared with the experimental results for lateral deflections at the top and the bottom of the mid-span section, the vertical deflection at the mid-span and the rotation at the quarter span (Fig. 4.6). The bottom of the mid-span section deformed in the outward direction (shown as negative) and the top went inward (shown as positive). In this figure and all subsequent figures, the horizontal plateaus in the force-deformation responses obtained from the tests correspond to increasing deflections at sustained constant loads, and the finite element model developed for this study did not include the effect of creep in concrete [32]. Additionally, initial deflections and support reaction of 98 kN (22 kips) due to gravity and prestressing were excluded from all force-deformation curves.

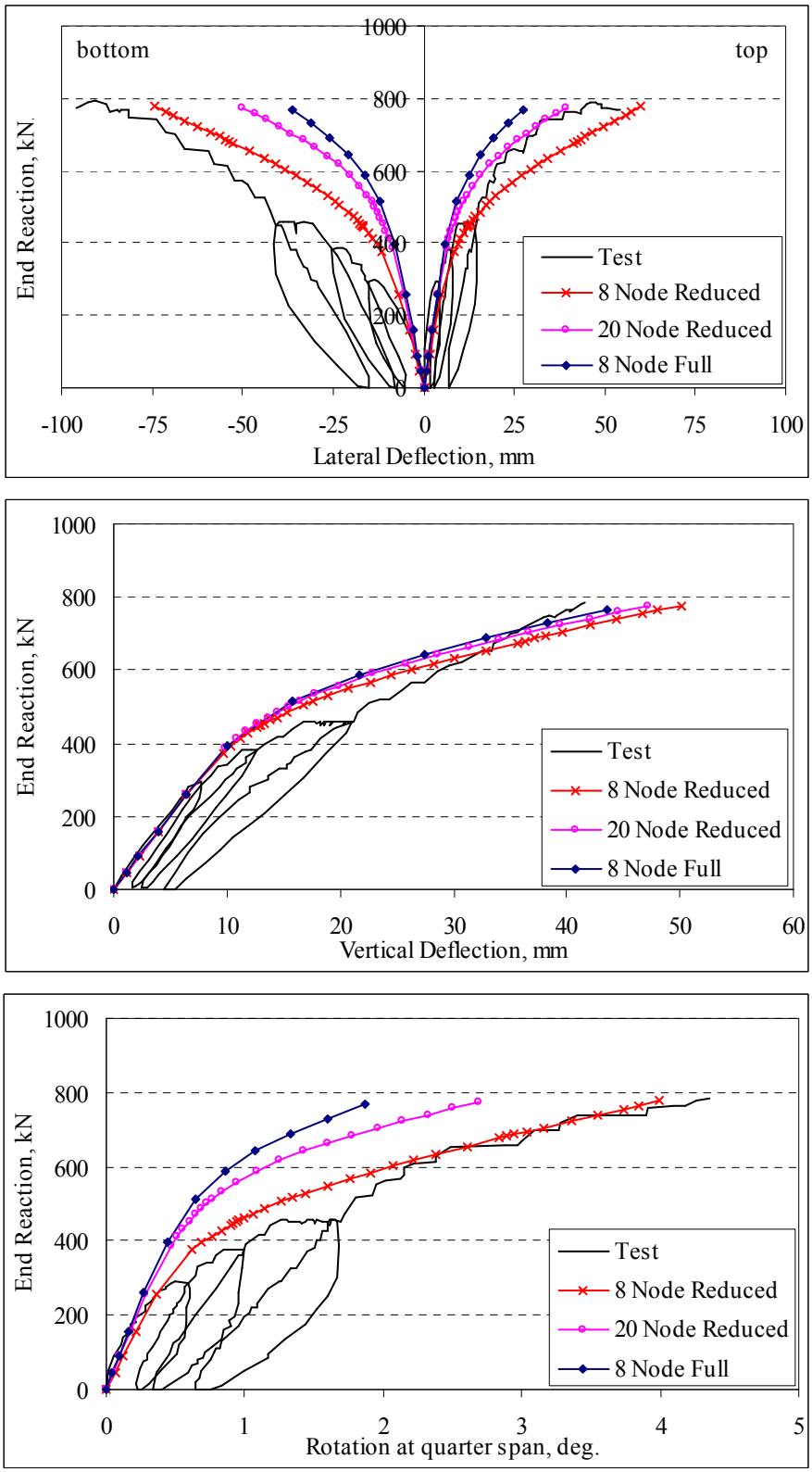

Fig. 4.6. Effect of finite element type

The arguments mentioned above, related to element type, were clearly observed in the response of spandrel beam model for the three different element types of the concrete solid. The model based on the 8-node brick element with full integration was prone to shear locking and resulted in very stiff response for lateral displacement. This phenomenon occurs because the web of spandrel beam is quite thin and has smaller stiffness, but is more prone to shear locking in the lateral direction than in the vertical direction. The shear locking effect was not observed in the vertical direction supporting the argument that shear locking occurs most prevalently in the bending of thin members.

The 20-node brick element with reduced integration also resulted in slightly stiffer response than the 8-node brick with reduced integration. This behavior seems to indicate that, for this element, reduced integration does not eliminate shear locking completely. Furthermore, CPU time required for the analysis with 20-node brick element was considerably longer than for the 8-node brick element with reduced integration. Thus, the 8-node brick element with reduced integration was found to give the most accurate results with the least computational cost.

4.6.2. Mesh sensitivity

The sensitivity of the spandrel beam response to various mesh configurations was also investigated. Two different meshes were generated in ABAQUS/Standard, as shown in Fig. 4.7. The maximum element sizes in Meshes-1 and -2 are 100 mm (4 in.) and 200 mm. (8 in.) respectively. In both configurations, the web and ledge of the spandrel consist of 100 mm (4 in.) thick elements. The 8-node brick elements with reduced integration were implemented for these mesh sensitivity analyses.

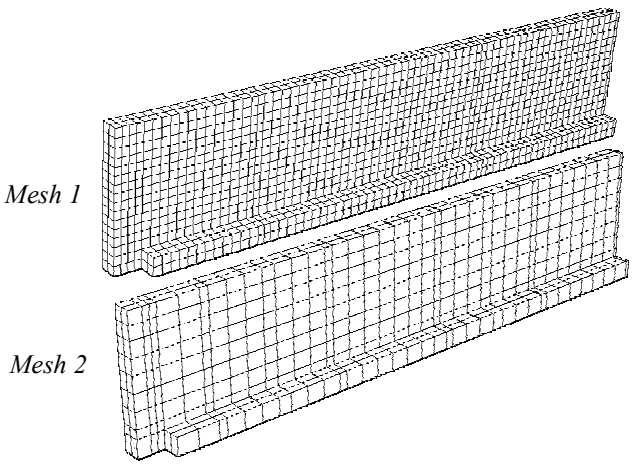

Fig. 4.7. Mesh configurations

The results of mesh sensitivity analyses, as seen in Fig. 4.8 show that mesh refinement in the longitudinal direction of the spandrel beam has negligible effect on the response for rotation, lateral and vertical deflections. In some cases, using a finer mesh results in narrower crack bands and cracked region with numerically negligible stiffness gets localized. Hence, singularity in the system of equations might occur during the analyses. To avoid such problems, it is essential to ensure that each concrete solid element is connected to at least one rebar element, so the concrete elements cannot be defined too small. This will allow the cracked concrete elements to be restrained by the interacting rebar and to associate its stiffness with a broader region rather than to get localized. Such meshing approach of concrete solid elements can be easily performed in highly reinforced concrete members. The finite element mesh should also be assigned in such a way that elements maintain reasonable aspect ratios. Large aspect ratios might lead to a change in the material behavior in the different directions. These recommendations are valid for not only precast, prestressed concrete spandrel beams, but also other types of prestressed or reinforced concrete structures.

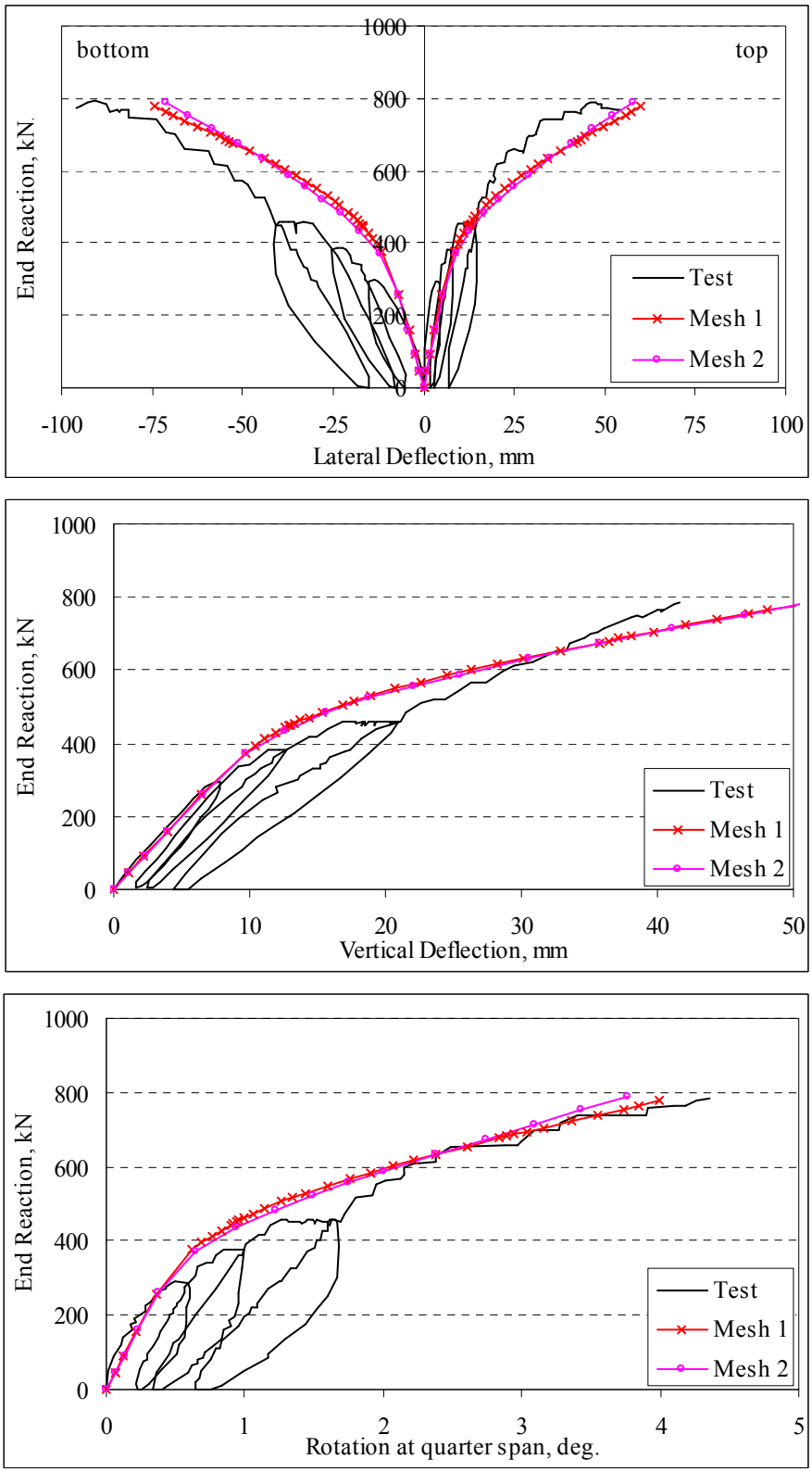

Fig. 4.8. Mesh sensitivity

4.7. Mechanical properties

Concrete, an inhomogeneous material consisting of aggregate and cement in various ratios, exhibits very complex material behavior. Defining a material model representing the real response of concrete can be a quite difficult task. Such material model should include various unique features of concrete such as cracking, crushing, stiffness degradation, volumetric change, concrete-rebar interaction etc. Unfortunately, some of these aspects of concrete have not been well-understood yet. Experimental measurements show that even fundamental properties of concrete such as elastic modulus, compressive strength, and tensile strength vary over broad ranges. Concrete also experiences large volumetric changes under compression, which is unique to granular materials. Predicting the initiation and development of cracking in concrete is also challenging [44], [45].

Before presenting the influence of various material parameters on the response of spandrel beams, we will first shortly describe "concrete damage-plasticity model", which is a material model for concrete provided in ABAQUS/Standard. The model comprises concrete crushing in compression, cracking in tension and "dilation angle", which is a term defining inelastic volumetric change in granular materials. In this model, the tensile behavior of concrete after cracking, that is, the so-called "tension stiffening", simulates the interaction between reinforcement and cracked concrete. In ABAQUS/Standard, one way of defining the tension stiffening is to apply a cracking criterion based on "fracture energy". In this section, detailed descriptions of dilation angle, tension stiffening and fracture energy will be presented, and subsequently the sensitivity of the spandrel beam response to these parameters will be investigated.

4.7.1. Concrete damage-plasticity model

Properly adapted plasticity theory can be used to define the behavior of concrete even though the theory was originally developed for metals. It is so because it has been found that irreversible deformations of concrete due to micro-cracking might be described by plasticity theory [44]. Most of the plasticity models are incremental in the sense that the

total strain rate is the sum of elastic and plastic strain rates and specification of the latter is a part of the theory. A flow rule sets the relationship between the stress and plastic strain rate, and a yield surface defined in stress space describes the condition for the initiation of yielding. A hardening rule shows how the yield surface and the flow rule change with an increase of deformation. Unlike classical plasticity models, the concrete damage-plasticity model also includes a scalar damage parameter which represents degradation of stiffness with plastic deformations. This feature is particularly important when the structure is subjected to cyclic loading [41]. The concrete damage-plasticity model in ABAQUS/Standard relies on the models proposed by Lubliner et al. [46] and by Lee and Fenves [47], [48]. The model is based on the limit states of concrete crushing in compression and cracking in tension. The model assumes non-associated potential plastic flow which is based on the Drucker-Prager function [41]. The model requires definition of parameters related to plasticity, compressive and tensile behaviors of concrete.

4.7.2. Fracture energy sensitivity

When cracking is present, the tensile strength and the elastic modulus are not enough to characterize the behavior of concrete in tension. To describe the post-peak behavior in tension the fracture energy, G_f, which is a concrete material property, defined as the energy needed to form a unit area of crack, is used. In general, fracture energy values for pure concrete vary with respect to the aggregate size and the compressive strength of the concrete [49]. The presence of reinforcement drastically increases the concrete fracture energy [50]. Being dependent on the amount and details of reinforcement, fracture energy values for reinforced concrete may vary over a broad range and there is no commonly accepted value. Thus, it is important to understand how different values of fracture energy affect the overall response of spandrel beams.

For plain concrete, the uniaxial tension test and the three-point-bend notched beam test are typically used methods to measure the fracture energy. In the uniaxial tension test of concrete, fracture energy, G_f, can be computed by integrating the area under the stress-cracking displacement curve as follows:

$$G_f = \int_o^{\delta_{max}} \sigma_t d\delta_t \tag{4.2}$$

where σ_t is tensile stress as a function of displacement , δ_t is cracking displacement and δ_{max} is the maximum cracking displacement [51]. However, uniaxial tension tests are quite challenging and require sophisticated testing apparatus. A simpler method to measure the fracture energy relies on the total work of fracture in the three-point bend notched beams. The fracture energy is equal to the work required to fracture the notched beam, K_f divided by the area of the fracture surface $b(d-a_o)$ where b and d are the width and the depth of the specimen and a_o is the notch size.

$$G_f = \frac{K_f}{b(d - a_o)} \tag{4.3}$$

Proper values for fracture energy play an essential role in the convergence of analyses for applications in ABAQUS/Standard. If the fracture energy is assumed to be too small, the solution cannot converge immediately after the member cracks. The influence of fracture energy on the response of the spandrel beam was studied using three different values, 17.5 kN/m (0.1 k/in), 1.75 kN/m (0.01 k/in) and 0.175 kN/m (0.001 k/in). The vertical and lateral displacements at the mid-span and rotation at the quarter span obtained with each analysis were plotted in Fig. 4.9. When the fracture energy of concrete was assumed to be equal to 0.175 kN/m (0.001 k/in), corresponding to the case of pure concrete, the solution was unable to converge immediately after concrete cracking. When the fracture energy was increased to 1.75 kN/m (0.01 k/in), convergence of the solution was maintained. In addition to this, using even larger value such as 17.5 kN/m (0.1 k/in) introduced only small variation in the results. This observation means that the contribution of the concrete in tension to overall capacity of the spandrel beam was relatively small, in comparison to those of the reinforcement and concrete in compression.

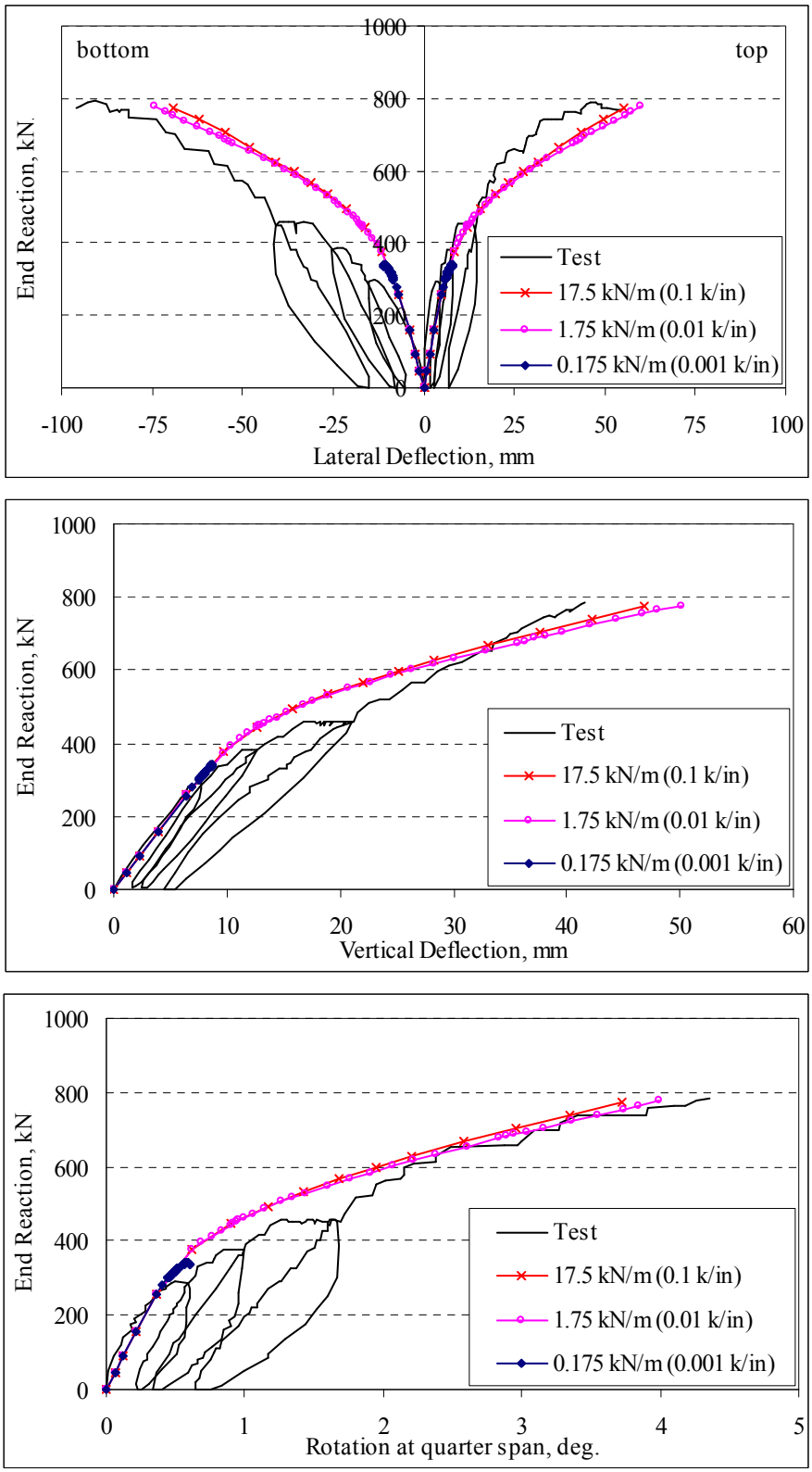

Fig. 4.9. Effect of fracture energy

4.7.3. Tension stiffening sensitivity

Plain concrete subjected to tension exhibits softening behavior in the post-peak regime. However, concrete in a cracked reinforced concrete member displays different characteristics than does plain concrete. By means of local bond-slip behavior, the concrete between cracks becomes stiffer than plain concrete due to the effect of reinforcement [50]. As mentioned in Section 4.5, reinforcing bars were modeled using one-dimensional truss elements which were embedded into continuum elements of concrete. Thus, translational degrees of freedom for this one-dimensional element were restrained at a bar node by those of the continuum element. The implication is that the interaction between cracked concrete and reinforcing bar, such as load transfer and bond-slip behavior, was ignored. Even though this implicit behavior contradicts the real situation, this interaction can be introduced into the concrete model approximately by means of "tension stiffening". The term of “tension stiffening” might be considered misleading, because it is used to define the softening regime of reinforced concrete in tension. However, the softening regime of reinforced concrete is stiffer than that of plain concrete.

ABAQUS/Standard provides a couple of ways to define tension stiffening for the damage-plasticity model of concrete. One way is to specify a post-cracking stress-strain relation for concrete in tension, and the other way is to apply a fracture energy criterion. In the first method, cracking strains and stresses are provided to model the tensile stress-strain curve beyond the elastic region. The cracking strain is calculated as the total strain minus the elastic strain. In the second method, the fracture energy model can be expressed in the form of either a failure stress-fracture energy relation or a failure stress-cracking displacement relation. Assuming a constant value for the fracture energy generally means that there is a linear loss of tensile strength with displacement after cracking, and this phenomenon follows because the fracture energy is equal to the area under the failure stress-displacement curve. Tension stiffening can also be defined with a multilinear relationship between cracking displacement and stress in such a way that the fracture energy remains the same as in the linear case.

The effect of tension stiffening with linear and bilinear relationships was investigated

through finite element analysis. The 8-node brick element with reduced integration was used for the concrete solid. Concrete fracture energy of 1.75 kN/m (0.01 k/in) and tensile strength of 3.5 MPa (0.51 ksi) give a maximum cracking displacement of 1 mm (0.04 in.) for the linear case and 2 mm (0.08 in.) for the bilinear case, as seen in Fig. 4.10. The area under each line yields the same value for concrete fracture energy, namely 1.75 kN/m (0.01 k/in). Linear and bilinear assumptions for cracking displacement-stress relation were compared with the assumption of fracture energy of 1.75 kN/m (0.01 k/in). The results of the finite element analyses are not presented here for brevity since the variations in results for the different tension stiffening assumptions are negligible. Tension stiffening defined with fracture energy and linear cracking displacement-stress relation provided the same results. However, the bilinear cracking displacement-stress assumption slightly reduced the stiffness of the spandrel beam in both vertical and lateral directions in the post-cracking region. Therefore, linear relationship for cracking displacement-stress relation with the fracture energy of 1.75 kN/m (0.01 k/in) was selected as the most appropriate assumption for concrete in the analyses.

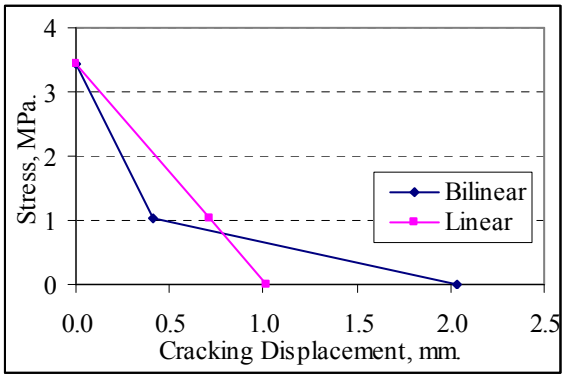

Fig. 4.10. Assumptions for tension stiffening

4.7.4. Dilation angle sensitivity

In contrast to metals, a brittle material like concrete tends to change its volume beyond its elastic limit due to cracking and slip along cracked surfaces. This change in the volume is generally called as "dilation". The dilation characteristic of concrete drastically affects the confinement pressure activated in a reinforced concrete member.

Therefore, the axial stress-strain behavior of concrete in compression greatly depends on the dilation characteristic. An increase in the dilation leads to more confinement and eventually a stiffer stress-strain relation [52]. In the concrete-damage plasticity model for concrete, the dilation angle represents plastic distortion. With an increase of the dilation angle, the concrete behaves in a more ductile manner.

The dilation angle is one of the parameters required for ABAQUS/Standard to define the plastic flow potential. To investigate the sensitivity of the spandrel beam response to the dilation angle, a series of finite element analyses were performed for three different dilation angles (55, 45 and 35 degrees). The 8-node brick element with reduced integration was used for concrete in these models. As shown in Fig. 4.11, lateral and vertical deformations at the mid-span of the spandrel beam depend heavily upon the value used for the dilation angle. As expected, the dilation angle has no impact on the response of the spandrel beam in the elastic regime. The stiffness of the cracked beam, however, reduces with the decrease of dilation angle. Lateral deformations at the mid-span and rotation at quarter span are more sensitive to the value of dilation angle than the vertical deformation at the mid-span. The dilation angle of 55 degrees should be used to describe the behavior of confined concrete in the spandrel beam deforming in the lateral direction since both reinforcement and prestressing provides confinement for the concrete.

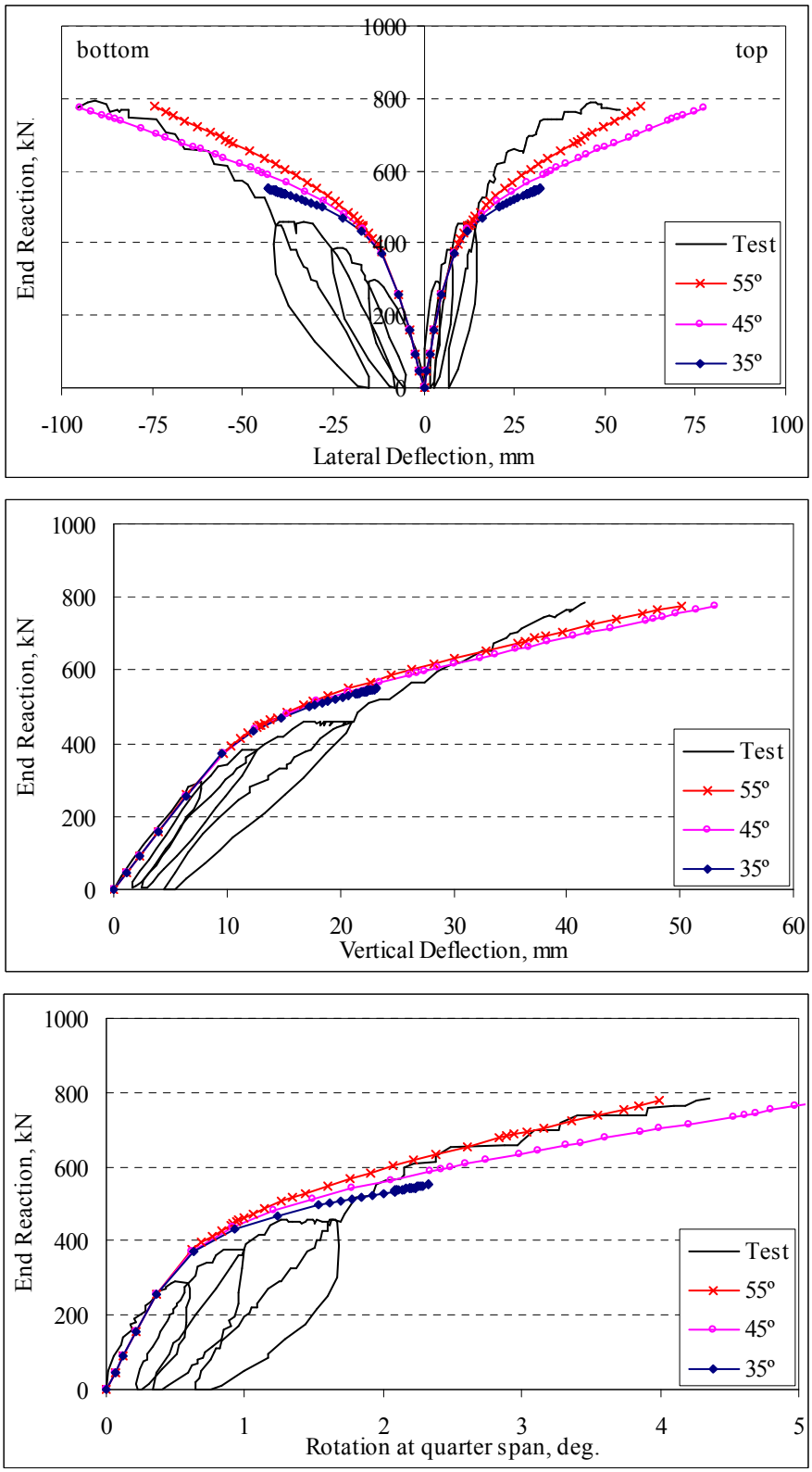

Fig. 4.11. Effect of dilation angle

4.8. Distribution of bearing stress

A spandrel beam carries vertical loads transferred from double-tee webs resting over the spandrel ledge. Both spandrel beam and double-tee beams deform and, depending on the relative angle of rotation in their contact area, the manner in which loads are transferred by the double-tees might vary. For example, for low load magnitudes the relative angle along the spandrel beam is small and, in this case, double-tee loading might be defined as uniform pressure over the spandrel ledge. However, large sectional deformations of the spandrel beam relative to the double-tees might cause double-tee loads to be transferred by means of a triangular bearing stress distribution. The distribution can approach concentrated loading for very large sectional rotations, as depicted in Fig. 4.12.

The distribution of bearing stresses at the supports of the double tees can be simulated by finite element analysis, as long as the double tees are modeled as deformable members and contact elements are defined over the support surfaces. Otherwise, a priori decision must be made regarding the distribution of these bearing stresses. Moreover, the stress distribution also changes the magnitude of loading eccentricity. The larger the eccentricity, the more rotation and lateral displacement the spandrel beams undergo.

Finite element simulations were performed to evaluate the sensitivity of the spandrel beam model to various patterns of bearing stress distribution, as depicted in Fig. 4.12. The results of the finite element analyses are plotted in Fig. 4.13 for reaction at the support vs. rotation at the quarter span and lateral and vertical displacements at the mid-span of the spandrel beam. Rotation and lateral displacements of the spandrel beam are highly sensitive to the pattern of bearing stress distribution. Nevertheless, vertical deflection at the mid-span was not significantly affected by the change in bearing stress distribution. Triangular bearing stress distribution was adopted throughout this study as it appears to provide the most accurate pattern for a deformed spandrel beam.

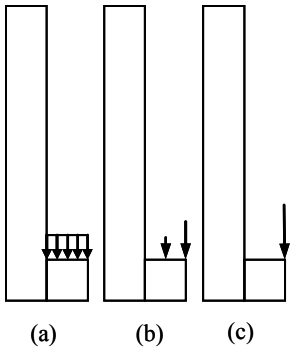

Fig. 4.12. Double-tee bearing stress distribution; (a) uniform, (b) triangular, (c) concentrated

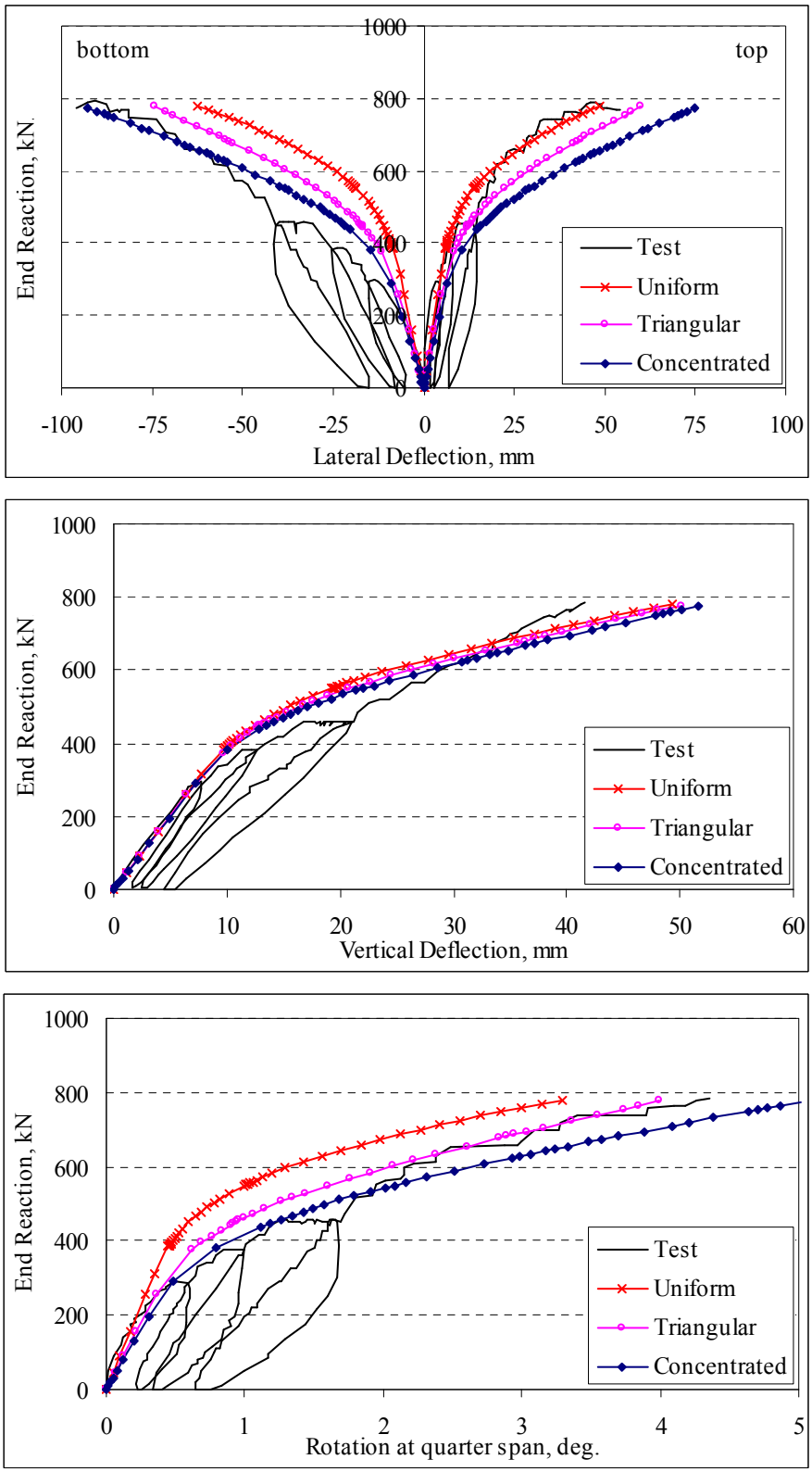

Fig. 4.13. Effect of bearing stress distribution

4.9. Boundary conditions

The response of the spandrel beam was highly dependent upon the boundary conditions. As seen in Fig. 4.4, the bottom web surface at the end of the spandrel beam was fixed against vertical displacements only. Two tie-back bolts at each end of the spandrel beam were modeled using spring elements, which restrain only lateral displacements at these locations. Lateral restraints were also provided by deck-ties at the mid-height of the interior face of the spandrel web, which can affect measurably the lateral displacements.

4.9.1. End supports

The spandrel web rests on frictionless bearing pads at both ends, which introduces vertical restraint to the bottom surface of the web. The supported surface at the bottom of the web end might be modeled in various ways and the comparison of two supporting approaches was made here. One way is to fix the entire surface against vertical displacements (i.e., "surface restraint"). The other way is to fix a single point in the supported surface (i.e., "point restraint") and to let the beam rotate around it. To avoid singularities caused by concentrated reactions, the second method requires adding a constraint equation that forces the entire contact area to remain flat and prevents large distortions of the bearing surface from the concentrated reaction force. Fig. 4.14 shows the effects of point and surface restraints on the overall response of the spandrel beam. Entire surface restraints provided constraint on end rotation and introduced additional moment resistance at the support. Such restraint led to concrete damage around the support zone and resulted in stiffer response for spandrel rotation and deformations than did point restraints. In terms of numerical cost, point restraints provided faster convergence for solution than did surface restraints since no tensile cracks developed at the support.

4.9.2. Tie-back springs

The axial stiffness of spring elements for tie-back bolts was assumed to be equal to

100 kN/mm (570 k/in) as mentioned in Section 4.5. To evaluate the sensitivity of spandrel beam response to this stiffness value, finite element simulations were performed for fixed and spring connections. The results of these analyses are not shown for brevity because the axial stiffness of tie-back bolts had no effect on the spandrel beam behavior even for the loads approaching ultimate capacity. Small increases in rotation and lateral deformations were observed in the elastic region, which shows that the torsional stiffness of the uncracked spandrel beam depends on the stiffness value of the tie-back springs. However, the impact of tie-back spring stiffness decreases as spandrel deformation increases, and both models converge to the similar results once torsional cracks developed at the end zone of the spandrel. The vertical deformation at the mid-span was not affected by the axial stiffness value assumed for the tie-back springs.

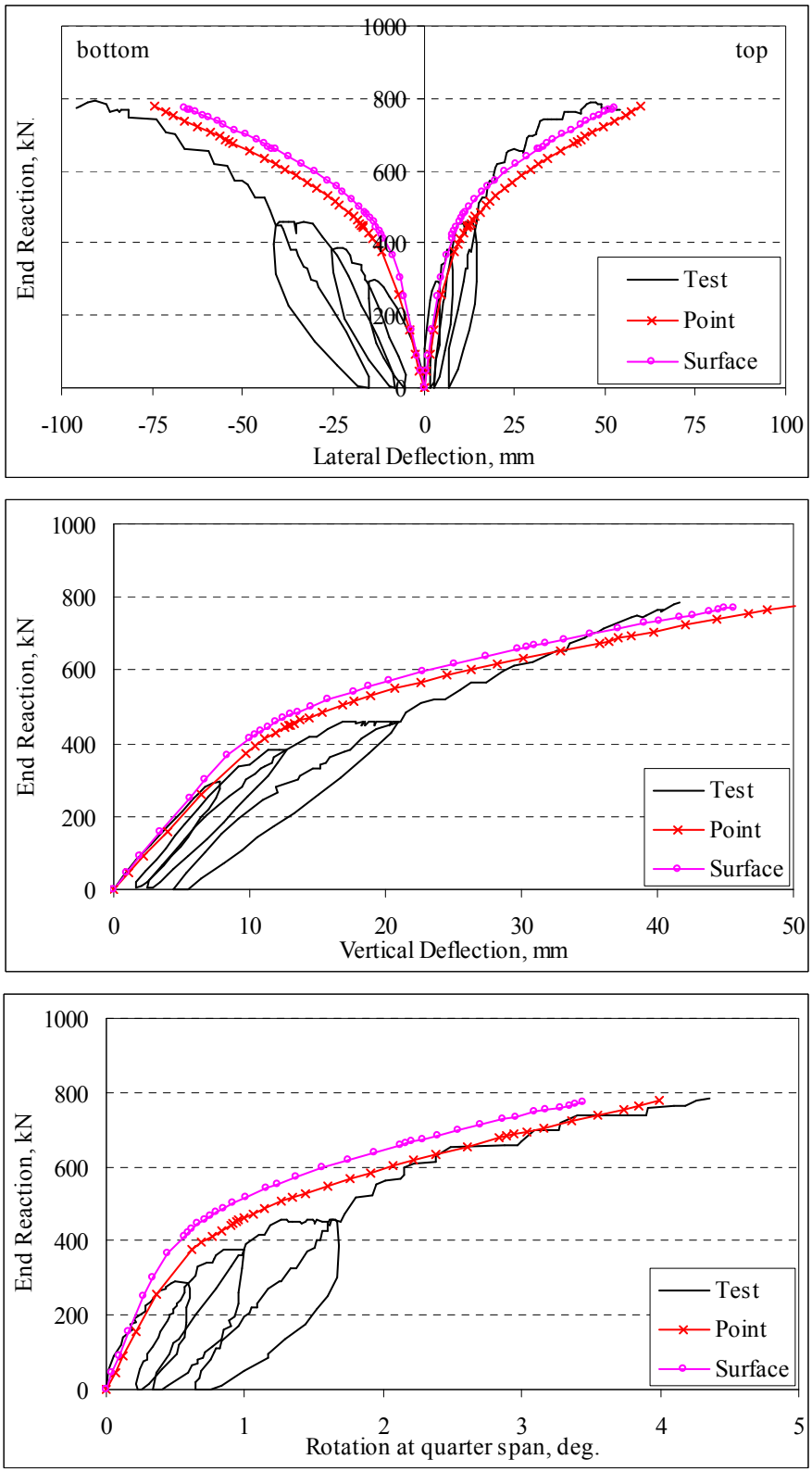

Fig. 4.14. Effect of support representation

4.9.3. Deck-tie springs

Deck-ties are steel plates embedded into the spandrel web, and they connect the double tees to the spandrel beam. As mentioned in Section 4.5, each steel plate was modeled with two spring elements and the axial stiffness value was assumed as 1900 kN/mm (10,875 k/in) per spring. Even though the deck-ties were defined with spring elements throughout the sensitivity analyses discussed above, the spring stiffness of 1900 kN/mm (10,875 k/in) turned out to be relatively large in comparison to the overall stiffness demand of the spandrel. As a result, the spandrel beam behaved as if it was fixed at the locations of the deck-ties, because the spandrel beam twisted around an axis that was located approximately at its mid-height. However, there is a threshold value for the spring stiffness of deck-ties under which the response of the spandrel beam becomes unstable.

Fig. 4.15 shows the results of finite element simulations for different values of deck-tie stiffness. The spring stiffness of 1900 kN/mm (10,875 k/in) produced spandrel behavior as if the connection was fixed. Negligible variations were observed in the response of the spandrel beam when the spring stiffness reduced from 1900 kN/mm (10,875 k/in) to 17.5 kN/mm 100 (k/in). For the spring stiffness of 1.75 kN/mm (10 k/in), even though the top and bottom points at the mid-span of the spandrel beam initially moved outward and twist of the spandrel became dominant for higher load levels, the spandrel beam still showed stable response and reached its ultimate strength. For the spandrel beam considered here, the threshold value of deck-tie spring was approximately 1.75 kN/mm (10 k/in). Fig. 4.15 also shows the response of the spandrel beam for the deck-tie stiffness of 0.175 kN/mm (1 k/in). For that value, once the end reaction reached a critical value of 550 kN (124 kips), the spandrel beam showed laterally unstable response. The beam experienced very large deformations and failed prematurely. The presence of deck-ties is noted here as being crucial to prevent excessive lateral deformations of the spandrel beam and maintain the stability of structure. However, the analysis results showed that the stiffness of deck-tie springs, beyond a minimum threshold value 0.175 kN/mm (1 k/in), had no appreciable influence on the magnitude of vertical deformations at the mid-span.

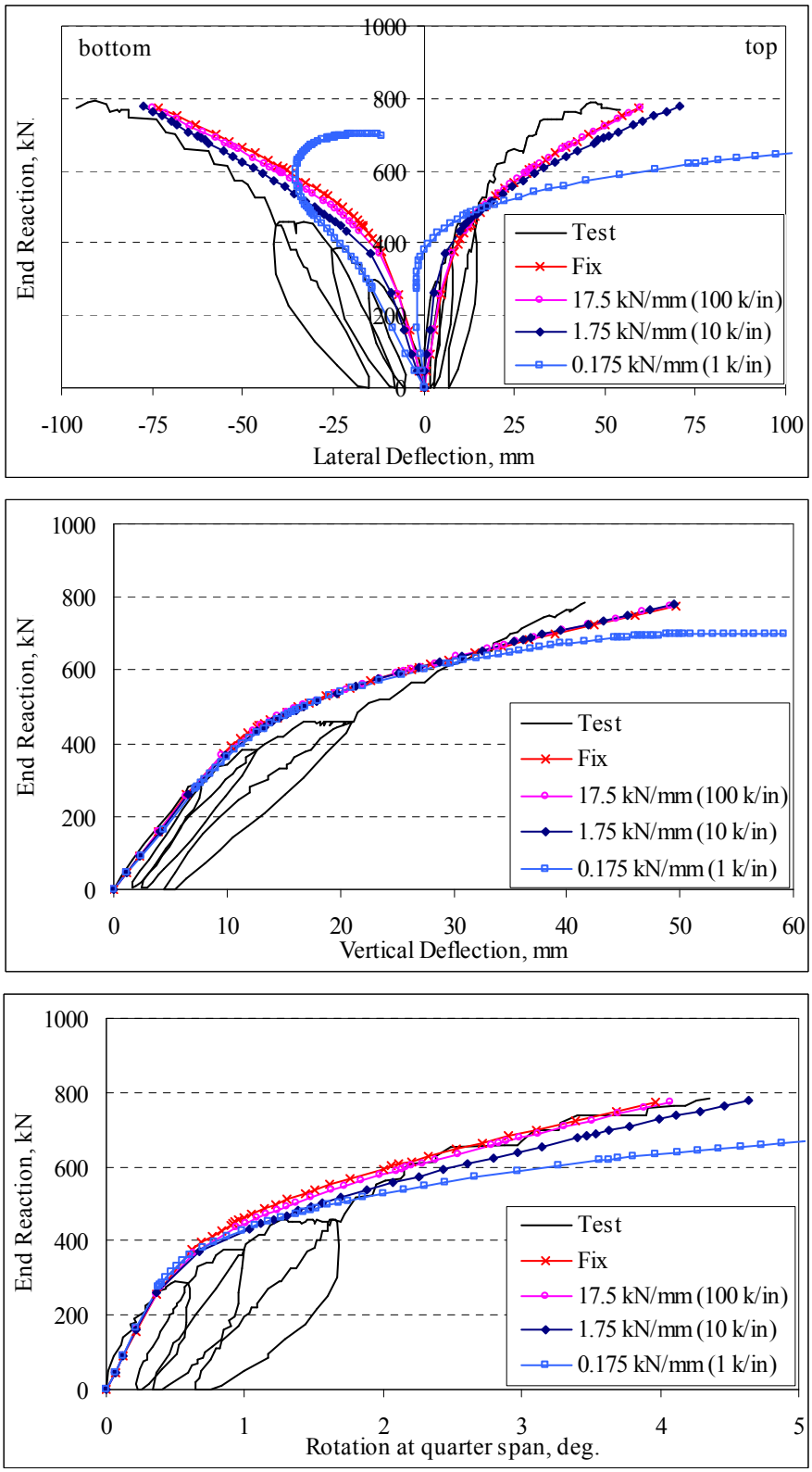

Fig. 4.15. Effect of deck-tie stiffness

4.10. Conclusions

This paper presents the observations and the modeling guidance resulting from the application of finite element analysis techniques in the simulation of the load response of precast prestressed concrete spandrel beams. In particular, the combination of three-dimensional discretization, large deflection theory and advanced material models (concrete damage-plasticity) has been applied to the simulation of full load-displacement response of concrete spandrel beams. These features are not commonly used in the analysis of concrete structures, but they are necessary if one attempts to analytically estimate the ultimate load carrying capacity, as well as the full range of displacement response to loading. Thus, it is believed that knowledge and experience gained from this comprehensive research should provide guidance to those undertaking finite element modeling of concrete structures in order to develop rational analysis tools and design criteria. Prestressed concrete spandrels are subject to very complex load conditions and it is believed that the conclusions reached at the end of the analyses reported here are applicable to a wide range of concrete structures.

The effects of various modeling parameters on the computed response of concrete spandrel beams differ quite significantly, and the following recommendations are offered to enhance the accuracy and reliability of the computational results:

- Element type dramatically influenced the finite element results for lateral deformations due to shear locking of the slender web of the spandrel beam for the weak axis bending. The 8-node brick element with reduced integration is recommended for modeling concrete because of both higher accuracy and computational efficiency. The 8-node element with full integration and the 20-node element with reduced integration exhibit unnaturally stiff response for the lateral deformations due to shear locking.
- The assumption of bearing stress distribution over the spandrel ledge, transferred from double-tees, has a great influence on the lateral displacement at the mid-span and rotation at the quarter-span of the beam. A triangular stress distribution appears appropriate for slender spandrel beams.

- The value of dilation angle defined for the concrete damage-plasticity model drastically changed the spandrel lateral response. With an increase of the dilation angle for concrete, more confinement pressure becomes activated and the spandrel beam model exhibits stiffer response.
- The response of the precast, prestressed concrete spandrel beam is slightly sensitive to the mesh configuration. It is important, however, for the element dimensions to be sufficiently large to include at least one rebar.
- Variations of tension stiffening and fracture energy for concrete had negligible impact on the response of the prestressed concrete spandrel beam although such parameters affect the performance of the numerical algorithm.
- Deck-ties embedded into the spandrel web play an important role on the lateral deformation and rotation responses of the spandrel beam. A threshold value can be defined as the minimum value for the spring stiffness of deck-ties required for the stable response of a spandrel beam. The absence of deck-ties can lead to large lateral deformations and stability problems.
- The axial stiffness of tie-back bolts only changes the initial torsional stiffness of the uncracked spandrel beam. The ultimate load capacity is not affected by the tie-back stiffness.

CHAPTER 5

Comparison of Arc-length and Explicit Dynamic Methods for the Finite Element Static Analysis of Prestressed Concrete Members

5.1. Introduction

This paper compares the arc-length and explicit dynamic solution methods for nonlinear finite element analysis of prestressed concrete members subjected to monotonically increasing loads. The investigations have been conducted using an L-shaped, prestressed concrete spandrel beam, selected from the literature, as a model problem to give an insight into the advantages and disadvantages of these two solution methods. Convergence problems, computation effort, and quality of the results were investigated using the commercial finite element package ABAQUS. We have shown that a static analysis procedure, based on the arc-length method, provides more accurate results if it is able to converge to the solution. However, it experiences convergence problems depending upon the choice of mesh configuration and the selection of concrete post-cracking response parameters. The explicit dynamic solution procedure appears to be more robust than the arc-length method and provides acceptable solutions in cases when the arc-length approach fails, however solution accuracy may be slightly lower and computation effort may be significantly larger. Furthermore, prestressing forces must be introduced into the finite element model in different ways for the explicit dynamic and arc-length solution procedures.

5.2. Background

Even though experimental methods still play a key role in research, numerical methods are increasingly replacing experiments due to their lower cost and time requirements comparing to experiments. Highly nonlinear problems can be solved by using commercially available computer finite element software. Nevertheless, finite element analysis requires the knowledge of how various modeling techniques might affect the numerical results. For example, a three-dimensional finite element simulation of a prestressed concrete beam inherently introduces some numerical and modeling challenges since the model needs to describe the complex material response of concrete,

which includes crushing in compression and cracking in tension.

ABAQUS [53] is a popular finite element program which offers solution techniques for such highly nonlinear problems. ABAQUS/Standard solves a system of nonlinear static equations iteratively to provide the solution of a problem at each load increment whereas ABAQUS/Explicit solves equations of motion by stepping forward in time and using very small increments without solving a system of algebraic equations at each increment [54].

The explicit dynamic solution procedure provided in ABAQUS/Explicit is generally used to solve dynamic problems. However, a static solution can also be obtained by using this procedure provided that the rate of loading is very low to minimize inertial effects in the structure. The analysis of metal forming process is a good example for the application of the explicit solution procedure to static problems [55]. Such analysis method, the so-called quasi-static analysis, is also very useful for solving highly nonlinear problems such as those resulting from stiffness reductions due to concrete cracking, but is unable to trace the descending (unstable) part of the equilibrium path. The arc-length method (or Modified Riks method) [56] and [57], available in ABAQUS/Standard, is used to solve static nonlinear problems. The arc-length method can efficiently capture material and geometric nonlinearity including the unstable post-buckling behavior. However, the peak load, which is often the most important result for engineering purposes, can be determined using both approaches. It is the purpose of this work to evaluate advantages and disadvantages of these two approaches in determining the response of the prestressed concrete members.

Concrete is a strongly nonlinear material and causes many numerical difficulties in finite element analysis. The stress-strain relation of concrete under uniaxial tension features a peak value for the tensile strength followed by a sudden drop with negative stiffness. In uniaxial compression, the stress-strain relation contains a strain hardening branch up to the compressive strength of the concrete and a strain softening regime thereafter. Cracking in tension and crushing in compression are irreversible processes that can be defined as damage. The only concrete model supported by both ABAQUS/Standard and ABAQUS/Explicit is the concrete damage-plasticity model

which incorporates most of the concrete properties such as cracking, strain softening in tension, dilation, damage, compression hardening, stiffness degradation, etc. [55]. These characteristics of concrete constitute the sources of nonlinearity and numerical challenges for finite element analysis. Such challenges have been reported by other researchers [58], [59].

In this work we will illustrate that the arc-length method in ABAQUS/Standard experiences convergence problems in solution for some combinations of concrete material properties and mesh configurations. The explicit dynamic method in ABAQUS/Explicit overcomes such numerical problems in the solution due to stabilizing effects of inertia. However, the time increment used in the explicit method has to be very small and the time of load application must be sufficiently low. Thus, the overall computation effort of explicit dynamic procedure can be quite significant. Furthermore, prestressing forces cannot be treated in the same manner with arc-length and explicit dynamic methods. In the explicit dynamic method, prestressing forces must also be introduced to the system slowly to prevent dynamic effects which creates the need for an additional quasi-static analysis before application of the load.

The fundamental advantages and disadvantages of the arc-length and explicit dynamic analysis are well known [60], [61]. But the manner in which they are manifested in the analysis of nonlinear problems typical for prestressed concrete structures does not appear to be documented. In particular, even though nonlinear finite element analysis of prestressed concrete members has been reported by many researchers [62], [63], [64], and [65], we have found no information in the literature that would advocate use of one method over the other in the analysis of prestressed concrete structures. Thus, in this study, the arc-length and explicit dynamic solution procedures were compared for the nonlinear finite element analysis of prestressed concrete members under monotonically increasing loads in order to evaluate the efficiency of these methods. By efficiency we understand here not only computational effort but also quality of the results obtained which we assess by comparing with available experimental results. To this end, a three-dimensional finite element model of an L-shaped, prestressed concrete spandrel beam was generated and analyzed with arc-length and explicit dynamic solution procedures in

order to give a better understanding of the overall advantages and disadvantages of these procedures.

5.3. General aspects of 3D finite element modeling of prestressed concrete members

In three-dimensional applications of finite element analysis, concrete is usually modeled using eight-node brick elements with reduced integrations. The element library of ABAQUS/Explicit for brick elements is confined to eight-node brick elements with reduced integrations whereas ABAQUS/Standard supports both eight- and twenty-node elements. Conventional reinforcement is represented by truss elements, which carry axial load only. Therefore, a uniaxial stress-strain relationship such as the elastic-plastic material idealization is sufficient to define the behavior of reinforcement. Using the embedded element option in ABAQUS, an assembly of reinforcement (i.e., embedded element) is located in the concrete solid (i.e., host element). In this case, translational degrees of freedom at a node of a reinforcing bar are constrained by the corresponding degrees of freedom in the concrete solid. This approach assumes that there is perfect bonding between rebar and concrete interfaces. However, this method neglects the load transfer in the cracked concrete element around the rebar. The behavior of cracked, reinforced concrete element is generally represented by introducing an additional ductility to the post-peak branch of concrete model in tension, the so-called "tension stiffening" effect.

Prestressing strands are also modeled using truss elements embedded in the concrete solid and perfect bond between concrete/strand interfaces. A proper model for the transfer length of strands becomes essential in the analysis of prestressed concrete beams, otherwise the beam fails in the end regions where the stress level in the concrete can be very high, depending upon the transfer of prestress force. The simplest modeling approach is to divide the transfer length of a strand into a number of segments and gradually decrease the cross sectional area of each segment to the beam ends [66]. When the prestressing force is defined as a constant initial stress along a strand, a strand

segment with reduced cross sectional area will be subjected to lower prestressing force and hence lower stresses are transferred to the concrete.

5.4. Arc-length method

The arc-length method is a static solution procedure that allows evaluation of the load-deflection path for a nonlinear structural response including descending branches. The method can efficiently account for material and geometric nonlinearity. Unlike the force-control approach, in which the magnitude of the load is specified, or the displacement control approach, in which the magnitude of a selected displacement is specified and the corresponding load magnitude computed, the arc-length method does not require specification of either. Instead, as seen in Fig. 5.1, the advancement from point *(n-1)* to point *(n)* on the equilibrium path (specified by unknown values of the displacement and force) is achieved by the definition of the distance l_n between these two points. To this end, in addition to the governing equation, a constraint equation, specifying l_n, is necessary for the solution of the simultaneous equations governing the problem in which the magnitude of the load is an additional unknown.

The constraint equation describes the arc length, l_n, of the load-displacement path. The load magnitude P_{total} at the new point on the equilibrium path is defined as:

$$P_{total} = \lambda P_{ref} \tag{5.1}$$

where P_{ref} is the reference load vector and λ is the load proportionality factor, which is an unknown representing the load. Nonlinear equilibrium equations are solved together with the constraint equation using Newton's method defining one arc-length step. The result is the nodal displacement vector and the load proportionality factor, λ.

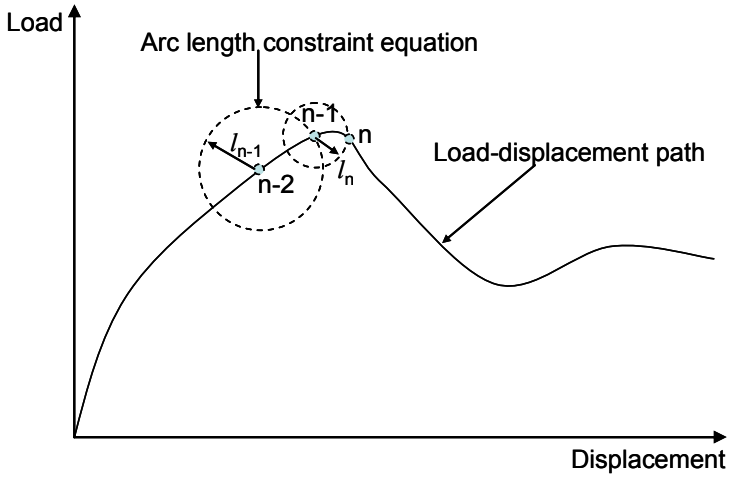

Fig. 5.1. Arc-length procedure

5.5. Explicit dynamic method

The static response of a prestressed concrete beam can also be investigated by using the explicit dynamic procedure. Since we are interested in the static solution of the problem, inertial effects produced by the structural mass should be minimized in explicit dynamic analysis. By either increasing the mass density of concrete or decreasing loading rate, the oscillation of the beam can be limited and inertial forces made negligible (Fig. 5.2). In practice, if the loading time T over which the load is increased to its final value, is of the order of an integer number of periods of the lowest frequency vibration, the inertial effect is usually negligible. The figure also illustrates that dynamic response initiates when the load reaches a local maximum in the static equilibrium path. So, even though the descending part of that path cannot be traced when using dynamic explicit analysis, one can still determine the peak load.

The time increment, Δt, used in the explicit dynamic analysis is automatically determined by the numerical stability limit of the explicit method implementation used in ABAQUS. There is a close relationship between the stability limit and the time required for a stress wave to cross the smallest element dimension in the model. When the model consists of elements with very small dimensions, a small time increment has to be used

and total computation effort will increase, given a fixed loading time, T. The number of increments, m, required to complete the analysis is $m=T/\Delta t$. Computational effort for the explicit dynamic analysis is proportional to the product of the number of time increments, m, and the total number of degrees of freedom.

An optimum value for the loading time, T, can be easily found if the longest period of natural vibration, T_n, is known (or estimated). As a starting point, the explicit dynamic analysis has been performed here for a loading time, T, which is a value in the range of ten to fifty times larger than that period of the lowest frequency of vibration, T_n (i.e., $T=10T_n$ *to* $50T_n$) [54]. For such a loading time, inertial effects are generally negligible, but computation effort might be high. In the subsequent analyses, the loading time has been gradually reduced until a significant variation due to inertia is observed in the analysis results. The magnitude of inertial forces can be evaluated by monitoring the ratio of kinetic energy to total strain energy during the analysis. That ratio should be less than 0.5 percent if the quasi-static response is desired [67].

Furthermore, the natural period does not remain constant during the analysis and increases when the structural stiffness reduces due to concrete cracking or steel yielding. Therefore, the loading time initially determined based on the fundamental period of the elastic structure is likely to be inadequate to ensure that inertial effects are minimized.

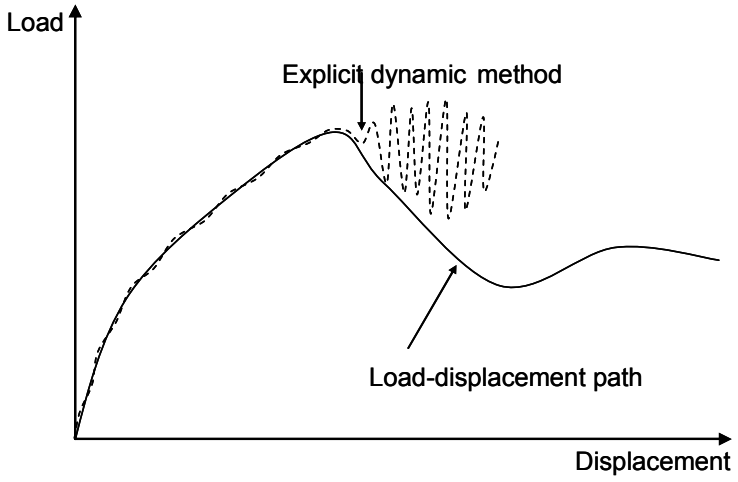

Fig. 5.2. Explicit dynamic procedure

5.6. Modeling of prestressing force

Concrete cracking reduces both torsional and flexural stiffness of prestressed concrete beam and causes significant increase in deflections. However, prestressing forces delay cracking under flexure. Therefore, prestressing strands should be modeled properly in order to capture concrete cracking at the appropriate load level, as well as the corresponding deflection of the beam with sufficient accuracy. A significant modeling aspect of prestressed concrete beams is to appropriately create the initial stress state due to prestressing at the beginning of the analysis. Using the arc-length method in ABAQUS/Standard, the prestressing force in a strand can be defined as an initial stress that is assumed to be constant along the truss element of the strand in the model. Then, in the first increment of the arc-length analysis, the structure will reach the equilibrium state for this initial stress condition. If the same modeling approach for prestressing forces is applied in the explicit dynamic procedure, the initial stress state creates an impact loading in the beam and the transient response includes oscillations with amplitudes that can be large. Therefore, prestressing forces in the explicit dynamic analysis must be modeled in an alternate manner, utilizing either a direct or an indirect procedure.

In the direct modeling approach, the geometry and material states of the beam, when subjected to prestressing effects only, are obtained using the static analysis procedure in ABAQUS/Standard and transferred to ABAQUS/Explicit as an initial condition. Since the beam is already in equilibrium at the end of the static analysis, the initial condition defined at the beginning of the explicit dynamic analysis does not lead to impact loading. However, ABAQUS/Standard and ABAQUS/Explicit process data in different ways and the forces transferred from ABAQUS/Standard may not be in perfect equilibrium in ABAQUS/Explicit, which causes minor oscillation of the beam. These oscillations, however, will become negligible in the rest of the explicit analysis.

In the indirect modeling approach, the prestressing force in a strand is introduced via an artificial reduction in strand temperature. Without transferring any data from ABAQUS/Standard to ABAQUS/Explicit, the response of prestressed concrete beam is evaluated with two consecutive explicit analyses. In the initial analysis, temperature change is slowly applied to the prestressing strands to generate the intended prestressing

effect, after which the temperature remains constant. It should be noted that temperature change does not affect the physical properties of concrete or steel in ABAQUS, and it is used solely as a way to create the desired initial stresses in the strands. The required temperature change, ΔT_{st}, can be obtained using equation (5.2), in which α_{st} represents the thermal expansion of the strand, E_{st} is the elastic modulus of strands and f_{pe} is effective prestress after losses.

$$\alpha_{st} . \Delta T_{st} = f_{pe} / E_{st} \tag{5.2}$$

5.7. Modeling of concrete

Concrete is an inhomogeneous material and exhibits properties that vary broadly from one experiment to another. The stress-strain relation of concrete in compression has a nonlinear ascending branch up to ultimate strength, followed by a strain softening region. Concrete in tension, however, cracks at very low stress levels. The behavior of concrete under multi-axial stress states is even more complex. Consequently, defining a material model for concrete that represents its response with a high level of fidelity is a very challenging task, [68],and [69]. The concrete damage plasticity model was implemented in this study for both the arc-length and the explicit dynamic analyses because it is the only concrete model offered in both ABAQUS/Standard and ABAQUS/Explicit. In a previous study [70], this model was shown to offer the flexibility needed to represent various property of concrete. The concrete damage-plasticity model in ABAQUS relies on the ideas proposed by Lubliner et al. [71] and by Lee and Fenves, [72] and [73]. The concrete damage-plasticity model brings together isotropic damage elasticity and nonassociated multi-hardening plasticity. The concrete damage-plasticity model assumes two failure modes; cracking in tension and crushing in compression and isotropic damage elasticity represents the elastic stiffness degradation of concrete due to cracking.

In general, the resistance of cracked concrete is often ignored in design for simplicity. However, neglecting the post-cracking behavior of concrete may lead to significant error in the nonlinear finite element analysis of prestressed concrete structures. The post-cracking response of concrete plays an important role in deflections, crack width, bond-

slip, and shear transfer, etc. [74]. Cracking initiates once the stress level at an integration point in a concrete brick element reaches the concrete tensile strength, cracking initiates. Cracking introduces gradual strength decrease at this integration point in accordance with the post-peak response of concrete model in tension. However, the cracked reinforced concrete element can still transfer load through the rebar. Interaction between cracked concrete and rebar such as stress transfer, bond-slip, etc., is not directly taken into account with the reinforcement modeling approach mentioned above. This interaction effect, the so-called "tension stiffening" behavior, is approximated in the concrete model by modifying the tension softening region relative to that for plain concrete as seen in Fig. 5.3, [75].

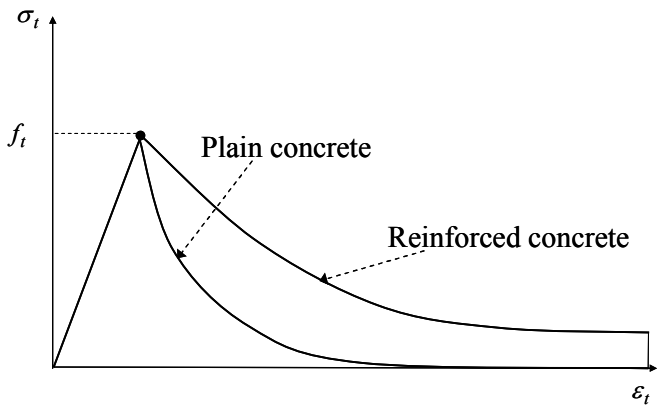

Fig. 5.3. Tension stiffening of concrete due to concrete-rebar interaction

Defining proper tension stiffening behavior plays an essential role in the quality of the results and the performance of the algorithm used. Numerical solution of a model generated with ABAQUS/Standard might be unstable if a relatively small amount of tension stiffening effect is introduced into the concrete model. It is commonly suggested that numerical stability can be achieved for the solution of an arc-length analysis when the ultimate tensile strain of concrete, including the effect of tension stiffening, is equal to a value ten times larger than that of plain concrete [54]. However, due to stabilizing effect of inertia, the explicit dynamic procedure does not experience numerical instability even if the post-cracking response of plain concrete is used in the concrete model and tension stiffening effect is ignored.

Tension stiffening can be introduced as the fracture energy used in the cracking criterion. The fracture energy, G_f, is a material property indicating the energy required to open a unit area of crack in a plain concrete specimen, [76] and [77]. The interaction between concrete and steel is generally taken into account by using a fracture energy value for reinforced concrete, which is larger than that for plain concrete. The total cracking displacement, w_t, can be found using equation (5.3) where f_t is the tensile strength of concrete.

$$w_t = \frac{2G_f}{f_t} \tag{5.3}$$

5.8. Modeling an L-shaped, precast, prestressed concrete spandrel beam

We use a finite element model for an L-shaped, precast, prestressed concrete spandrel beam, which was investigated experimentally [78], to get better understanding of the relative merits of two approaches: the arc-length method and explicit dynamic solution procedure. Such beams were suited for this study since they exhibit a complex structural response to loading and thus constitute a good test for various aspects of the model. There is also a practical reason for this choice: spandrel beams have been widely used in the perimeter of precast concrete frames. They support deck beams and are connected to column corbels at their ends. The cross section of an L-shaped spandrel beam is under the combined effects of shear, torsion and bending. The vertical loads acting on the beam ledge create biaxial bending due to the asymmetric shape of the cross section. The eccentricity of the vertical loads also causes a torsional effect, which leads to twisting of the member. Prestressing forces further complicate the behavior of a spandrel beam.

5.8.1. Description of the experiment

An L-shaped, prestressed spandrel was tested at North Carolina State University and the results of this test were reported by Lucier et al. [78]. The behavior of L-shaped spandrel specimen was also modeled by using Anatech Concrete Analysis Program [66]. The specimen had a length of 13.7 m (45 ft), a depth of 1.5 m (5 ft) and a web thickness

of 0.2 m (8 in). The cross section of each spandrel ledge was 0.2 × 0.2 m (8 × 8 in). The ledge was terminated at a 0.3 m (12 in) distance from both ends of the spandrel web (Fig. 5.4). Low relaxation, 1860 MPa (270 ksi), 12.7 mm (½ in) diameter seven-wire steel strands with initial prestressing forces of 100 kN (Type A) and 68.5 kN (Type B) were used in this specimen (Fig. 5.5). The cylinder strength for concrete in compression was measured as 49.6 MPa (7,190 psi). A 152 × 152 mm (6 × 6 in) - W4 × W4 mesh of welded wire fabric was placed on both sides of the spandrel web. Reinforcement details can be found in Lucier et al. [78].

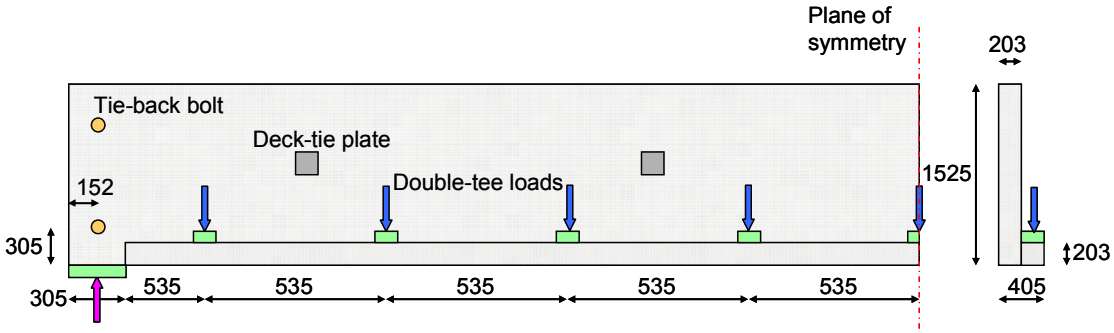

Fig. 5.4. Specimen dimensions (mm)

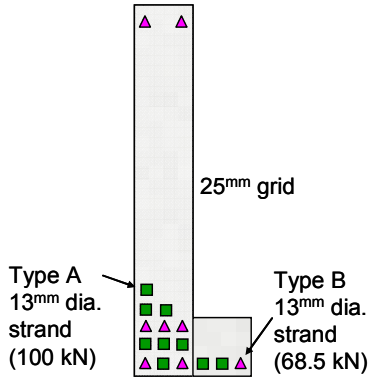

Fig. 5.5. Prestressing strand details

The web of the spandrel beam was laterally connected to the vertical support at the ends with 25.4 mm (1 in) diameter bolts. The lateral tie-back bolts were located 0.15 m (6 in) away from the ends and 0.3 m (12 in) away from the top and bottom. Teflon-coated bearing pads were provided to reduce friction at the end supports, and these pads

enabled the test spandrels to undergo a significant out-of-plane deflection and hence the most severe loading case was obtained. The spandrel web was connected to the double-tee deck by means of embedded steel plates.

The self-weight of the spandrel specimen with testing equipment resulted in a vertical reaction of 22 kips at the bearing support. Hydraulic jacks were attached to 3 m wide (10 ft) double tees, resting on the spandrel ledge. Before testing, three load levels, service (DL+LL), service with snow (DL+LL+S) and fully factored (1.2DL+1.6LL+0.5S), were determined for the spandrel supporting an 18.3-m (60-ft) span double-tee. The load was applied until each of these load levels and then released. Finally, the spandrel was loaded up to failure. During the experiment, the vertical and lateral displacements at the top and bottom of the spandrel mid-span, and the rotation of the spandrel quarter-span and the vertical reaction at the bearing support were also monitored.

5.8.2. Description of the finite element model

The specimen described in the preceding section was chosen in the present numerical investigation due to availability of the experimental results, as well as its complex nonlinear response which is challenging from the computational standpoint. Due to the symmetry of the specimen with respect to the mid-span, only one-half of the spandrel was modeled. The end of spandrel beam was fixed at the mid-point of the bottom surface of the web against vertical displacements at the bearing pad. However, since restraining only one point in such a three-dimensional finite element model may lead to singularity problems, the bottom surface 0.3 × 0.2 m (12 × 8 in) of the web at the support region was forced to remain plane during analysis by defining planar constraint equations. This eliminates singularity and bypasses a need for much more complex contact analysis. The tie-back spring stiffness was assumed to be equal to 100 kN/mm (570 k/in) after computing the axial stiffness for one-meter long bolt with a diameter of 25 mm (1 in). Deck ties comprising steel plates with 76 × 152 × 9.5 mm (3 × 6 × 3/8 in) dimensions were used in the experiments to reduce lateral displacement at the mid-height of the spandrel. These ties were modeled by two spring elements located at the mid-height of the front face of the spandrel. To accommodate the finite size of the connections, each

deck-tie was modeled using two adjacent springs with an axial stiffness of 1910 kN/mm (10,900 k/in), each corresponding to one half of the steel plate stiffness value.

The concrete was modeled using 8-node brick elements with reduced integration and hourglass control. The concrete solid was analyzed with three different mesh configurations defined as coarse, intermediate and fine with the maximum element size of 203 mm, 102 mm and 51 mm (8 in, 4 in and 2 in) respectively. The elastic modulus of concrete can be estimated as 33 GPa (4,800 psi) according to the ACI Committee 318 building code document, [79], for a concrete compressive strength of 49.6 MPa (7,190 psi). The uniaxial stress-strain relation of the concrete under compression was assumed as in Fig. 5.6. Post-peak behavior of concrete in tension was described by means of a concrete fracture energy of 1.75 kN/m (0.01 k/in) and a tensile strength of 3.5 MPa (0.509 ksi).

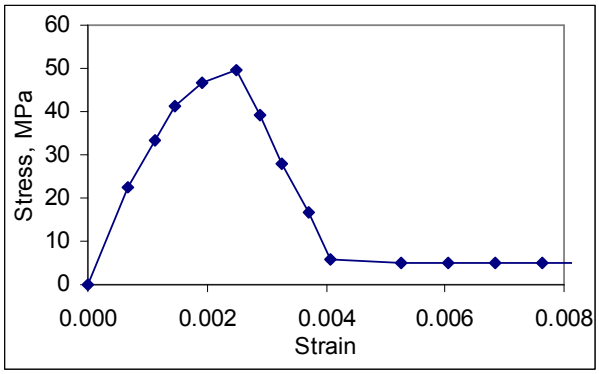

Fig. 5.6. Uniaxial stress-strain relation for plain concrete in compression

Two-node linear 3D truss elements were used to model both non-prestressed reinforcement and prestressing strands. Typical element size for reinforcement, welded wire mesh and strands was 50 mm (2 in). The material model for all steel elements was based on elastic-perfectly plastic behavior. The elastic modulus was assumed to be 200 GPa (29000 ksi). The yield strengths for mild steel, welded-wire-mesh reinforcement and prestressing strands were taken as 445 MPa (64.5 ksi), 675 MPa (98 ksi) and 1675 MPa (243 ksi), respectively. The transfer length was assumed to be equal to 510 mm (20 in) and a 15% loss in prestressing force was assumed [66].

Prior to arc-length analysis, the spandrel beam model was first analyzed with load-

controlled static procedure for self-weight and prestressing forces. Stresses in stands after losses were introduced as an initial stress state and the self-weight of the spandrel was defined with body forces so that the resulting spandrel end reaction was 100 kN (22 kips). Response to subsequent load transferred by the double-tees was analyzed using arc-length approach. This load was distributed linearly over the bearing pads (starting with zero at the connection of the spandrel ledge and the web). The assumption on bearing stress distribution was made considering the potential for relative movement of the spandrel ledge with respect to double tees. The initial arc length increment was taken quite large, 0.01 out of a total arc length of 1.0, since severe nonlinearity was not expected in the solution for low load levels. This allowed for a faster advancement along the equilibrium path at early stages of loading. The subsequent arc length increments were automatically determined by ABAQUS, based on the number of iterations needed to converge.

In the explicit dynamic approach, prestressing was introduced by defining an artificial temperature change in strands. The temperature change was different for different strands to achieve varying prestressing force. The strands of Type A had prestressing force of 85 kN after losses while Type B strands had 58.3 kN. Following the prestressing stage, explicit dynamic analysis was continued to analyze the response due to load transferred by the double-tees. The bearing stress distribution was assumed as in the case of the arc-length approach.

5.8.3. Duration of the explicit analysis

A frequency analysis was performed to determine the largest period of vibration, T_n. For the spandrel beam considered here, the fundamental period of 0.075 sec was found. Thus, a loading time between 0.75 sec and 3.75 sec (i.e., $T=10T_n$ and $50T_n$) should be used to minimize dynamic effects in the spandrel response.

The vertical end reactions versus the lateral deflections at the top and bottom of the mid-span were plotted in Fig. 5.7 for the loading times of 1 sec, 0.5 sec and 0.25 sec for the intermediate mesh. The displacements toward the inner face of the spandrel (the face that is connected to the double-tee beams) were assumed positive. Therefore, the top of

the spandrel web moved inward at the mid-span. The self-weight of the specimen (100 kN) were excluded and hence the end reactions begin with zero value as shown in the figure.

The results in Fig. 5.7 showed that when the end reaction reached the value of approximately 400 kN (90 kips), concrete cracking occurred. The results in the elastic region (i.e., end reaction < 400 kN) were the same for all loading times. Moreover, loading times of 0.5 sec and 1 sec yielded a similar response in the inelastic regions. Except that for the loading time of 0.25 sec, the spandrel model exhibited stiffer response in the inelastic region which can be attributed to dynamic effects. After concrete cracking, the stiffness of the spandrel decreased and the natural period of vibration increased. Thus, the minimum loading time leading to the quasi-static response also increased and the loading time of 0.25 sec became inadequate to prevent dynamic effects in the inelastic region.

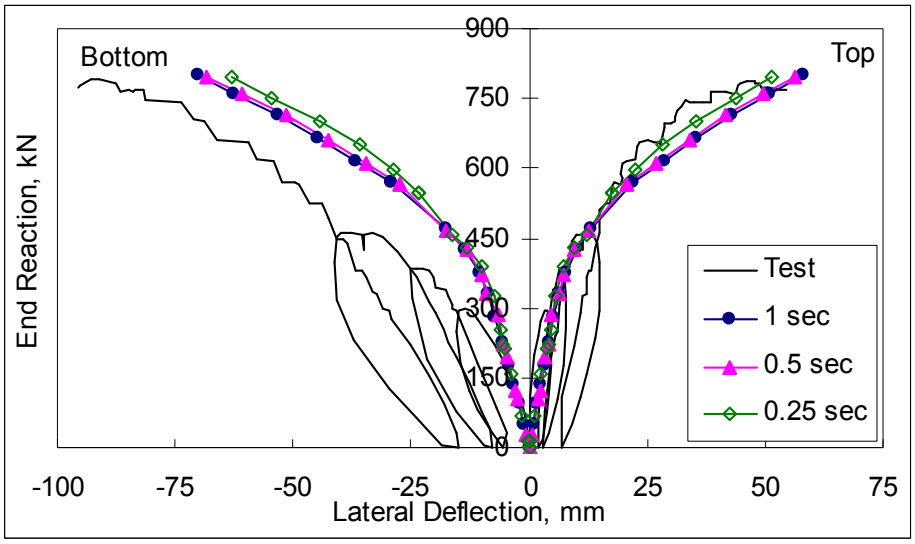

Fig. 5.7. The sensitivity of the explicit dynamic analysis to the loading time

The effects of loading time variation on the vertical deflections at the mid-span were less pronounced than on the lateral deflections. It is attributed to the fact that the spandrel examined here is quite slender and much more flexible in the lateral direction than vertical.

Another way to evaluate the magnitude of dynamic effects is to find the maximum

ratio of kinetic energy to strain energy of the entire model. Fig. 5.8 shows the ratio of the kinetic energy to the strain energy for the spandrel as a function of time for different loading times and mesh configurations. For the loading time of 0.25 sec, the maximum energy ratio was greater than the limit of 0.5 percent, which supports the finding, discussed earlier, that the dynamic effects were significant in this case. The loading time of 0.5 sec for which the maximum energy ratio was around 0.5 percent was the minimum value to ensure negligible dynamic effects.

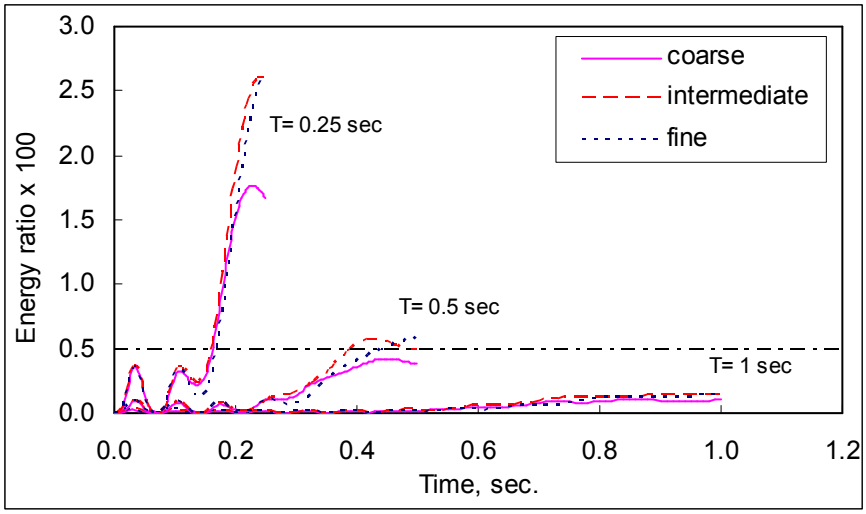

Fig. 5.8. Energy ratios for various loading times and mesh configurations

5.9. Comparison of the solution procedures for the spandrel beam example

5.9.1. Robustness

The results of arc-length and explicit dynamic analyses of the spandrel beam with the fine mesh were plotted for the lateral displacements at the mid-span versus the vertical end reactions in Fig. 5.9. A loading time of 1 sec was used to minimize the dynamic effects noted the preceding section for explicit dynamic analysis. The arc-length analysis showed a severely nonlinear zone around the region where the tie-back springs were located. The horizontal reaction force in the spring can be large and the element in the

concrete solid, associated with this reaction force, experienced large inelastic deformations. Thus, the arc-length method failed to converge to the solution for the fine mesh (Fig. 5.9). It should be noted that such localized inelastic strain had not been observed for the arc-length analyses with coarse and intermediate meshes as the tie-back forces were distributed over a larger volume. As seen in Fig. 5.9, the explicit procedure overcomes the problem in the fine mesh observed for the arc-length method. Large inelastic deformation still appeared around the tie-back springs, but they had a negligible effect on spandrel response and they could be handled effectively by the explicit algorithm.

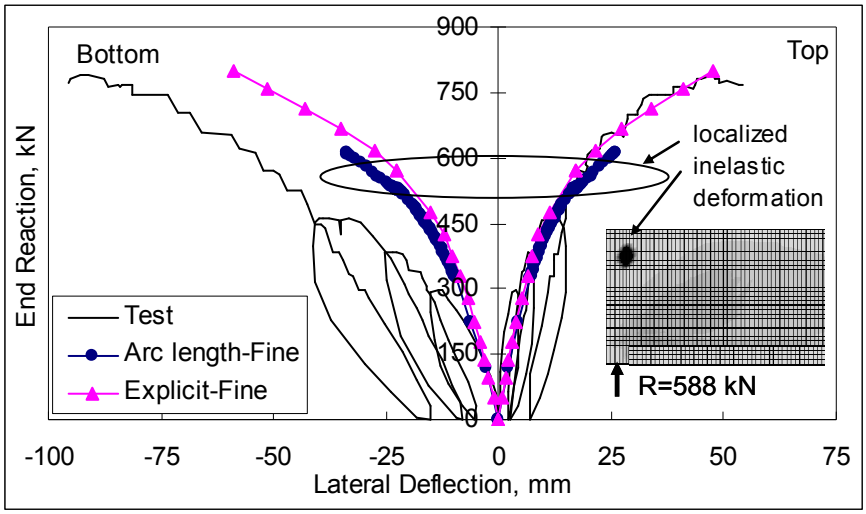

Fig. 5.9. Comparison for the mesh refinement

In addition to the case of the fine mesh, the arc-length method cannot converge to the solution when the concrete model in the post-cracking regime includes a relatively small amount of tension stiffening. The results of the explicit dynamic and the arc-length analyses were compared for the intermediate mesh with and without the tension stiffening (Fig. 5.10). Both the arc-length and the explicit dynamic methods provided numerical solutions when the tension stiffening effect was introduced in the concrete model. However, the arc-length analysis without the effect of tension stiffening could not converge to the solution and failed right after concrete cracking initiated in the spandrel while the explicit dynamic procedure continued without interruption.

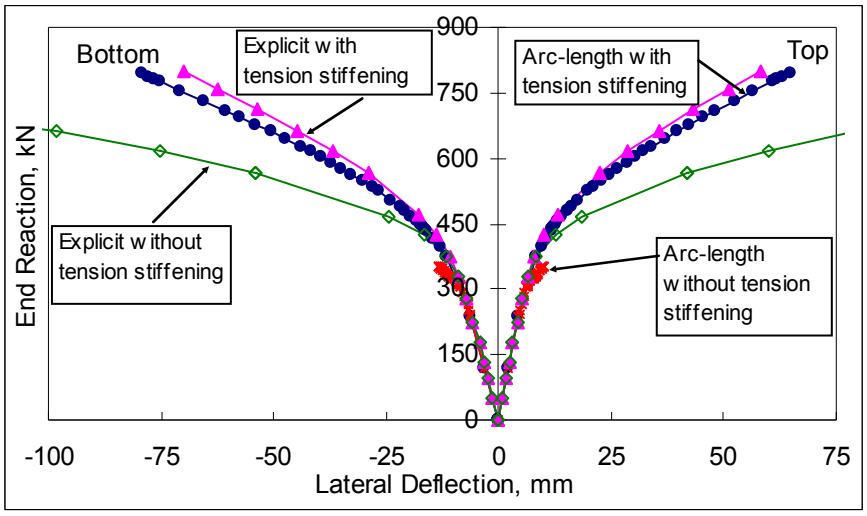

Fig. 5.10. Comparison for the effect of tension stiffening

As mentioned above, the tension stiffening effect for the concrete is closely related to the amount of steel distributed along the member. Therefore, it is not appropriate to ignore the tension stiffening for the spandrel beam since the steel ratio for a typical prestressed concrete spandrel beam is relatively high and tension stiffening must exist. However, this effect posses problems for the analysis of lightly reinforced concrete beams.

In the analyses shown in Fig. 5.10, the effect of tension stiffening was introduced in the concrete model by increasing the fracture energy of plain concrete. Fig. 5.11 shows the stress-strain relationships for concrete in tension based on different values for the fracture energy. The fracture energy of 1.750 N/mm represents the case with tension stiffening and the value of 0.175 k/in is used to represent the case with virtually no tension stiffening, or the case of plain concrete. The strain softening region of the plain concrete is steeper than that for reinforced concrete, which makes it harder for the arc-length method to achieve convergence in the former.

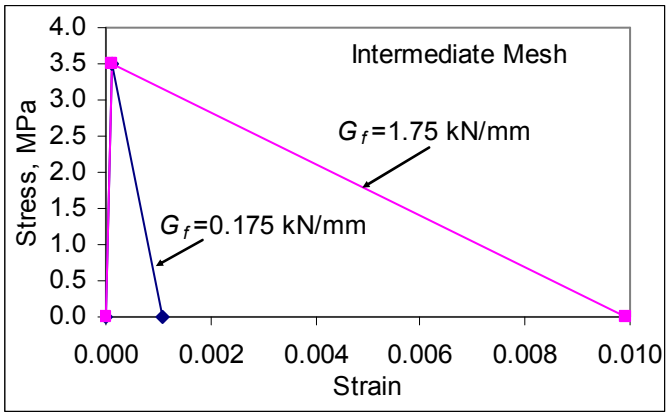

Fig. 5.11. Stress-strain relationships for concrete in tension

5.9.2. Computational accuracy

In the preceding section, we compared the ability of the arc-length and explicit dynamic methods to provide a solution and documented that the explicit dynamic method yielded a solution while the arc-length method failed in the analysis of concrete structures modeled with a small amount of tension stiffening or a refined mesh. The small discrepancies in load-deflection behavior present in cases that were successfully solved by both approaches stems from several reasons. First, when solving a static problem, the explicit procedure inherently introduces computational error since the static equations of equilibrium are not exactly satisfied. Second, to advance the solution in time, numerical time integration is performed and this is associated with an additional error. Third, for the arc-length method, the static equations of equilibrium are also satisfied within a prescribed tolerance, and the resulting errors may be of opposite sign than those in the explicit dynamic approach.

Fig. 5.12 compares the results of two solution methods with the test result of the spandrel specimen for rotations at the quarter span. Explicit dynamic analyses were performed for a loading time of 1 sec. The arc-length tends to give closer results to the test measurements than the explicit dynamic method for the spandrel example considered here. The results of the explicit dynamic analysis were more sensitive to the mesh refinement than those of the arc-length method. While mesh refinement from coarse mesh to intermediate mesh configuration had a minor effect in the results of the arc-

length analysis, the explicit procedure provided the results in better agreement with the test results for the intermediate mesh. However, from the practical viewpoint, one can say that all of the simulations in Fig. 5.12 were acceptable.

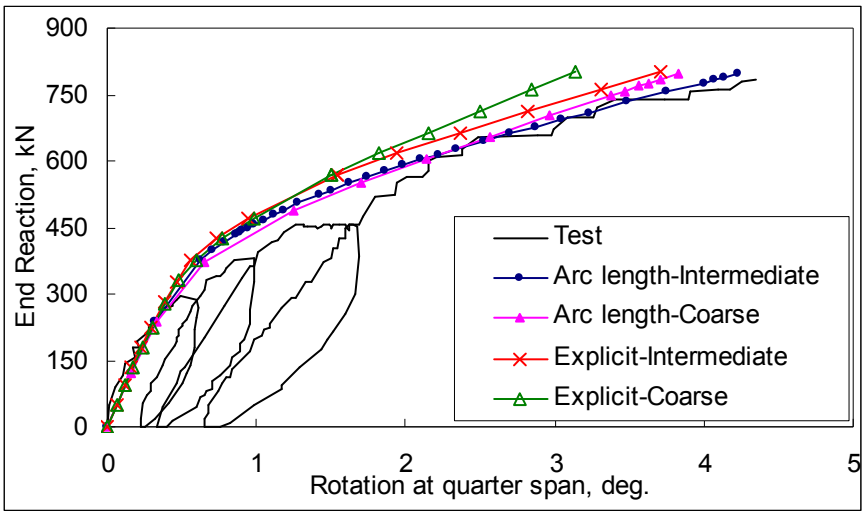

Fig. 5.12. Comparison for the rotations at the quarter span

5.9.3. Computational effort

To obtain an insight about how the computation effort changes with respect to the solution procedure and the size of the problem, CPU time required for the analysis of the spandrel model was studied. CPU time for the explicit analysis, using loading times of 2, 1, and 0.5 sec, was compared with that of the arc-length analysis for coarse and intermediate meshes (Fig. 5.13). Since the arc-length procedure did not converge to the solution for the fine mesh, there was no basis for comparison with the explicit method. It should be noted that these results were obtained by excluding CPU time spent for the initial analysis of prestressing and self weight load. The highlighted columns in Fig. 5.13 indicate the minimum loading times, ensuring negligible dynamic effects, for explicit dynamic analyses. The results show that the arc-length procedure used less CPU time than the explicit method for both mesh configurations. However, when the number of solid elements increased approximately threefold by changing the mesh configuration from coarse to intermediate, the CPU time increased for the arc-length procedure whereas the CPU time decreased for the explicit procedure using the minimum loading time.

Thus, it may be concluded that the explicit dynamic procedure can be more efficient than the arc-length method in some cases. This reduction was made possible by use of a smaller loading time for the intermediate mesh than for the coarse mesh and still ensure negligible dynamic effects.

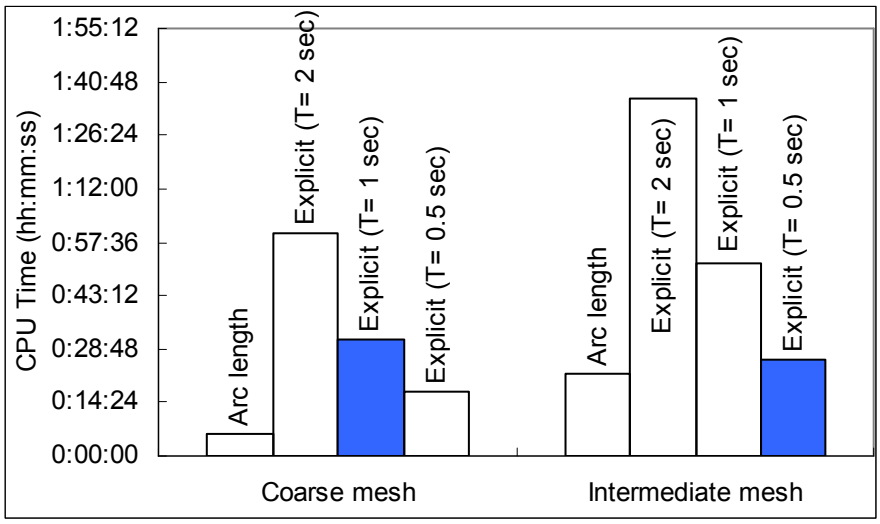

Fig. 5.13. Comparison for CPU time

5.10. Conclusions

In this study, the arc-length and the explicit dynamic finite element approaches were compared for three-dimensional, non-linear finite element analysis of prestressed concrete beams under monotonically and quasistatically increasing loads. The advantages and disadvantages of using these two methods were investigated in the context of strongly nonlinear structural response. It included the damage-plasticity model for concrete, resulting from concrete crushing in compression and low strength in tension, as well as from a combination of structural response modes formulated within a large–strain theory. All those features are present in the analysis of L-shaped, prestressed concrete spandrel beam, which has been used as a model problem in this work. The findings are as follows:

The most significant finding is that when the effect of tension stiffening for concrete is small, the arc-length approach fails while the explicit method still yielded a solution.

Thus, in the analysis of lightly reinforced concrete structures, for which the tension stiffening for concrete is expected to be small, the arc-length method is likely to fail converge to a solution. When both methods yield solutions, those solutions are close to each other provided that prior to the explicit dynamic analysis of a static problem, the loading time over which the load is increased to its final value is determined so as to make the dynamic effects negligible.

The explicit method requires somewhat more computational effort than the arc-length method. However, as indicated above, it is less sensitive to various model parameters and, consequently, more robust. The computational cost of the explicit method can be minimized by careful selection of the loading time over which the load is increased to its final value. In conclusion, a loading time (T) equal to fifty times the fundamental period (T_n) of a concrete structure is probably too long even assuming that when the stiffness of the structure decreases due to concrete cracking, the fundamental period of the structure increases and hence the influence of dynamic effects increases as well. However, since the spread of inelastic zones is somewhat different for different mesh configurations, the minimum loading time ensuring negligible dynamic effects depends to some extent on the mesh, even though the fundamental period of a linear-elastic structural model is virtually independent of the mesh configuration. The present investigation indicates that a loading time (T) equal about 10-15 times the fundamental period (T_n) is adequate.

Even for the coarse mesh, the results of the arc-length method are in good agreement with the experimental results. However, a finer mesh should be used for the explicit dynamic method in order to obtain results that are close to experimental measurements.

Based on these findings, it may be concluded that from the viewpoint of computational efficiency, the arc-length method should be preferred over the explicit dynamic analysis for three-dimensional, nonlinear finite element analysis of prestressed concrete beams under monotonically increasing loads so long as convergence to a solution is achieved. Furthermore, unlike the explicit dynamic approach, the arc-length method allows the tracing of the complete equilibrium path, including any descending branches. However, the explicit dynamic analysis is a robust technique which is able to provide a solution in cases when the arc-length method fails.

5.11. Notation

n = a point on the equilibrium path

l_n = arc length

P_{total} = load magnitude

P_{ref} = reference load

λ = load proportionality factor

T = loading time

Δt = time increment

m = number of increments

T_n = the longest period of natural vibration

ΔT_{st} = temperature change for strands

E_{st} = elastic modulus of strands

f_{pe} = effective prestress in strands

E_c = elastic modulus of concrete

α_{st} = thermal expansion coefficient for strands

f_t = tensile strength of concrete

G_f = fracture energy for concrete

w_t = total cracking displacement of concrete

CHAPTER 6

Long Term Deformations of Precast and Prestressed Concrete Spandrel Beams

6.1. Introduction

The use of high strength concrete and prestressing steel has allowed the production of more material efficient precast and prestressed concrete structural members. In the last few years, a new generation of spandrels (thinner spandrels spanning longer distances) has begun to emerge in the precast market. They have been introduced so as to construct more cost-effective buildings and to advance the competitiveness of the precast concrete industry due to their efficiency as they reduce the number of columns required in a building. However, such slender spandrels require refinements in design and analysis methods to allow efficient utilization of these members, in particular, the influence on long-term spandrel deformations. However, comparing to the "current generation" of spandrels, slender spandrels have less sectional stiffness and larger deflections. Both vertical and lateral deflections should be considered in design since spandrels are generally subjected to eccentric loads transferred from deck beams. Consequently, it is possible that serviceability requirements rather than stress limitations may control the design of some slender spandrels. Thus, it is important to accurately estimate short-term and long-term deflections in these members. For this reason, this paper aims to provide realistic estimates of long-term deformations for the 'next generation' of longer and thinner spandrels and to gain an understanding of the parameters that affect it. A numerical study has been conducted involving a series of nonlinear finite element analyses of L-shaped, pocket and spot corbel spandrels for different span lengths (48 and 60 ft) and web thicknesses (8, 9, and 10 in.), including realistic reinforcement and prestressing strand details. The sensitivity of long-term deflections in the spandrels to various material and structural properties such as spandrel type, span length, beam width, concrete curing method, long-term effects, loading eccentricity and magnitude is presented.

6.2. Background

Precast and prestressed concrete spandrel beams (Fig. 6.1) are widely used in the perimeters of precast concrete buildings, especially parking ramps. The spandrels typically support double-tees on ledges, corbels or pockets, all of which introduce lateral eccentricity as the double tee loads are transferred to the spandrels. The torsional loading interacts with the flexural loading to generate a complex pattern of deformations that include vertical and lateral deflections, as well as twisting of the spandrel section. Creep and shrinkage of concrete further complicate the state of deformation, and after supporting dead loads for a sustained time, total deflections will include a nontrivial long-term component. To date, such deformations under full service loads have not been identified as a performance problem for the current generation of spandrels (i.e., with span lengths up to 45 ft). However, the 'next generation' of longer (up to 60 ft) and thinner (as little as 8 in.) spandrels may require detailed investigation of long-term deformations due to the combination.

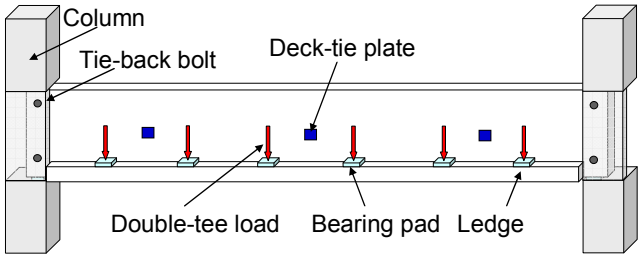

(a) L-shape spandrel beam

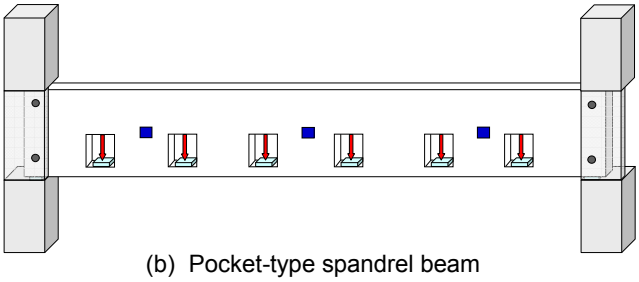

(b) Pocket-type spandrel beam

Fig. 6.1. Precast spandrel beams

Spandrels serve to support the precast concrete double-tee beams, which are used as combined deck beams and diaphragms in a precast building (Fig. 6.1). The soffit of the

spandrel typically rests on column corbels at both ends. The web of the spandrel is bolted to the column above each corbel by means of tie-backs. Upon initial placement of double tees during the erection process, when the spandrels are resisting only dead loads, they behave as simply-supported beams with no lateral restraints. Some distortion takes place in the form of lateral deflection combined with twisting as the spandrels respond to the dead loads. However, industry experience has shown that these distortions are unlikely to pose a problem at this loading stage for typical spandrel spans up to 45 ft. Moreover, the authors' experience studying the short term deflection behavior of members representative of the 'next generation' of longer, thinner spandrels suggests that short-term deflections are unlikely to be pose a problem at this loading stage. Upon connecting the spandrels to the double tees using deck ties (Fig. 6.2), these connections serve as lateral restraints for the spandrels due to the axial stiffness of the deck ties and the in-plane rigidity of the double-tee deck. Thus, lateral deflection of the spandrel is prevented at the connection points. However, given that the deck ties are thin steel plates, they are unable to constrain twisting of the spandrel section, and subsequent deformation of the spandrel will include both vertical deflection and twisting. The current generation of spandrels (i.e., with span lengths up to 45 ft) have not experienced serviceability problems due to such deformations under full service loads. Moreover, even for the 'next generation' of spandrels, these deformations are most likely not to cause any problem under short-term loadings.

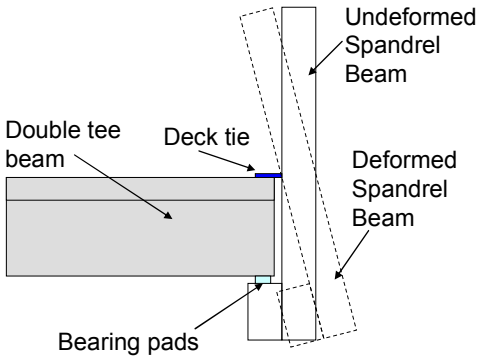

Fig. 6.2. Interaction between spandrel beam and floor diaphragm (double tee)

However, long-term loading is known to increase the magnitude of deformations in

concrete members well above the values generated upon immediate loading. There are likely to be spandrel dimensions beyond which excessive long-term deformations renders such design unfeasible. Although the next generation of spandrels leads to greater efficiency in construction arising from fewer column lines at a greater spacing, long-term deformations of longer and thinner spandrels have the potential to (a) reduce the bearing length for the double tee supports as the bottom of the spandrels kicks out (deflects laterally away from the double tee as shown in Fig. 6.2), and (b) produce unsightly distortion of the top of the spandrel as it tilts inward (deflects laterally toward the double tee, Fig. 6.3).

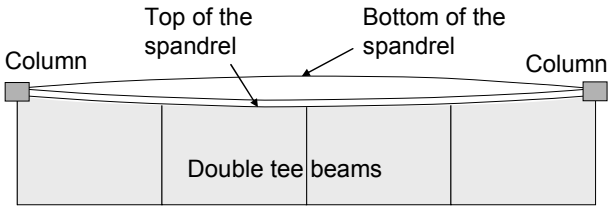

Fig. 6.3. Deformed shape of a spandrel beam under gravity loads

Therefore, this study aims (a) to provide realistic estimates of long-term deformations for the 'next generation' of longer and thinner spandrels, and (b) to gain an understanding of the parameters that affect it. To achieve these objectives, comprehensive finite element models of spandrels having various span lengths (45 and 60 ft) and web thicknesses (8, 9 and 10 in.) were generated using a well-known software package ABAQUS [19]. The FE models included realistic representation of spandrel geometry, loading configuration, material behavior of concrete (i.e., creep and shrinkage) and support conditions. The sensitivity of long-term deflections in spandrels to various material and structural properties are investigated.

Finally, a note is made here regarding the large variability in the properties of the material and structural parameters considered here. Concrete is a non-homogeneous material, and is mechanical properties (i.e., modulus of elasticity, modulus of rupture, compressive and tensile strengths, and creep and shrinkage parameters) scatter over a broad range depending on various factors; environmental conditions, loading features, water and cement contents, aggregate properties etc. Therefore, in some cases, the

estimated values of short- and long-term deflections in spandrels significantly diverge from the actual values observed in the field or in the precast plant. Better results for estimated deflections can be obtained if material and structural properties similar to those expected in the field are used in the calculations.

6.3. Literature Review

Only a limited amount of research on precast concrete spandrel beams is found in the technical literature. Most studies, [80] and [81], have been concerned with design criteria for prestressed or reinforced concrete spandrel beams subjected to combined effects of bending, shear and torsion. In 1986, an experimental study by Cleland [82] was directed towards short-term lateral deflections of reinforced concrete ledger beams (i.e., L-shaped spandrels). In this study, the ledger beams were tested in the elastic range of behavior and the experimental results are only relevant to reinforced concrete beams under short-term loading. A more recent experimental and analytical investigation on precast and prestressed concrete spandrel beams with lateral eccentricity of vertical loads was reported by Lucier et al. [83] to elucidate resistance mechanisms in the spandrels and investigate the detailing of torsional reinforcement. Nonlinear finite element models of spandrels calibrated based on the results from these full-scale tests were used to investigate the response of compact, precast and prestressed concrete spandrel beams with open web reinforcement [84]. Both of these experimental [83] and analytical [84] studies are quite comprehensive in terms of geometry and loading, but they addressed primarily the configuration of transverse reinforcement and they focused on the current generation of spandrels (with span lengths up to 45 ft) under short term loading. The conclusions from these valuable studies cannot be extrapolated to address long-term deformations in the 'next generation' of longer and thinner spandrels.

In a previous study, Mercan et al. [85] presented three-dimensional, nonlinear finite element modeling techniques for precast, prestressed concrete spandrel beams using commercial software ABAQUS. The sensitivity of the short-term lateral deflection response of spandrels to various modeling parameters such as finite element type, dilation

angle, fracture energy, tension stiffening, bearing stress distribution and support representation was presented. The long-term deformations in prestressed or partially prestressed concrete members have been studied by many researchers, [86]-[89], but all of these studies have been concerned with vertical deformations in rectangular beams subjected to concentric loads. A comprehensive assessment of 'lateral' long-term deformations in precast and prestressed concrete spandrels subjected to eccentric loading has not been undertaken.

6.4. Short-term Response of Concrete

The instantaneous response of concrete in compression or tension is affected by many factors such as the magnitude of the applied load, loading rate, concrete age and composition. For this reason, only empirical equations are available to predict the fundamental characteristics of concrete. The modulus of elasticity E_c for a normal weight concrete with a compressive strength up to 6000 psi (42 MPa) can be estimated using an empirical equation, Eq. (6.1), given in ACI 318-08. It gives the secant modulus corresponding to the intersection of concrete stress-strain curve at $0.45f'_c$. Thus, concrete can be modeled as a linear elastic material for compressive stresses less than $0.45f_c'$, as given in Eq.(6.2). Beyond this limit value, the stress-strain relationship for concrete becomes nonlinear. Popovics [122] summarized empirical formulas available in literature for predicting the short term response of concrete. Equation (6.3) is one of such empirical formulas. The concrete strain ε_o corresponding to the compressive strength f'_c is approximately equal to 0.002.

$$E_c = 57{,}000\sqrt{f_c'} \text{ , psi or } E_c = 4{,}800\sqrt{f_c'} \text{ , MPa} \tag{6.1}$$

$$f_c = E_c\varepsilon_c \text{ for } f_c \le 0.45f_c' \tag{6.2}$$

$$f_c = f_c'\left[\frac{2\varepsilon_c}{\varepsilon_o} - \left(\frac{\varepsilon_c}{\varepsilon_o}\right)^2\right] \text{for } f_c > 0.45f_c' \tag{6.3}$$

The deflection response of concrete is influenced highly by cracking and post-cracking properties of concrete. ACI 318-08 recommends Eq. (6.4) for estimating the modulus of

rupture f_r for normal density concrete, 145 to 150 pcf (2325 to 2400 kg/m^3). For high strength concrete for which the compressive strength f'_c at 28 days is greater than 6000 psi (42 MPa), the modulus of rupture can increase up to the value of $12\sqrt{f'_c}$ in psi.

$$f_r = 7.5\sqrt{f_c'} \text{ , psi or } f_r = 0.623\sqrt{f_c'} \text{ , MPa} \tag{6.4}$$

Hillerborg et al. [123] proposed a brittle fracture concept using fracture energy in order to define the post-cracking behavior of concrete. Fracture energy G_f is a material property which defines the energy required to open a unit area of crack. Its magnitude is equal to the area under the stress-displacement curve, in the post cracking regime of a concrete specimen in a direct tensile test. For example, the fracture energy for a high strength concrete with a compressive strength of 6000 psi (42 MPa) is approximately equal to 0.67 lb/in (120 N/m). During the test, cracks generally localize in a process zone, leading to a non-unique stress-strain relationship in tension. Therefore, the post-cracking response is usually represented by the relationship between stress and displacement (or crack width), rather than stress and strain. Displacement depends on the opening at the crack regardless of the specimen length. The ultimate cracking displacement u_{tu} at which the concrete stress attains zero value can be found in terms of the fracture energy G_f and the tensile strength f_r as in Eqs.(6.5) and (6.6). It assumes that concrete exhibits linearly descending post-cracking regime. If the characteristic crack length L_o is known, Eq. (6.5) can be rearranged for predicting the ultimate tensile strain ε_{tu} as given in Eq. (6.6).

$$u_{tu} = \frac{2G_f}{f_r} \tag{6.5}$$

$$\varepsilon_{tu} = \frac{2G_f}{L_o f_r} \tag{6.6}$$

A summary of the discussion above is presented in the tension side of the stress-strain behavior of concrete under uniaxial compression and tension shown in Fig. 6.4. For the prestressed concrete spandrel beams under service load conditions, the maximum compressive stress in concrete is typically less than $0.45f_c'$ and the assumption for concrete behavior in the inelastic compressive regime affects slightly spandrel

deflections.

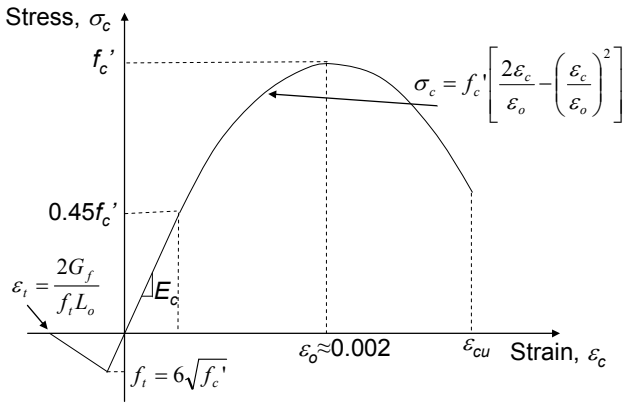

Fig. 6.4. Uniaxial stress-strain behavior of concrete

The accuracy of the results from the finite element analysis depends highly on how the concrete material model has been defined for both short- and long-term effects. The concrete damage-plasticity model provided in ABAQUS is used in this study for modeling the short-term response of concrete. The detailed description of the concrete damage-plasticity model and the effect of various modeling parameters on the short term deflection response of spandrel beams were previously reported by Mercan et al. [85]. A short summary of this material model for concrete is herein presented.

The finite element model in ABAQUS requires a linear elastic and isotropic behavior of concrete when the concrete strain ε_c is less than the cracking strain in tension (ε_t) or the compressive strain (ε_p) at which the irreversible deformations initiate in concrete. Inelastic behavior of concrete, mainly influenced by micro-cracking, includes strain-softening in tension and stress hardening followed by strain softening in compression. In the damage-plasticity model, such inelastic characteristics of concrete are represented by the combination of two concepts: (a) damage in which the unloading response of the concrete specimen in the inelastic regime exhibits stiffness degradation; and (b) plasticity in which, a flow rule, a yield function and a hardening rule are defined as in the classical metal plasticity.

The concrete damage-plasticity model uses tension stiffening approach in order to distinguish the behavior of reinforced concrete from that of plain concrete. Reinforced

concrete exhibits a "stiffer" strain softening regime in tension than does plain concrete since cracked reinforced concrete continues transferring stress through the rebar. In general, tension stiffening is defined by (a) a post failure stress-displacement curve or (b) a post-failure stress-fracture energy curve. The amount of tension stiffening effect that needs to be introduced to the model is not easy to determine due to the fact that tension stiffening depends highly on the reinforcement details, rebar size and concrete aggregate size. In the modeling of highly reinforced concrete members (i.e., prestressed concrete spandrels), the tension stiffening effect can be introduced by simply increasing the fracture energy of plain concrete by a factor of ten [19].

6.5. Long-term Response of Concrete

6.5.1. Overview

Time-dependent volume changes of concrete such as shrinkage and creep always occur in concrete members and they are of particular importance in prestressed concrete members because they affect the magnitude of effective prestress. Creep is the time dependent increase of strain in hardened concrete subjected to sustained stress and defined as a strain per unit stress. Shrinkage is a volumetric change due to changes in the moisture content of the concrete and physico-chemical changes, which occur without stress attributable to actions external to the concrete. The magnitude of strains in concrete due to creep and shrinkage is affected by many factors such as relative humidity, volume-to-surface area ratio and the composition of concrete (e.g., cement paste, aggregate, water-cement ratio, and cement content).

Fig. 6.5 illustrates an idealized variation of the compressive strain in a concrete specimen subjected to a constant stress. Before applying the load, the concrete specimen experiences only shrinkage strain with a reducing rate in time. When the specimen is subjected to the constant stress, an immediate increase occurs in concrete strains, which may exceed the elastic range for concrete (approximately equal to the strain corresponding to 45 percent of the compressive strength for concrete). Even though the load is kept constant, the compressive strain in concrete continues increasing in time due

to both creep and shrinkage effects and there is a nonlinear relationship between the total strain and time. Unloading the specimen leads to an elastic strain recovery of concrete, but the specimen may still experience a slight increase in strain due to shrinkage.

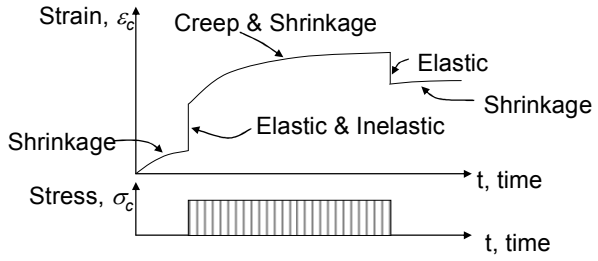

Fig. 6.5. The variation of concrete strain in time

Thus, ignoring the interaction between creep and shrinkage effects and assuming elastic deformations only (no cracking or crushing in concrete), the total strain $\varepsilon_c(t)$ in concrete at time t can be defined as the sum of the instantaneous elastic strain ε_{ins} due to a constant stress σ_c applied at time t_o, creep strain $\varepsilon_{cr}(t,t_o)$ and shrinkage strain $\varepsilon_{sh}(t)$.

$$\varepsilon_c(t) = \varepsilon_{ins} + \varepsilon_{cr}(t,t_o) + \varepsilon_{sh}(t) \tag{6.7}$$

Even though there is a nonlinear relationship between the creep strain and the sustained load, it is assumed that the creep strain $\varepsilon_{cr}(t,t_o)$ is proportional to the stress σ_c when it is less than 40 percent of the compressive strength of concrete f'_c. So, instead of using the creep strain, the effect of creep is introduced into equation (6.7) as a factor for the instantaneous elastic strain ε_{ins} and hence equation (6.7) is given in the form of

$$\varepsilon_c(t) = [1 + v(t,t_o)]\varepsilon_{ins} + \varepsilon_{sh}(t) \tag{6.8}$$

where $v(t,t_o)$ is the creep coefficient representing the ratio of the creep strain at time t to the instantaneous strain that occurred at time t_o.

Numerous models for predicting creep and shrinkage behavior of concrete have been proposed [119]-[121]. The ACI 209R-92 model [119], which has been widely used in research and practice, was adopted in this study. It is an empirical model for predicting creep and shrinkage strains in concrete, developed by Branson and Christiason, and first introduced in the ACI 209R-82 report. The model has a hyperbolic curve which is defined as a function of time and asymptotic to the ultimate value for creep coefficient v_u

or shrinkage strain ε_{shu}. The shape of the curve and ultimate values are affected by several factors such as concrete composition, initial curing, environment, geometry, loading history and stress conditions etc. These factors are considered in the model by referring to "standard conditions" and "correction factors other than standard conditions". Correction factors, γ_{sh} and γ_c, are used to modify ultimate values for shrinkage and creep. In the absence of specific creep and shrinkage data for concrete mixed using local aggregates and cured under specific conditions, the ACI 209R-92 model recommends using the following equations for predicting creep and shrinkage for concrete in standard conditions listed in Table 6.1:

Creep coefficient at time t in days:

$$v(t) = \frac{t^{0.6}}{10 + t^{0.6}} v_u \tag{6.9}$$

$$v_u = 2.35\gamma_c \tag{6.10}$$

It should be noted that for standard conditions the creep coefficient is not defined as a function of loading time t_o. There is a correction factor for loading ages later than 7 days for moist cured concrete and later than 1-3 days for steam cured concrete.

The shrinkage equation at time t after age 7 days for moist cured concrete:

$$\varepsilon_{sh}(t) = \frac{t}{35 + t} \varepsilon_{shu} \tag{6.11}$$

The shrinkage equation at time t after age 1-3 days for steam cured concrete:

$$\varepsilon_{sh}(t) = \frac{t}{55 + t} \varepsilon_{shu} \tag{6.12}$$

And, the ultimate shrinkage strain:

$$\varepsilon_{shu} = 780 \times 10^{-6} \gamma_{sh} \tag{6.13}$$

where the factors of γ_{sh} and γ_c are the product of the applicable correction factors in ACI 209R-92.

Table 6.1. Factors affecting concrete creep and shrinkage considered in ACI 209 Model

Factors			Variables considered	Standard Conditions
Concrete (creep and Shrinkage)	Concrete Composition	Cement paste content	Type of cement	Type I and III
		Water-cement ratio	Slump	70 mm (2.7 in.)
		Mixture proportions	Air content	≤ 6%
		Aggregate characteristics	Fine aggregate percentage	50%
		Degree of compaction	Cement content	279 to 446 kg/m^3 (470 to 752 lb/yd^3)
	Initial Curing	Length of initial curing	Moist cured	7
			Steam cured	1 to 3 days
		Curing temperature	Moist cured	23.2 ± 2 °C (73.4 ± 4 °F)
			Steam cured	≤ 100 °C (≤ 212 °F)
		Curing humidity	Relative humidity	≥ 95%
Member geometry and environment (creep and shrinkage)	Environment	Concrete temperature	Concrete temperature	23.2 ± 2 °C (73.4 ± 4 °F)
		Concrete water content	Ambient relative humidity	40%
	Geometry	Size and shape	Volume-surface ratio or minimum thickness	V/S= 38 mm (1.5 in.)
				150 mm (6 in.)
Load (creep only)	Load history	Concrete age at load application	Moist cured	7 days
			Steam cured	1 to 3 days
		During of loading period	Sustained load	Sustained load
		Duration of unloading period	_	_
		Number of load cycles	_	_
	Stress conditions	Type of stress and distribution across the section	Compressive stress	Axial compression
		Stress/strength ratio	Stress/strength ratio	≤ 0.5

6.5.2. Finite Element Modeling

For finite element analysis of spandrels using ABAQUS, shrinkage strains in concrete can be introduced by varying the coefficient of thermal expansion α and temperature T as a function of time t. In other words, solid continuum elements of concrete are subjected to a temperature change so that thermal strains replace shrinkage strains. The main advantage of such modeling procedure for shrinkage strains is that the problem can be solved by using static finite element procedures without any additional thermal analysis methods. The thermal strain ε_{th} at time t is computed by multiplying the coefficient of thermal expansion $\alpha(t)$ by the temperature change $T(t) - T(0)$, as given in Eq. (6.14). Thermal expansion (or contraction for shrinkage effect) results in isotropic response so that the strain increment remains the same in all directions. For simplicity, the initial

temperature *T(0)* is assumed to be zero. Such assumption can be made since the main objective of FE analysis is not to investigate the thermal response of spandrels. Thus, thermal strain equation can be reduced to Eq (6.15). By setting the thermal strain $\varepsilon_{th}(t)$, in Eq. (6.15), to be equal to the shrinkage strain $\varepsilon_{sh}(t)$, in Eq. (6.11) or Eq. (6.12), the expressions for the coefficient of thermal expansion $\alpha(t)$ are obtained for moist cured or steam cured concrete as seen in Eq. (6.16). The negative signs represent the case of contraction (shrinkage) in concrete with an increase of time or temperature. The variation of temperature T in time t (in this case, assume $T=t$ for simplicity) is defined by introducing a predefined field variable into the solid continuum elements of concrete.

$$\varepsilon_{th}(t) = \alpha(t)\left[T(t) - T(0)\right] \tag{6.14}$$

$$\varepsilon_{th}(t) = \alpha(t)\,t \tag{6.15}$$

$$\alpha(t) = -\frac{\varepsilon_{shu}}{35+t} \text{ for moist cured concrete}$$
$$\alpha(t) = -\frac{\varepsilon_{shu}}{55+t} \text{ for steam cured concrete} \tag{6.16}$$

For creep analysis, ACI 209R-92 recommends the use of two different methods; the Effective Modulus Method (EMM) when the gradual time change of stress due to creep and shrinkage is small and the Age-adjusted Effective Modulus Method [119] when the gradual time change of stress is significant. The latter method is not employed in this study since (a) the constant sustained loads (i.e., double tee loads) are assumed to instantaneously act at the beginning of the time-dependent analysis (or drying), (b) the redistribution of internal forces in spandrels due to concrete cracking is negligible under service load conditions.

Effective Modulus Method (EMM) in the creep analysis is treated as an elastic analysis with a time-dependent reduced modulus that replaces the elastic modulus [119]. The creep strain is calculated using the final stress distribution and depends on the previously accumulated creep strains. The EMM method provides sufficiently accurate results when the concrete stress does not vary significantly. The load-dependent strain, the sum of the instantaneous strain ε_{ins} and the creep strain $\varepsilon_{cr}(t)$ due to the sustained load σ_o is computed using Eq. (6.17). The elastic modulus of concrete E_c, which has a

constant value, equal to modulus of elasticity of concrete at the time of initial load, can be estimated using Eq. (6.1). Rearranging Eq. (6.17) with the creep equation (6.9) gives Eq. (6.18), where the effective elastic modulus for concrete E_{eff} as a function of time t, Eq. (6.19), is obtained.

$$\varepsilon_{ins} + \varepsilon_{cr}(t) = [1 + v(t)]\sigma_o / E_c \tag{6.17}$$

$$\varepsilon_{ins} + \varepsilon_{cr}(t) = \sigma_o / E_{eff}(t) \tag{6.18}$$

$$\text{where } E_{eff}(t) = \frac{E_c}{1 + v(t)} = \frac{E_c}{1 + \frac{t^{0.6}}{10 + t^{0.6}} v_u} \tag{6.19}$$

The time dependent behavior of concrete in tension is also considered in the model. In general, the tensile creep is three times larger than the compressive creep [94]. Implementing the EMM combined with the concrete damage-plasticity model leads to the use of the same creep coefficient for tension and compression. However, such assumption does not produce significant error in the results [126]. Furthermore, the model assumes that the initiation and propagation of cracks in concrete are not influenced by the creep effect, but the shrinkage can still create cracking in concrete since spandrel beams are statically indeterminate. Test results show that the tension-stiffening effect for concrete reduces to its ultimate value in 20 days after loading [125], and hence does not need to be modified for long-term effects.

6.5.3. Experimental verification for reinforced concrete beams

The reliability and accuracy of the EMM for estimating creep deformations and the thermal expansion method for shrinkage deformations of reinforced concrete beams were discussed in this section by comparing the results of finite element analysis with those of experiment. For the purpose of verification, an experimental study conducted by Corley and Sozen [91] was selected. The details of beams tested are shown in Fig. 6.6. Time dependent deflections of the beams were monitored over a period of two years. Three beams (1, 3 and 4) were loaded up to P= 2,240 lb (9.96 kN) and kept constant for two years. However, Beam 2 was first subjected to the same load, resulting in cracking, and then unloaded. Additionally, one 4×6-in (100x150 mm) cylinder specimen was tested

under the sustained compressive stress of 1,350 psi (9.3MPa) whereas another cylinder specimen was not subjected to any load. All beams and cylinders were kept in the same environmental conditions [70ºF (21ºC) and %50RH]. The material properties for concrete used in the damage-plasticity model are as follows: E_c= 2,265x10^3 psi (15.6 MPa), ν= 0.15, f'_c= 3,000 psi (20.7 MPa), ε_{cu}= 0.0038, f_t= 329 psi (2.27 MPa), G_f= 5 lb/in (876 N/m), L_o=1 in (25.4mm). It should be noted that the compressive strength of concrete was the only parameter known. The initial elastic modulus, E_c was obtained from the test results for loaded cylinder specimen. Other parameters used in the concrete damage plasticity model were estimated using the empirical equations previously discussed as described below.

First, ACI creep and shrinkage equations (6.9) and (6.11) were calibrated against the cylinder test results by adjusting the values of the ultimate shrinkage strain ε_{shu} and the ultimate creep coefficient v_u. The unloaded specimen was under the shrinkage effect only, whereas the loaded specimen was subjected to both creep and shrinkage effects. The shortening of the unloaded cylinder specimen was approximately 0.0003 at the end of two years. Therefore, the value of the ultimate shrinkage strain ε_{shu} was calculated as 314× 10^{-6} by Eq. (6.11) as follows:

$$\varepsilon_{shu} = \frac{35+t}{t}\varepsilon_{sh}(t) = \frac{35+2\times 365}{2\times 365}0.0003 = 314\times 10^{-6} \tag{6.20}$$

A brick element in ABAQUS was subjected to thermal expansion in order to analyze the shrinkage response of unloaded cylinder specimen tested. The specimen was free to deform in transverse directions. Short-term behavior of concrete was defined with concrete damage-plasticity model and parameters described above. Shrinkage strains determined based on the ACI equation (ε_{shu} =314×10^{-6}) were defined with equivalent thermal strains in ABAQUS, which were introduced into the model by changing temperature and thermal expansion coefficient for the concrete. The results of the finite element analysis and test for unloaded specimen were in good agreement as seen in Fig. 6.7.

For the calibration of the finite element model for the creep response of concrete, the brick element previously used for the unloaded case (or shrinkage) was subjected to the

sustained stress of 1,350 psi (9.3 MPa) in one direction over the period of two years. The EMM, discussed in detail above, was used for modeling the creep behavior of concrete. When the ultimate creep coefficient v_u was taken as 2.5, finite element analysis provided a very good estimation for long term deformations in the loaded cylinder specimen, as seen in Fig. 6.7.

Finally, three-dimensional finite element models of rectangular reinforced concrete beams were generated based on the beams details and loading conditions described above. In the finite element simulation of these beams, concrete was defined using 8 node brick elements and the concrete damage-plasticity model, whereas reinforcement was defined using truss elements and the elastic-perfectly plastic material model based on the elastic modulus of 29000 ksi (200 GPa) and the yield stress of 60 ksi (413 MPa). Even though reinforcement was embedded into the concrete solid and fully restrained, the rebar-concrete interaction was introduced to the model through the tension stiffening effect. Creep and shrinkage characteristics of concrete in beams were in accordance with the results from the finite element analyses of cylinder specimens (ε_{shu} =314×10^{-6} and v_u= 2.5). Fig. 6.8 shows the time-dependent mid-span deflections of the beams. The results from the finite element analyses are in very good agreement with those measured during the tests. Thus, it is concluded that the EMM and concrete damage plasticity model predicts the long-term behavior for reinforced concrete beams with an acceptable accuracy.

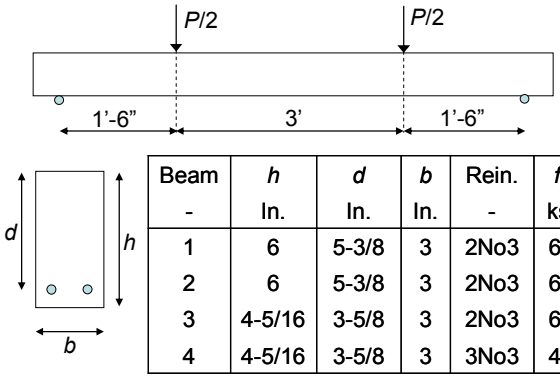

Beam	h	d	b	Rein.	f_y
-	In.	In.	In.	-	ksi
1	6	5-3/8	3	2No3	60
2	6	5-3/8	3	2No3	60
3	4-5/16	3-5/8	3	2No3	60
4	4-5/16	3-5/8	3	3No3	40

Fig. 6.6. Details of beams (1 in= 25.4 mm, 1 ksi=6.89MPa, 1 kips= 4.448 kN, 1 lb/in=175 N/m)

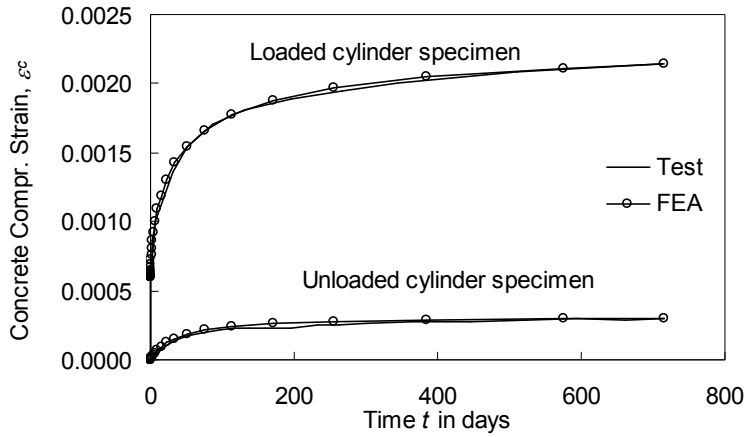

Fig. 6.7. Strains of loaded and unloaded cylinder specimens

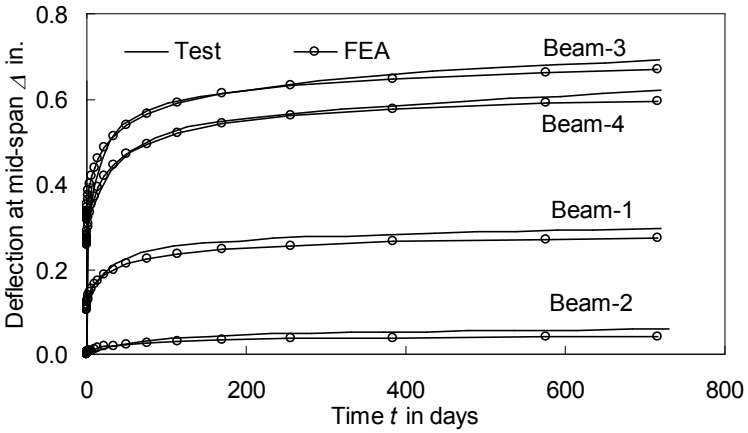

Fig. 6.8. Deflections at mid-spans (1 in=25.4 mm)

6.5.4. Experimental verification for prestressed concrete beams

Branson and Shaikh [127] tested a series of 15-ft long, simply supported, prestressed concrete beams (6 in. by 8 in.) in order to investigate the effect of non-tensioned steel on the time-dependent behavior of prestressed concrete beams. All test beams and cylinder specimens were moist-cured for 7 days. The temperature in the laboratory was around 72 ºF. Two beams with pretension steel only, Beam-1 and Beam-2, were analyzed herein. The 7 day and 28 day concrete compressive strengths of the beams were 4830 psi and 6570 psi, respectively. Beam-1 included three 5/16-diameter prestressing strands (A_s=0.173 in^2), located at the effective depth of 6.5 in. and subjected to the initial

prestressing force 30.5 kips. Beam-2 included three 3/8-diameter prestressing strands (A_s=0.240 in^2), located at the effective depth of 6.5 in. and subjected to the initial prestressing force 29.8 kips. Short-term mid-span camber occurring at the release of prestress and long-term camber due to creep and shrinkage were measured during three months.

The instantaneous elastic shortening ε_{ins} in the cylinder specimens (A_c=28.27 in^2), subjected to the sustained load of 55 kip, was measured as 465×10^{-6}. Therefore, the elastic modulus of concrete E_c is approximately equal to 4183 ksi. Using the cylinder test data, the ultimate creep coefficient v_u and the ultimate shrinkage strain ε_{shu} in Equations (6.9) and (6.11) were determined as 2.83 and 844×10^{-6}, respectively. For cylinder specimens, the experimental strain values together with the prediction of finite element analysis based on EMM is presented in Fig. 6.9. A good agreement between computational and experimental results was achieved for the creep behavior over the entire time range and for the shrinkage after the first 50 days. Next, three-dimensional finite element models of Beam-1 and Beam-2 were generated using modeling techniques similar to those in the example of reinforced concrete beams, described above. Due to the combined effect of the prestressing force and the self-weight of the beams, the initial camber at the mid-span of the beams was measured in the value of 0.225-in. Creep and shrinkage effects in concrete and the loss of the presstressing force in strands led to an increase on the time-dependent cambers. It is concluded that the finite element model based on the EMM for creep, the thermal expansion procedure for shrinkage, and the damage-plasticity model for the short-term concrete response describes the long-term response of prestressed concrete beams tested quite well, especially after the first 50 days, as seen in Fig. 6.10. However, the results of the finite element analysis were slightly stiffer at early ages of concrete, possibly due to the discrepancy between actual and computed shrinkage effects.

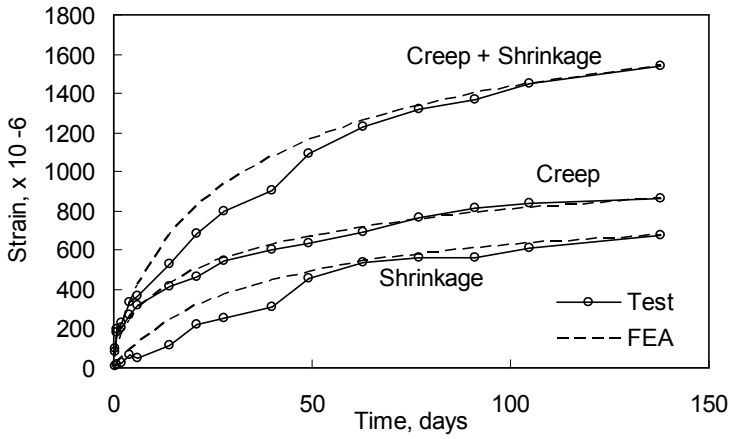

Fig. 6.9. FE analysis vs. test results for cylinder specimens

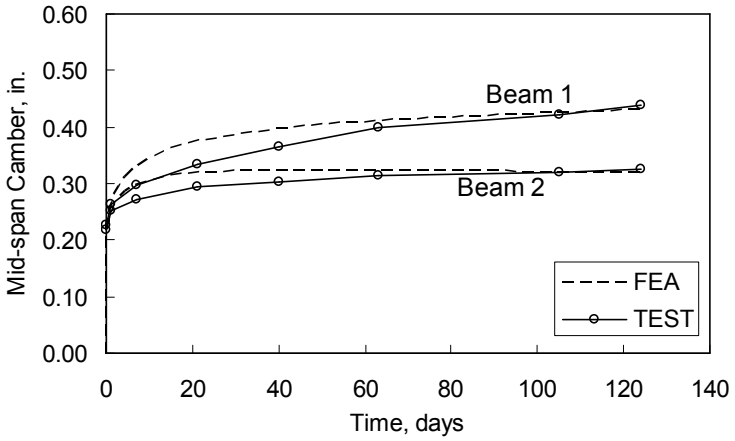

Fig. 6.10. Time dependent camber at the mid-span of prestressed concrete beams

6.6. Description of Prototype Spandrel Beams

Spandrels are often categorized by the features of their configuration which serve to support the deck members (e.g. the double-tee beams). "L-shaped" spandrels have a continuous horizontal ledge, "pocket" spandrels have rectangular cutouts on which double-tees are supported. The latter configuration provides support only at the locations of the double-tee webs. The "corbel" spandrel has discontinuous ledges only at the location of the double-tee webs. Due to the similarity with the "L-shaped" spandrels, they are not considered here. The height and width of a typical spandrel vary from 60 to 83 in. and 10 to 12 in., respectively. Today, technological advances in fabrication and

erection enable precasters to produce the "next generation" of spandrels with the span length that can be as long as 60 ft, and with a web width as thin as 8 in. Therefore, a set of prototype spandrels, that are representative of the 'next generation' of the spandrel beams, is defined.

Precast and prestressed concrete spandrel beams in various configurations were designed in order to achieve a range of long-term lateral deflections under service loads. The main design parameters included the spandrel type ("L-shaped" or "pocket"), the span length (48 ft and 60 ft) and the web width (8 in, 9 in, and 10 in.). The height *h* of all spandrels was 83 in. The cross-sectional dimensions of the prototype L-shape and pocket spandrels are presented in Fig. 6.11.

Spandrels were designed in accordance with the *ACI 318-08* document, the *International Building Code* (IBC 2009 Edition), *Minimum Design Loads for Buildings and Other Structures* (ASCE 7-05). The compressive strength of concrete was assumed to be 6000 psi for all spandrels. Fig. 6.12 shows the design details of prototype spandrels. It was assumed that spandrels supported one end of 60 ft-long double-tee beams (12DT30), which have a 12 ft-wide top flange and the self-weight of 81 psf. Four double-tee beams of 12DT30 rested on 48-ft long spandrels, whereas five double-tees were on 60-ft spandrels. Live and snow loads acting on double tees were assumed as 40 and 30 psf, respectively. Thus, double-tee stem loads (depicted as concentrated loads in Fig. 6.12) acting on the ledges of L-shaped spandrels and in the cut-outs of pocket spandrels, were placed at typical spacing of 6 ft. The computed dead, live and snow loads, respectively, were 14.5 kips, 7.2 kips and 5.4 kips. In addition to the double-tee loads, the self-weight of spandrels were obtained by assuming a unit weight of concrete equal to 150 pcf. Deck-tie restraints were located at the mid-height level of a typical spandrel beam (3'-6" from the top) with 8-ft spacing. Two tie-back bolts restraining the twisting deformations of the spandrel at the ends were located at the distance of 6-in from the end and 12-in from the top and bottom of the spandrel (Fig. 6.12).

The design of the spandrels for the loads defined above yielded two typical strand patterns, as seen in Fig. 6.13. Strand pattern 1 (SP1), consisting of 10 strands in total, was provided in 48-ft long spandrels regardless of spandrel type (i.e., L-shape or pocket).

Strand pattern 2 (SP2) included 16 strands and were used in all of the 60-ft spandrels. The prestressing steel was ½ -in. diameter seven wire strand (pulled to 75% of strand ultimate stress) with a nominal diameter of 0.167 in^2 and a specified tensile strength, f_{pu}, of 270 ksi. The details of non-prestressing steel, used in the spandrels with yield strength of 60 ksi, are shown in Fig. 6.14.

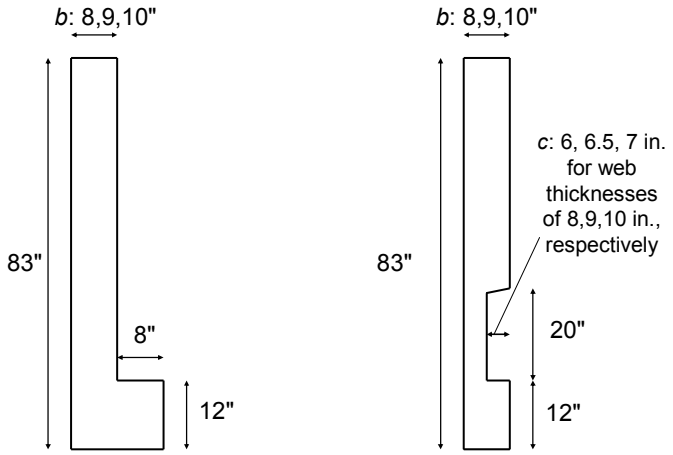

(a) L-shape (b) Pocket

Fig. 6.11. Cross-sections of prototype spandrels considered

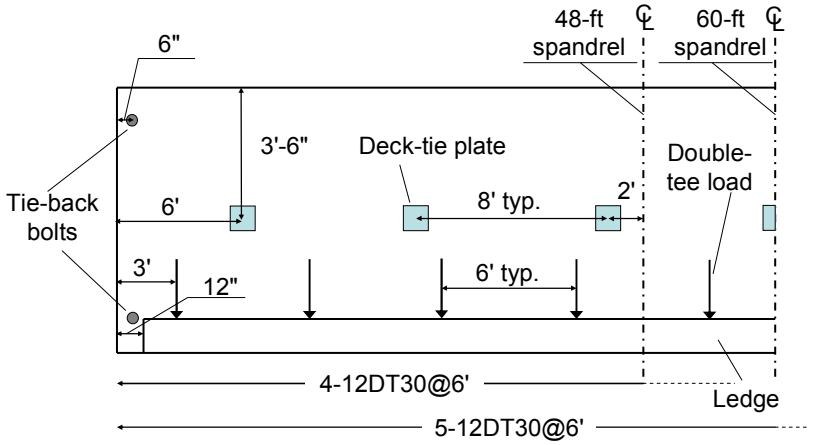

(a) L-shape spandrels

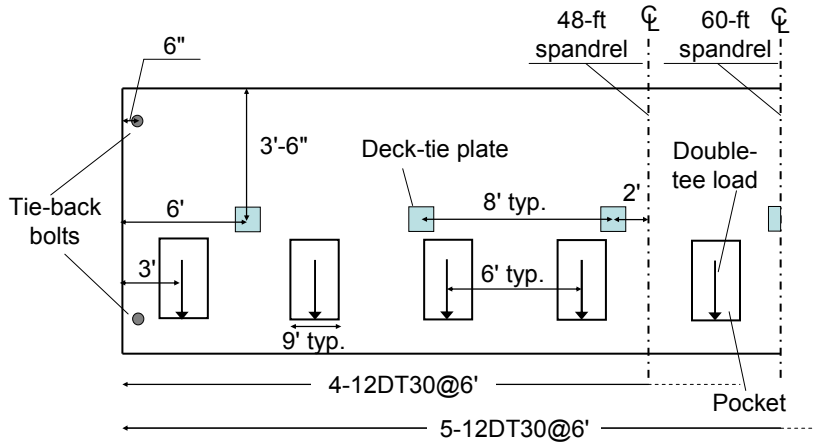

(b) Pocket spandrels

Fig. 6.12. Geometry of 48-ft and 60-ft prototype spandrels

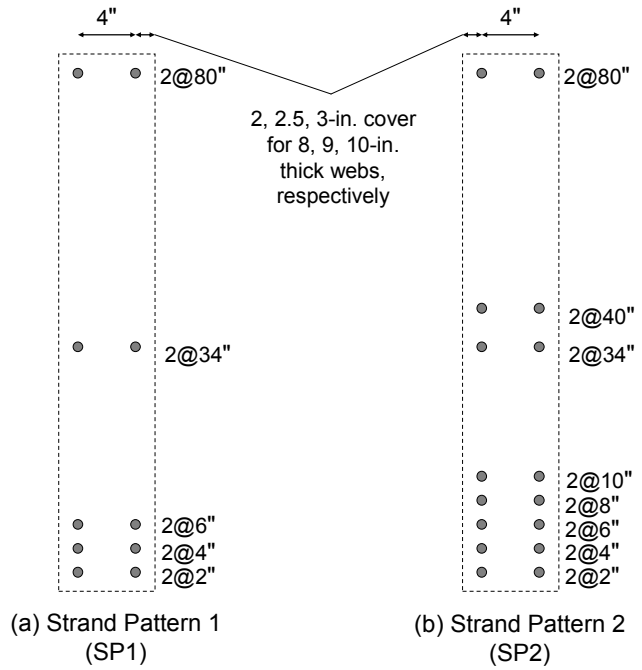

Fig. 6.13. Typical strand details: (a) SP1 for 48-ft spandrels and (b) SP2 for 60-ft spandrels (Dimensions shown are strand location from soffit)

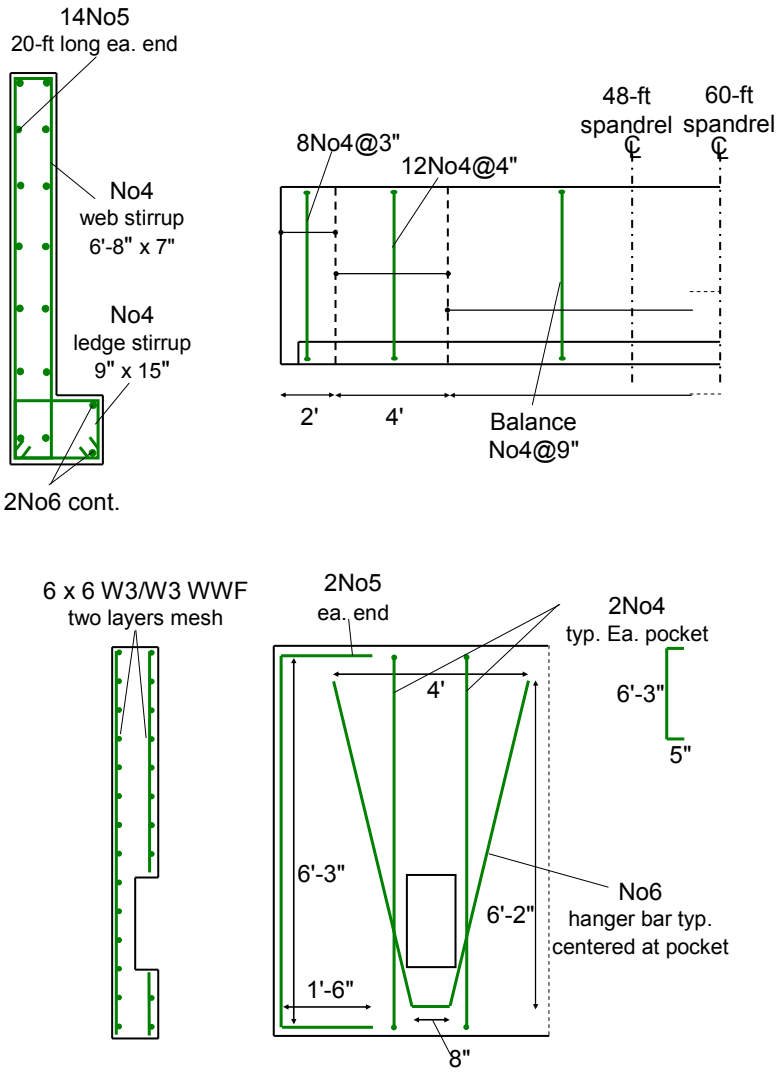

Fig. 6.14. Reinforcement details for L-shape and pocket spandrels

6.7. Creep and Shrinkage Effects for Spandrel Beams

Creep and shrinkage effects for concrete are influenced by various factors, as listed in Table 6.1, which lead to a wide range of values for correction factors that are applied to the ultimate creep coefficient (2.35) and ultimate shrinkage strain (780×10^{-6}) when concrete is not under the standard conditions. The investigation of spandrels for every single possible condition, however, is not practical. Therefore, assuming values for these corrections that bracket a practical range is crucial for estimating long-term deflections in precast spandrels.

An informal survey of several concrete precasters was conducted to assess typical values for the variables affecting creep and shrinkage behavior of concrete in spandrels. Table 6.2 shows these variables, the values for these variables obtained from the informal survey, and the corresponding values for correction factors determined based on the ACI 209 model. For each variable, three values were selected and designated as high, medium and low depending upon their effect on creep and shrinakge. For example, loading age is a factor affecting the creep of steam-cured concrete. The effect of creep reduces with an increase of loading age. In standard conditions, ACI 209 model assumes that steam-cured concrete is loaded at age of 1-3 days. In this study, three different loading ages, 7, 28 and 90 days, corresponding to high, medium and low creep effects, respectively, were considered.

Finally, the correction factors for the ultimate creep coefficient and shrinkage strain, Table 6.3, were obtained by multiplying values tabulated in Table 6.2. For example, the correction factor for creep of moist cured concrete, assuming a "high" level of long-term effects, was obtained as 1.07, equal to the multiplication of factors, 1.00 for the loading age of 7 days, 1.00 for 40% relative humidity, 0.77 for average thickness, 1.16 for 5-in. (13 cm) slump, 1.02 for 60% fine aggregate percentage, and 1.18 for 8% air content. Table 6.3 indicates the correction factors are close to unity for a "high" level of long-term effects for both types of curing. Therefore, the ultimate creep coefficient (2.35) and ultimate shrinkage strain (780×10^{-6}) for standard conditions recommended by ACI 209 committee report generally results in a conservative assumption for long term effects in spandrel beams.

Table 6.2. Factors affecting concrete creep and shrinkage considered in ACI 209 Model

Variables affecting concrete creep and shrinkage	Level of long-term (LT) effects	Values for variables considered	Correction Factors	
			Creep	Shrinkage
Loading age for steam cured concrete	High	7 days	0.94	-
	Medium	28 days	0.83	-
	Low	90 days	0.74	-
Loading age for moist cured concrete	High	7 days	1.00	-
	Medium	28 days	0.83	-
	Low	90 days	0.74	-
Moist Curing Duration	High	1 day	-	1.20
	Medium	3 days	-	1.10
	Low	7 days	-	1.00
Relative Humidity	High	40%	1.00	1.00
	Medium	60%	0.87	0.80
	Low	80%	0.73	0.60
Average Thickness (V/S approach)	High	8 in.	0.77	0.77
	Medium	9 in.	0.75	0.74
	Low	10 in.	0.74	0.71
Slump in.	High	5	1.16	1.10
	Medium	2.7	1.00	1.00
	Low	0.5	0.85	0.91
Fine Aggregate Percentage (ratio of fine aggregate to total aggregate by weight)	High	60	1.02	1.02
	Medium	50	1.00	1.00
	Low	40	0.98	0.86
Cement Content lb/yd^3	High	800	-	1.04
	Medium	700	-	1.00
	Low	600	-	0.97
Air Content Percentage	High	8	1.18	1.01
	Medium	6	1.00	1.00
	Low	3	1.00	0.97

Table 6.3. Correction factors for conditions other than standard

Level of long-term (LT) effects	Corrections for Moist Cured Concrete		Corrections for Steam Cured Concrete	
	Creep	Shrinkage	Creep	Shrinkage
High	1.07	1.09	1.01	0.91
Medium	0.54	0.65	0.54	0.59
Low	0.33	0.31	0.33	0.31

6.8. Modeling of Spandrel Beams

The computational study using ABAQUS included three-dimensional models of spandrel beams. Referring to Table 6.4, the parametric study of the spandrels included the following variables; spandrel type (L-shape and pocket), span length (48 and 60 ft), web width (8, 9, and 10 in.), concrete curing conditions (moist and steam), long term effects (high, medium and low), instantaneous loads (DL, DL+0.5LL and DL+LL) and load locations (s=0.50c, 0.75c, and 1.0c, seen in Fig. 6.15). The term s describes the distance from the location of load to the face of the spandrel web. The exact location of the resultant point load P along the support width c is not known. Therefore, three different locations 0.5c, 0.75c and 1.0c were considered as possible locations for the resultant point load P. Due to a large variety of parameters, baseline spandrel models were first generated and analyzed. Next, by altering the baseline model for various parameters, the sensitivity of spandrel response to these parameters was evaluated. Basic characteristics of these baseline models are tabulated in Table 6.5. All of these models were based on moist cured concrete, high long-term effects, 50% of live load, and the eccentricity e_c for the load location s=0.5c. By varying spandrel type, length and width, twelve baseline models were created.

Table 6.4. Spandrel parameters considered in the finite element simulations

Spandrel Type	Span Length [ft]	Web Width [in]	Curing Type	Level of Long Term (LT) Effects	Instantaneous Load	Load Locations s
L-shape	48	8	Moist	High	DL	0.50c
Pocket	60	9	Steam	Medium	DL+0.5LL	0.75c
		10		Low	DL+0.75LL	1.00c

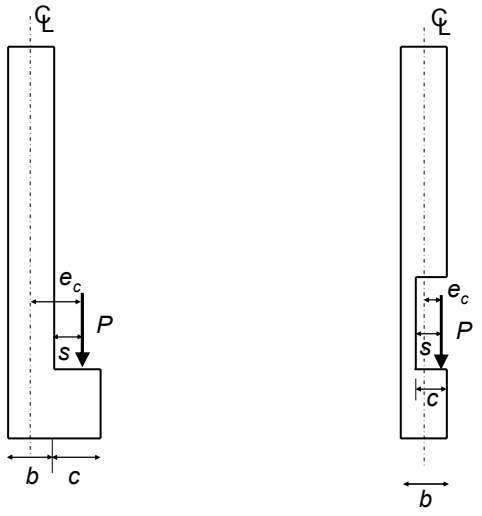

(a) L-shape (b) Pocket

Fig. 6.15. Load locations for L-shape and pocket spandrels (the eccentricity e_c=b/2+s for L-shape and e_c=b/2+s-c for Pocket)

Table 6.5. Basic characteristics of baseline spandrel models

Designation	Spandrel Type	Span Length [ft]	Web Width [in]	Curing Type	Level of Long Term (LT) Effects	Instant Load	Load Location s	Support width c [in]	Eccentricity e_c [in]
L4808	L-shape	48	8	Moist	High	DL+0.5LL	0.50c	8.0	8.00
L4809	L-shape	48	9	Moist	High	DL+0.5LL	0.50c	8.0	8.50
L4810	L-shape	48	10	Moist	High	DL+0.5LL	0.50c	8.0	9.00
P4808	L-shape	60	8	Moist	High	DL+0.5LL	0.50c	6.0	7.00
P4809	L-shape	60	9	Moist	High	DL+0.5LL	0.50c	6.5	7.75
P4810	L-shape	60	10	Moist	High	DL+0.5LL	0.50c	7.0	8.25
L6008	Pocket	48	8	Moist	High	DL+0.5LL	0.50c	8.0	8.00
L6009	Pocket	48	9	Moist	High	DL+0.5LL	0.50c	8.0	8.50
L6010	Pocket	48	10	Moist	High	DL+0.5LL	0.50c	8.0	9.00
P6008	Pocket	60	8	Moist	High	DL+0.5LL	0.50c	6.0	7.00
P6009	Pocket	60	9	Moist	High	DL+0.5LL	0.50c	6.5	7.75
P6010	Pocket	60	10	Moist	High	DL+0.5LL	0.50c	7.0	8.50

Each simulation utilized one-half of a spandrel to minimize computational effort since loading and boundary conditions were symmetric, as illustrated in Fig. 6.16. The concrete solid was defined using 8-node brick elements with reduced integration. Short-term behavior of the concrete was represented by concrete damage plasticity model, described earlier in detail. Based on the concrete compressive strength of 6000 psi, other material properties of concrete were predicted as follows: E_c= 4,415x10^3 psi , ν= 0.15, ε_{cu}= 0.0038, f_t= 465 psi, G_f= 10 lb/in, and L_o=2.5 in. The characteristic length L_o is a parameter describing the typical dimension of concrete solids used in the model. Spandrel models were meshed using solid elements in a cubic shape with an

approximate side length of 2.5 in. (i.e., L_o=2.5).

Reinforcing steel was modeled with 3D truss elements, as shown in Fig. 6.16, and metal plasticity models. The elastic modulus for reinforcing steel, with the yielding strength of 60ksi, was taken as 29000 ksi. The elastic modulus of strands was taken 28,500 ksi. Prestressing force in strands (0.75×270=202.5 ksi) was applied as an initial condition to the truss elements representing the strands in the model. The transfer length (assumed to be 20 in.) of a strand was also modeled by gradually reducing the cross section of the strand at one end. Truss elements representing rebar and strands were embedded into the concrete solid and relative displacements between concrete and steel was fully restrained. Tension stiffening was defined in the concrete damage plasticity model and describes the interaction between concrete and steel (i.e., bond-slip and load transfer).

The spandrel simulations included reasonable boundary conditions for the tie-backs, deck-ties and bearing supports. Tie backs and deck ties were modeled as linear and horizontal springs with stiffness values of 600 and 10000 k/in, respectively. These values are defined in a previous study by the author [98] concerned with the influence of deck-tie and tie back stiffnesses on the behavior of spandrels. A simple support (vertical restraint only) was provided at one end of the spandrel whereas, at the mid-span, symmetric boundary conditions were introduced. Double-tee loads acting on the ledges of L-shaped spandrels and in the cut-outs of pocket spandrels were evaluated in three different load levels.

All spandrel beam models were analyzed with time-controlled static analysis procedure with large deformation formulation. After being deformed under the effect of prestressing force, each spandrel beam was first analyzed for the self-weight and double-tee loads (acting simultaneously), resulting in the instantaneous response of the spandrel. Next, by sustaining these loads for the period of two years and implementing the EMM analysis procedure, the time dependent response of the spandrel beam was obtained.

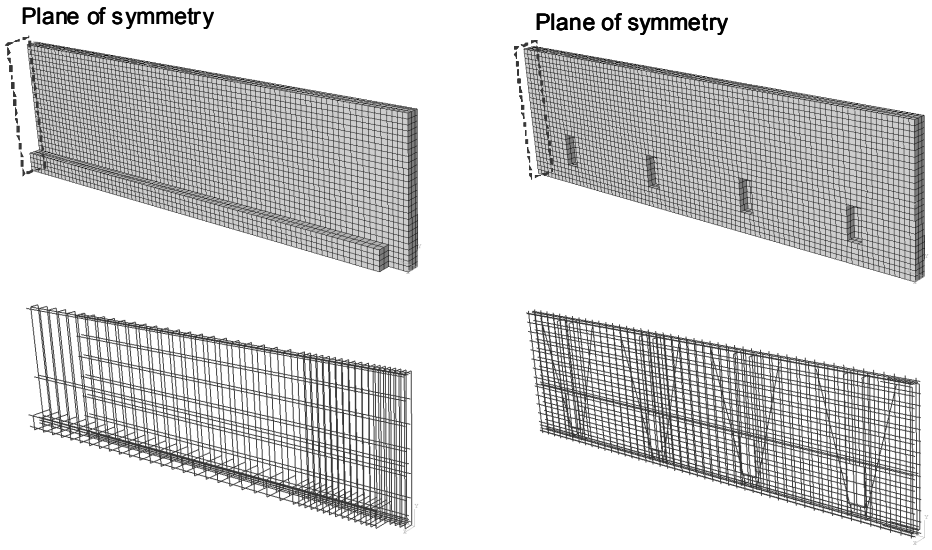

(a) L-shaped spandrel mesh and reinforcement

(b) Pocket spandrel mesh and reinforcement

Fig. 6.16. Finite element mesh and reinforcement details for 48-ft spandrels

6.9. Results of Finite Element Simulations

6.9.1. Deflections of spandrel beams

Precast and prestressed concrete spandrel beams exhibit complex deflection response including both vertical deflections and twisting deformations. Fig. 6.17 shows typical mid-span deflections of spandrels before and after the gravity loads are applied. The dashed lines represent the undeformed shape of the spandrel prior to the release of prestressing strands and the application of the beam self-weight. Under the effects of prestressing forces and the self-weight of the beam, the mid-span of the spandrel initially moves upward as shown in Fig. 6.17 (a). However, loading from the deck beams produces twisting and vertical deflections in the opposite direction of the initial deflections under the prestressing and self-weight, as seen in Fig. 6.17 (b). The bottom point moves laterally in the positive u direction, which is toward the outer face of the spandrel. It is noted that the spandrel is laterally restrained by deck-ties located at the mid-height level. The deflection of spandrel beams requires definition of the reference position by the totally undeformed shape indicated by dashed lines or the shape deformed

by the prestressing and self-weight in Fig. 6.17 (a). In this study dashed lines representing the position of spandrel prior to the release of prestressing strands are considered as reference.

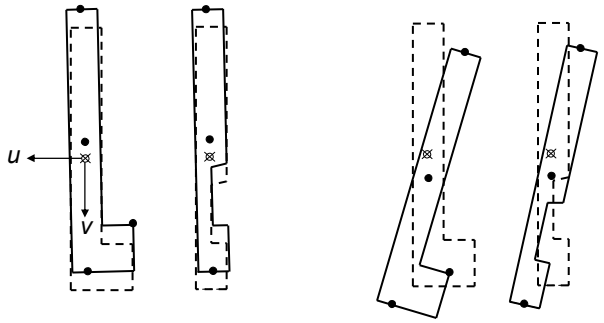

Fig. 6.17. Deformed shapes of spandrel cross-sections

Fig. 6.18 shows the results from finite elements (FE) analysis for baseline model L6008 (L-shape, 60-ft long, 8-in. wide). Time-dependent deflections of various locations (i.e., top, bottom, middle and ledge, see Fig. 6.17) in the mid-span cross section are presented. Results are plotted for both lateral *u* and vertical *v* deformations. Due to twisting of the spandrel, vertical displacements varied within the section. At the end of two years, the middle point moved 0.97 in. downward. The top and bottom points however had slightly different deformations, but the percentage of variation was less than 5 percent. The maximum vertical deflection was computed as 1.1 in. at the tip of the spandrel ledge (13 percent greater than the mid-point deflection). These deflections include contributions from prestressing (i.e., camber), self-weight, deck beam loads, and long-term effects (creep and shrinkage). Since the spandrel was laterally restrained around the mid-depth of the cross section, zero lateral displacements occurred at this location. The bottom and top points moved laterally in the similar amount (0.55 in.), but in the opposite directions. Computational results showed that the maximum displacement in the lateral direction is approximately one-half that in the vertical direction for the 60-ft L-shape spandrels as in the case of L6008.

The results of model P6008 (pocket, 60-ft long, 8-in wide) for a time period of two years are presented in Fig. 6.19. Similar to the deflection response of L6008, due to

twisting deformations, vertical deflections were different within the cross section at the mid-span. But such variations remained less than 5 percent. The maximum vertical deflections for the mid point were computed as 0.85-in. at the end of two years when the position of the beam before the release of the strands was used as a reference. Unlike L-shape spandrel L6008, lateral deflections at the top and bottom points in the mid-span cross section of pocket spandrel, P6008, were relatively small (u_{top}=0.11 in. and u_{bottom}=-0.11 in). This is partly due to the fact that the loading eccentricity in pocket spandrels is less than that in L-shaped spandrels. The effect of the eccentricity on the spandrel response will be discussed in detail later.

The pocket spandrel, P6008, initially moved upward 0.29 in. (v_{mid}=-0.29 in.) under prestressing forces and self-weight, as seen in Fig. 6.19 . After the application of instantaneous service loads (DL+0.5LL), the mid-span section deflected 0.52-in downward (v_{mid}=+0.23 in.). At the end of two years, the spandrel mid-span section had a final vertical position of v_{mid}=+0.85 in., indicating that the additional deflection due to concrete creep and shrinkage was around 0.63-in. Therefore, the multiplier λ for additional deflection due to long-term effects can be estimated as 1.22 (=0.63/0.52) for a time period of two years. Similar observations can be made for the L-shaped spandrel L6008; v_{mid}=-0.11 before loading, +0.29 after loading, +0.97 in. after two years, indicating that spandrel deflects 0.4 in. downward due to the instantaneous loads and 0.68 in. more due to long-term effects. Thus, the multiplier λ for additional deflection due to long-term effects can be estimated as 1.73 (=0.68/0.4).

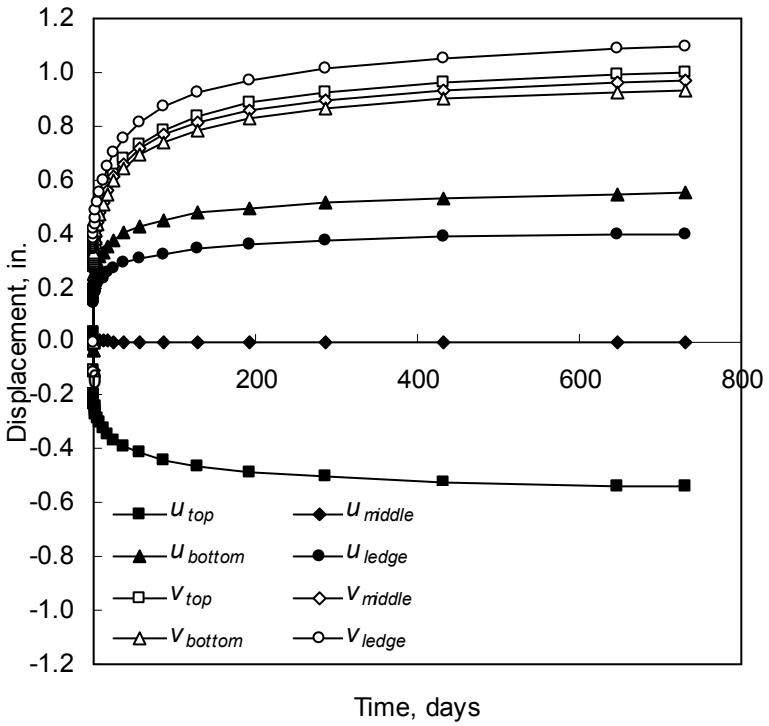

Fig. 6.18. Long-term deflections at the mid-span of the 60-ft-long and 8-in-wide L-shape spandrel (L6008)

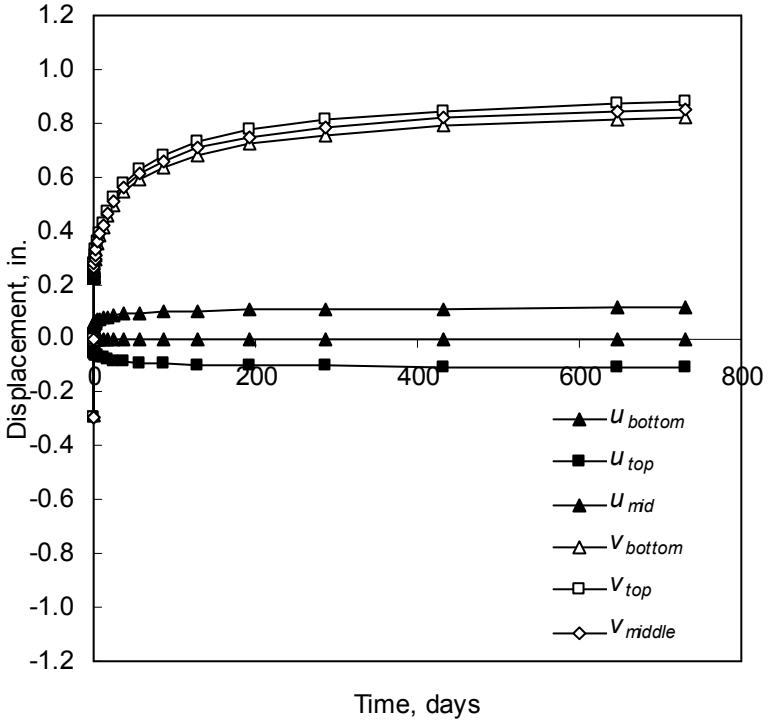

Fig. 6.19. Long-term deflections at the mid-span of the 60-ft-long and 8-in-wide pocket spandrel (P6008)

6.9.2. Geometric parameters: type, length and width

The effect of geometric characteristics such as spandrel type, length and width on the long-term deflections was studied in Fig. 6.20 and Fig. 6.21 for all of the baseline spandrel models listed in Table 6.5. Fig. 6.20 shows the vertical deflections computed at the mid-spans of these spandrels. As expected, the longer spandrels, 60-ft series, had larger long-term deflections than the 48-ft series. Interestingly, for the same magnitudes of prestressing force ($0.75f_{pu}$) and permanent loads (DL+0.5LL), L-shape spandrels experienced larger deflections than pocket-type spandrels, given that the pocket-type spandrels had smaller cross-sectional stiffnesses. For the 48-ft long spandrels, such deflection variations in different spandrel types were negligible. However, as seen in Fig. 6.20, with the increase in spandrel span length from 48 ft to 60 ft, the effect of spandrel type on the vertical deflections becomes significant.

Fig. 6.21 shows the long-term lateral deflection responses of baseline spandrels,

computed at the bottom of the mid-span cross-section. Spandrel type rather than spandrel length or width had the greatest influence on the lateral deflection response. Due to smaller eccentricities, lateral deflections in the pocket spandrels were significantly smaller than those in the L-shape spandrels. Regardless of the spandrel type or span length, long-term lateral deflections at the end of two years typically increased around 30-40 percent when the width of a spandrel decreased from 10 in to 8 in. For a certain spandrel type, the lateral deflections in 60-ft long spandrels were larger than those in the 48-ft series. This was partly due to the fact that because the short-term lateral deflections were larger for the longer spandrels, so were long-term deflections.

In order to define a long-term deflection amplification factor for a prestressed concrete member, a reference condition must be defined as noted earlier. Using the configuration of the spandrels before the strand release and self-weight application as the reference, amplification factors were computed. These amplification factors are tabulated in Table 6.6 for both lateral and vertical deflections for the baseline spandrel beams. The positions of certain points in the cross-section at mid-span were evaluated at three different times immediately after the release of strands (RL), immediately after the application of the permanent loads (ST) and at the end of two years (LT). At RL, the lateral deflections were negligible or small for all spandrels, whereas the vertical deflections varied and are not negligible. The short-term deflection is obtained by the total displacement from the point RL to the point ST. These displacements include the effects of permanent loads, but not strand release and self-weight. The long-term deflection is obtained by the total displacement from the point ST to the point LT. Therefore, the multiplier λ for additional deflection due to long-term effects is calculated by the ratio of long-term deflections to the short-term deflection, (LT-ST)/(ST-RL). Thus, the multipliers λ for the vertical long-term deflections ranged from 1.22 to 2.04. The multipliers λ for lateral deflections in L-shape spandrel ranged from 1.31 to 1.44, whereas those in pocket-type spandrels ranged from 2.37 to 2.91.

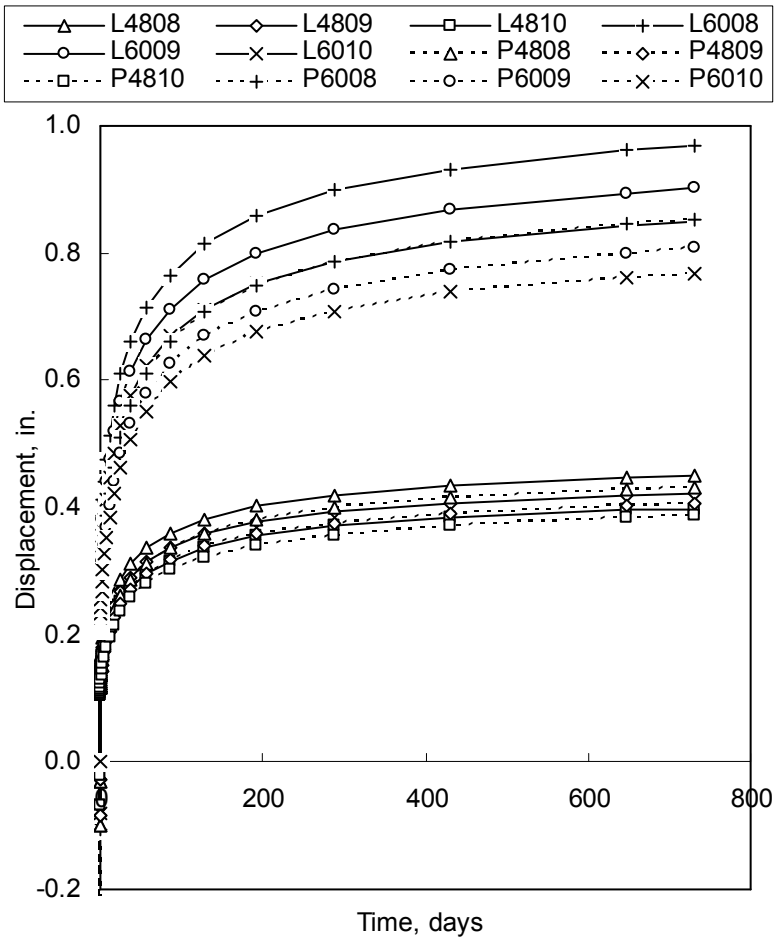

Fig. 6.20. Vertical deflections at the mid-spans of baseline spandrels

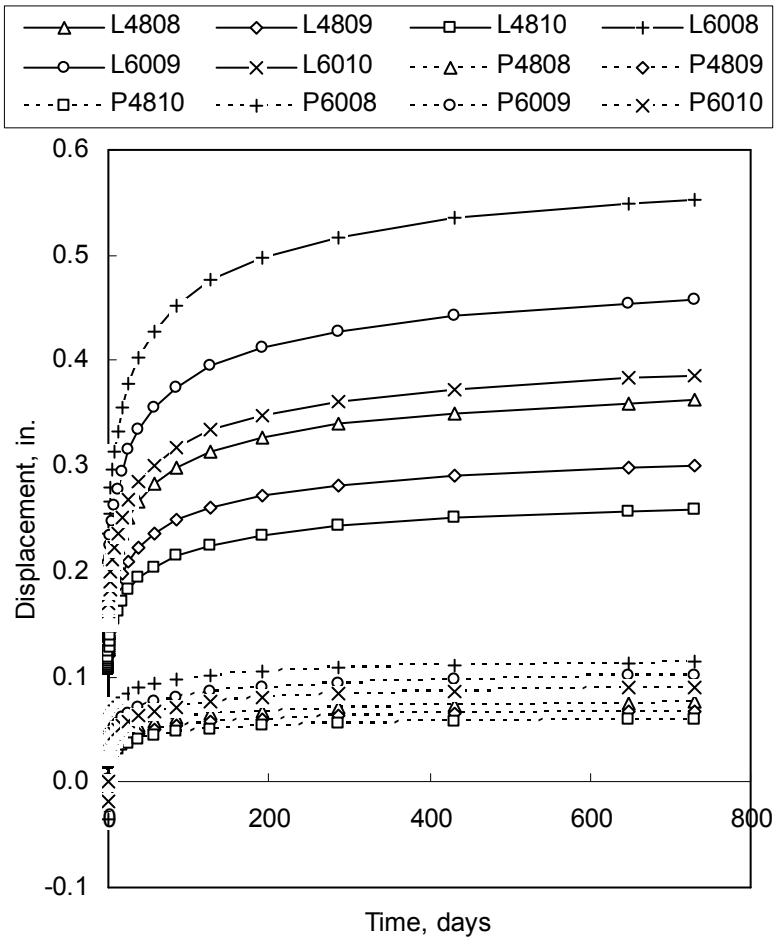

Fig. 6.21. Bottom lateral deflections at the mid-spans of baseline spandrels

Table 6.6. Long-term multiplier

Beam	Lateral position for the top				Lateral position for the bottom				Vertical position for the center			
Mark	RL	ST	LT	λ	RL	ST	LT	λ	RL	ST	LT	λ
-	in.	in.	in.	-	in.	in.	in.	-	in.	in.	in.	-
L4808	0.02	-0.13	-0.35	1.41	-0.02	0.14	0.36	1.37	-0.03	0.14	0.45	1.90
L4809	0.02	-0.11	-0.29	1.39	-0.01	0.12	0.30	1.35	-0.03	0.13	0.42	1.97
L4810	0.01	-0.10	-0.25	1.37	-0.01	0.11	0.26	1.31	-0.02	0.12	0.40	2.04
L6008	0.04	-0.20	-0.54	1.44	-0.04	0.21	0.55	1.41	-0.11	0.29	0.97	1.73
L6009	0.03	-0.17	-0.45	1.44	-0.02	0.18	0.46	1.40	-0.09	0.26	0.90	1.78
L6010	0.02	-0.14	-0.38	1.42	-0.02	0.15	0.39	1.38	-0.08	0.25	0.85	1.83
P4808	0.00	-0.02	-0.07	2.55	0.00	0.02	0.08	2.40	-0.10	0.12	0.43	1.45
P4809	0.00	-0.02	-0.06	2.64	0.00	0.02	0.07	2.47	-0.08	0.11	0.41	1.53
P4810	0.00	-0.02	-0.06	2.75	0.00	0.02	0.06	2.53	-0.07	0.11	0.39	1.61
P6008	-0.03	-0.05	-0.11	2.91	0.02	0.05	0.11	2.87	-0.29	0.23	0.85	1.22
P6009	0.00	-0.03	-0.10	2.38	0.00	0.03	0.10	2.37	-0.24	0.22	0.81	1.28
P6010	0.00	-0.03	-0.09	2.47	0.00	0.03	0.09	2.42	-0.21	0.21	0.77	1.35

RL= immediately after release of strands

ST= immediately after the application of permanent loads

LT= at the end of two years

λ= Long-term amplification factor =(LT-ST)/(ST-RL)

6.9.3. Concrete curing process

The previous sections have described in detail the deflection response of baseline spandrel models for a variety of geometric characteristics. However, the same concrete curing process (i.e., moist curing as shown in Table 6.5) was used in all baseline models. The present section discusses the variation of lateral deflection results when the steam curing of concrete is used. For this purpose, the creep and shrinkage behavior of concrete in L6008 and P6008 models was modified by introducing the steam-curing properties. Table 6.3 shows the correction factors for steam cured concrete, based on the "high level" of long-term effects (i.e., 1.01 and 0.97, respectively). For creep and shrinkage coefficients because the correction factors for steam curing are smaller than those for moist curing, the lateral deflections computed for the L-shape spandrel (L6008) are slightly smaller in the case of steam curing, as seen in Fig. 6.22. In addition to this, the effect of curing method on the lateral deflection response of the pocket-type spandrel is negligibly small.

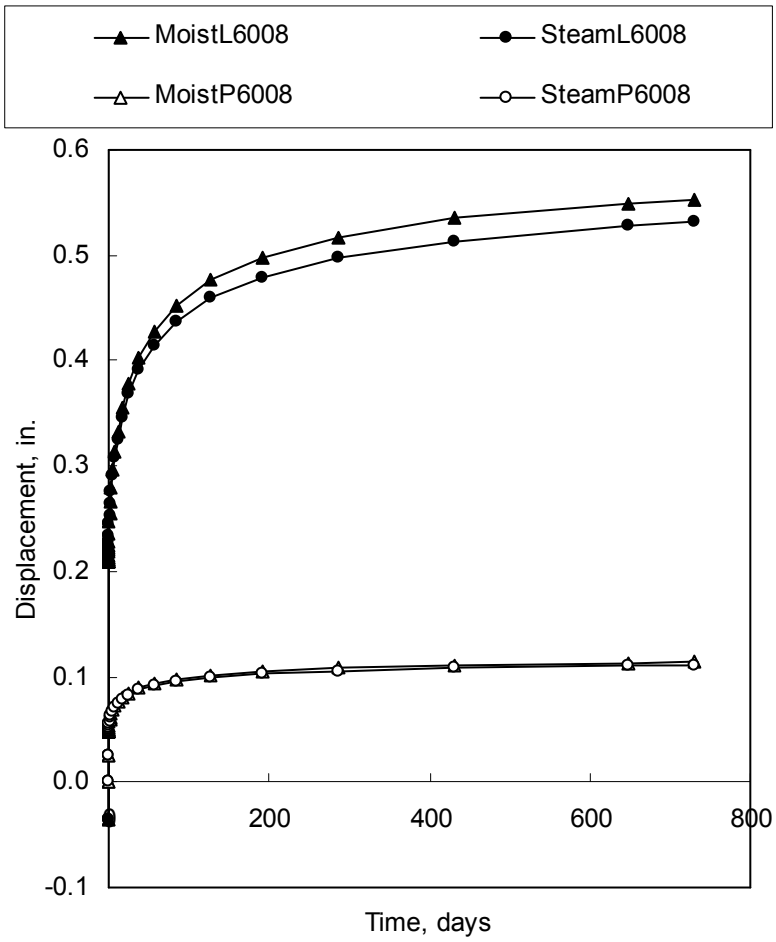

Fig. 6.22. Bottom lateral deflections at the mid-spans for different curing methods

6.9.4. Level of long-term effects

The baseline models relied on the "high level" of long-term effects, which is a conservative assumption. In this section, the variation of lateral deflection response of spandrels was evaluated for other levels of long-term effects. For this purpose, the spandrel models, L6008 and P6008, were modified by including low and medium levels of long-term effects. The lateral deflection results are plotted in Fig. 6.23. For both L-shape and pocket type spandrels, lateral deflections decreased 40 to 50 percent at the end of two years when the long-term level changed from high to low. When the level of long-term effects was changed from the high to medium level, the magnitude of long-term lateral deflections typically reduced 30 to 40 percent.

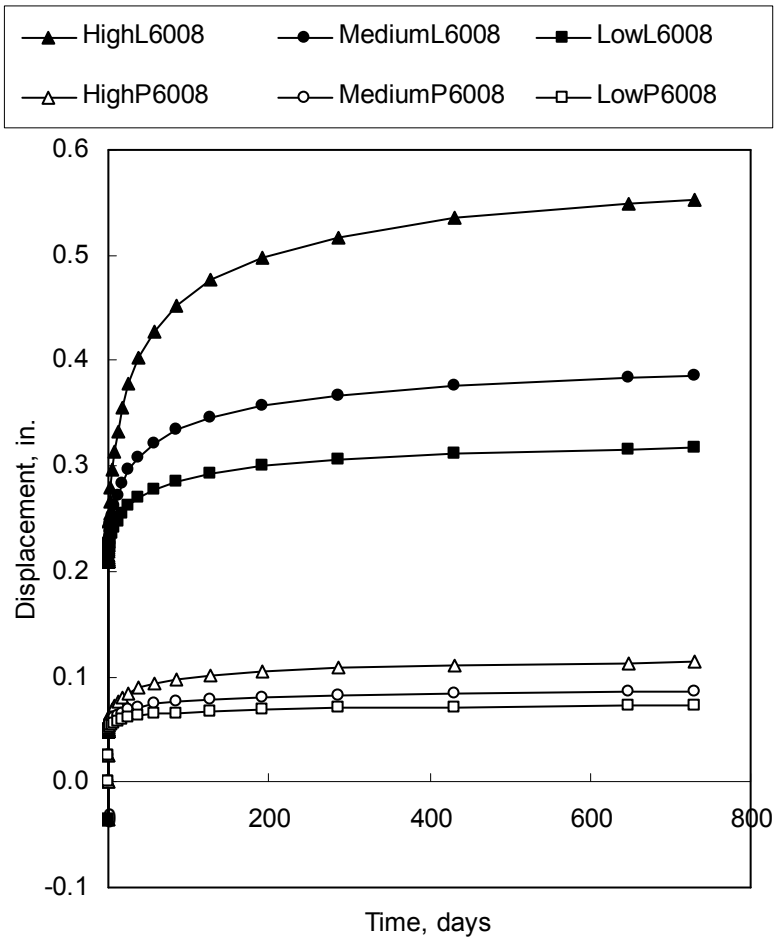

Fig. 6.23. Bottom lateral deflections at the mid-spans for different long-term effects

6.9.5. Magnitude of double-tee loads

All baseline models (Table 6.5) were subjected to the same instantaneous load, DL+0.5LL, sustained for two years in addition to spandrel self-weight and prestressing forces. In this section, lateral deflection responses of spandrels were investigated for different loading cases. In one of the loading cases, the full live load was sustained along with the dead load (i.e., DL+LL). In another loading case, only dead load was applied (i.e., DL). Fig. 6.24 shows the results from L6008 and P6008 models under the loading cases described. As expected, the long-term deflections increased when the sustained part of live load changed from 50 percent to 100 percent. The increment of lateral deflections at the end of two years was around 30 percent for L-shape spandrel, L6008, whereas the increment was approximately 10 percent for the pocket type spandrel model, P6008.

This result shows L-shape spandrels are more sensitive to a change on the magnitude of loads than pocket-type spandrels primarily because they typically have much large eccentricities of double tee loads than the pocket spandrels.

Fig. 6.24 also shows that there is a significant difference in the lateral deflection responses of L-shape and pocket spandrels when they are subjected to the self-weight and prestressing forces only. For such a loading case, the bottom of the L-shape spandrel moved toward the double-tees (negative deflection in Fig. 6.24) at the beginning of loading and the deflections continued increasing in the same direction due to the long-term effects. However, the direction of lateral displacements at the bottom of the pocket spandrel was not affected by the loading condition. This difference in responses arises from the fact that the L-shape spandrels are subjected to asymmetric bending under the prestressing forces.

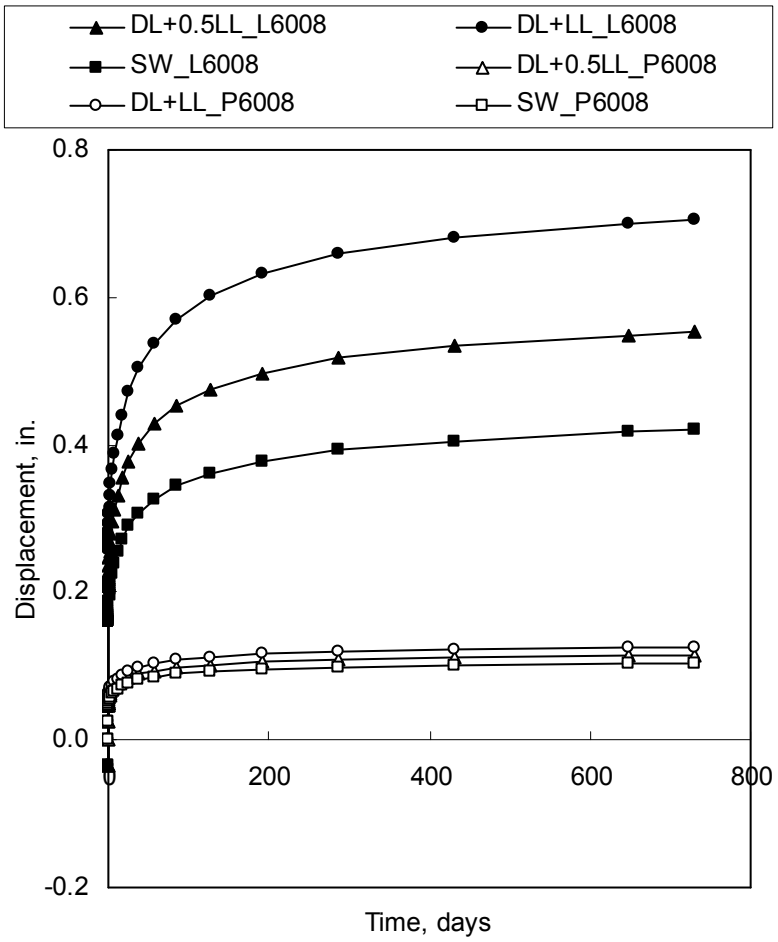

Fig. 6.24. Bottom lateral deflections at the mid-spans for different sustained loads

6.9.6. Loading eccentricity

Baseline spandrel models, listed in Table 6.5, were loaded at the half distance of their support widths, s=0.5c. The sensitivity of spandrel deflections to different loading eccentricities was also investigated by modifying the baseline models L6008 and P6008. Additional models were generated and analyzed for values of s equal to 0.75c and 1.0c. The support width s was equal to 8 in. for L-shape spandrels and 6 in. for 8-in wide pocket spandrels, as shown in Fig. 6.11. Assuming the eccentricity as the distance from the centerline of the spandrel web to the loading location, the value of the eccentricity for the loading at 0.5c is equal to 8 in for the 8-in wide L-shape spandrel (0.5b+0.5c=4+4=8 in.) and 1 in for the 8-in wide pocket spandrel (0.5b+0.5c-c=4+3-6=1 in.). Table 6.7 shows the values of eccentricities for other loading locations 0.75c and 1.0c. Shifting the

loading location from 0.5*c* to 1.0*c* increased the eccentricity 1.5 times in the L-shape spandrel and 4 times in the pocket-type spandrel.

Table 6.7. Loading eccentricities

Spandrel type	Web width *b* [in.]	Support width, c [in.]	Eccentricity e_c for		
			s=0.5*c*	*s*=0.75*c*	*s*=1.0*c*
L-shape	8	8	8	10	12
Pocket	8	6	1	2.5	4

The load point locations *s*=0.5*c* to 0.75*c* are representative of realistic loading. The loading at *s*=1.0*c* seems impractical, but corresponds to the most extreme case from the lateral deflection standpoint. Fig. 6.25 shows the lateral deflection results from the FE analyses of L6008 and P6008 models with various load point locations, *s*=0.5*c*, 0.75*c*, and 1.0*c*. Clearly, the pocket-type spandrels were more sensitive to the level of loading eccentricity than L-shape spandrels. The amount of eccentricity considered for the L-shape spandrels is always larger than that in the pocket spandrels. However, for the most extreme case 1.0*c*, the pocket spandrel exhibited larger short-term and long-term deflections than the L-shape spandrel. This was partly due to the fact that the pocket spandrels have less sectional stiffness. Similarly, the long-term vertical deflection responses for various loading eccentricities were plotted in Fig. 6.26. As expected, the variation of eccentricity changed the vertical deflections in the L-shape spandrels slightly, while the variation was negligibly small for the pocket spandrels.

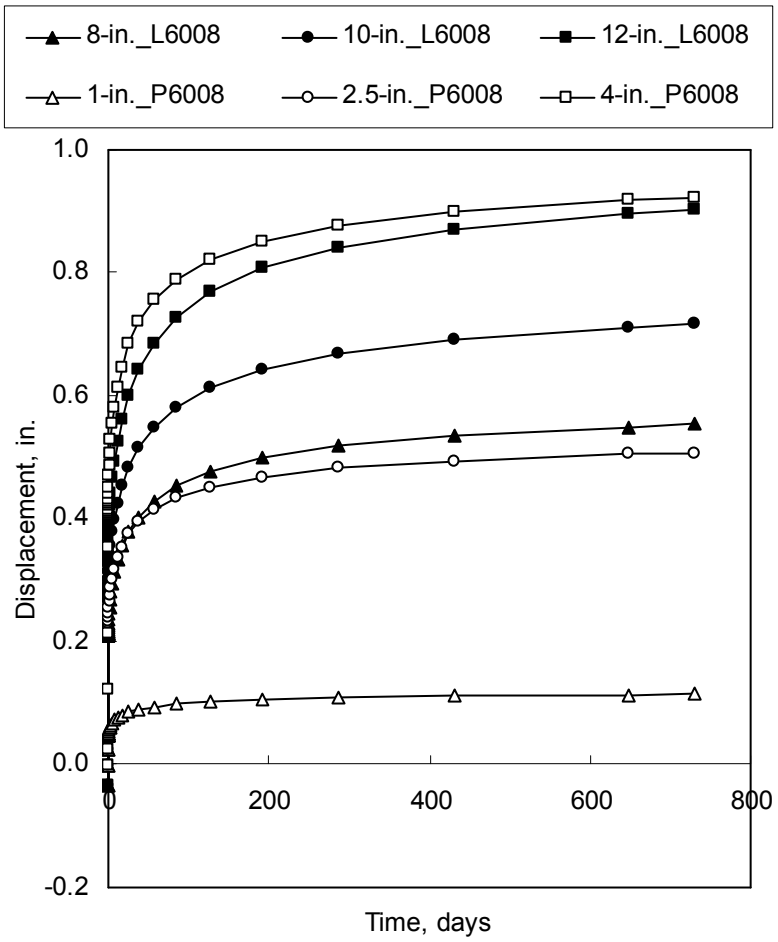

Fig. 6.25. Bottom lateral deflections at the mid-spans for various eccentricities e_c

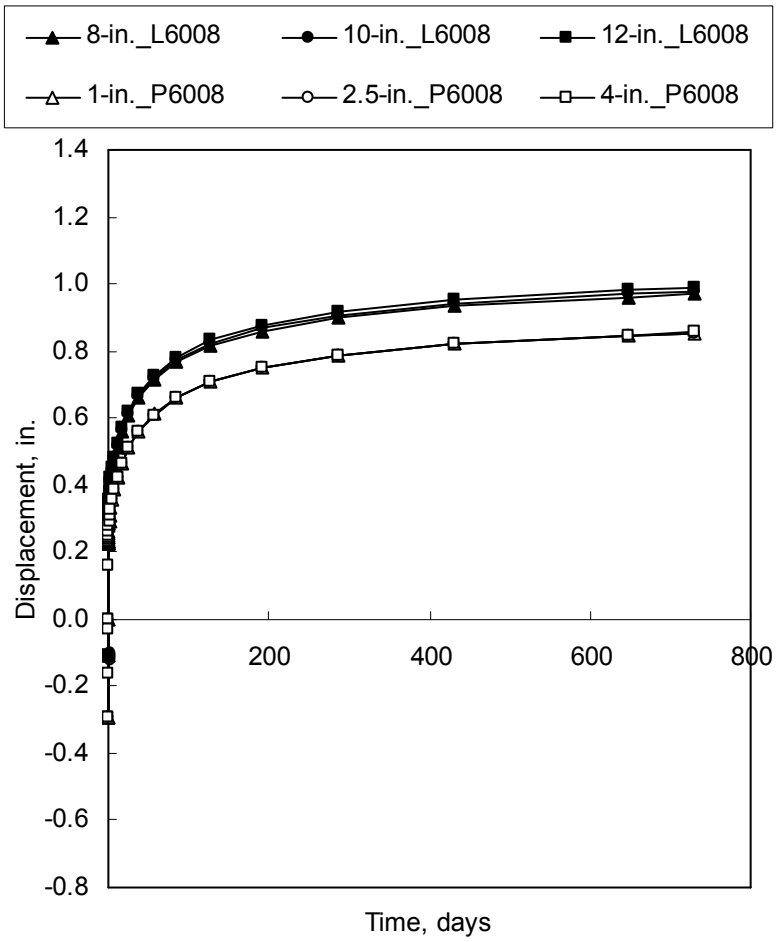

Fig. 6.26. Vertical deflections at the mid-spans for various eccentricities

6.10. Estimating Long-term Deflections

The *ACI 318-08* document provides a simple method for predicting additional deflections due to creep and shrinkage of flexural members. In this method, additional deflections can be determined by multiplying the instantaneous deflections by a factor λ unless a rigorous analysis method is implemented. This multiplier is defined as a function of another multiplier ξ and the compression reinforcement ratio ρ'. The values for multiplier ξ are tabulated for various durations of loading. The compression reinforcement reduces long-term deflections. However, for prestressed concrete spandrel beams, the effect of compression reinforcement can be ignored conservatively and hence the multiplier λ will be equal to ξ.

Using the procedure described in Section 6.9.2 in order to compute the long-term multipliers for the baseline spandrel beams at the end of two years, the multipliers for various durations of loading were obtained and plotted as seen in Fig. 6.27. The results indicate that the pocket type spandrels have larger long-term multipliers than L-shape spandrels. The ACI multiplier curve is closer to the set of multiplier curves of L-shape spandrels than those of pocket spandrels. For each type of spandrels, an idealized multiplier curve was established. Table 6.8 tabulates the values of the long-term multipliers from the ACI 318 document and proposed values for pocket and L-shape spandrels. Factoring these immediate deflections by the proposed long-term multipliers gives additional deflections due to long-term effects.

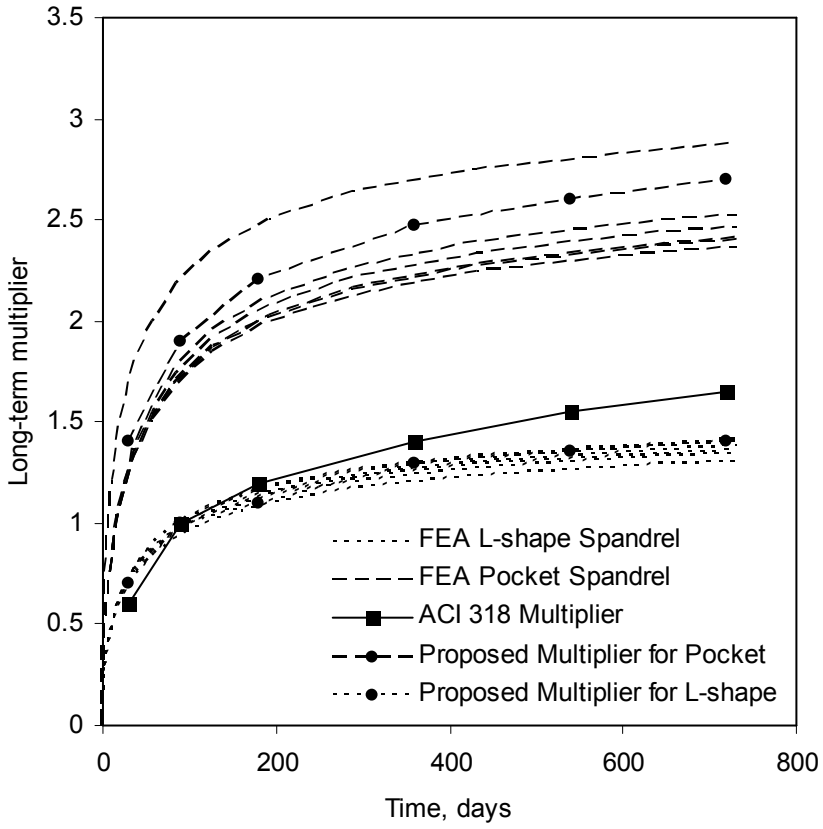

Fig. 6.27. Multiplier for additional deflections due to long-term effects

Table 6.8. ACI 318 and proposed multipliers λ

Month	ACI 318 values	Proposed values	
		L-shape	Pocket
1	0.60	0.70	1.40
3	1.00	1.00	1.90
6	1.20	1.10	2.20
12	1.40	1.30	2.47
18	1.55	1.35	2.60
24	1.65	1.40	2.70

6.11. Acceptability Criterion

In the pertinent literature or specifications, great effort has been expended for estimating and limiting vertical deflections in prestressed concrete spandrel beams. Maximum permissible vertical deflections have been specified to safeguard against the damage in supported or attached nonstructural elements (i.e., the limit of $L/360$ for immediate deflection due to live load). However, mention has not been made of the limitation of lateral deflections in prestressed concrete spandrel beams. For this reason, the long-term deflections computed in this study cannot be checked against a specified limit. However, the results obtained from finite element analyses of various spandrel beam models showed that the maximum total deflection (i.e., the sum of short-term and long-term deflections) is always less than $L/500$, above which the appearance of the spandrel beam might be impaired.

6.12. Conclusions

The use of high strength concrete and prestressing steel has allowed precasters to produce more material efficient precast and prestressed concrete structural members. This "next generation" of spandrels with thinner webs and spanning longer distances spandrels spanning longer distances has began to be utilized in the precast industry in the last few years due to their efficiency for reducing the number of columns required in a precast building. Comparing to the "current generation" of spandrels, such slender spandrels are, however, prone to larger deflections under service loads. Serviceability requirements rather than stress limitations may control the design in extreme cases.

Moreover, since spandrels are generally subjected to eccentric loads from deck beams, both vertical and lateral deflections ought to be considered for serviceability design checks. Thus, predicting long-term deflections for these members becomes necessary.

For this purpose, first, a series of pocket and L-shape spandrel beams were designed for various span lengths (48 and 60 ft) and widths, (8, 9 and 10 in.). Next, three-dimensional finite element models of these spandrels, including all reinforcement and prestressing strand details, were generated using commercial software ABAQUS. Creep and shrinkage behavior in concrete were defined using the ACI 209 model. Lateral deflections at the bottom and vertical deflections of the mid-span sections were computed after two years of sustained loads. Major findings were as follows:

- The top of the spandrel section usually moves laterally toward the double-tee beams, whereas the bottom moves outward (i.e., away from the double tees).
- The maximum lateral deflections in the next generation (60-ft long) spandrel beams at the end of two years for DL+0.5LL and the eccentricity of 0.5c was less than 1 in. Even though no limits have been specified for lateral deflections in the pertinent codes, the maximum lateral deflection is less than L/500 in all cases.
- Increasing the thickness of the spandrel from 8 in. to 10 in. reduced the long-term deflections around 30 to 40 percent.
- Concrete curing procedure (i.e., moist or steam curing) affected long-term lateral deflections, but only slightly.
- Ingoing from high to low levels of long-term effect reduced the long-term lateral deflections 40 to 50 percent.
- L-shape spandrels usually exhibit larger lateral deflections than pocket type spandrels provided that loading location is around 0.5*c* to 0.75*c*.
- Short-term and long-term lateral deflections in pocket type spandrel beams were more sensitive to the amount of loading eccentricity than those of L-shape spandrels.

This study pioneers in the evaluation of long-term behavior in precast/prestressed concrete, L-shape and pocket-type spandrels. Experimental study is necessary in order to verify time-dependent lateral deflection response of spandrel beams and the calculations

presented here.

6.13. Acknowledgement

The authors are grateful for Daniel P. Jenny Fellowship provided by Precast and Prestressed Concrete Institute.

6.14. Notation

E_c = modulus of elasticity of concrete

ε_c = concrete strain

ε_o = strain corresponding to the compressive strength of concrete

ε_p = strain at which the irreversible deformations initiates in concrete

ε_{cu} = concrete compressive strain at ultimate

ε_{tu} = ultimate tensile strain in concrete

$\varepsilon_c(t)$ = total strain in concrete at time t

ε_{ins} = instantaneous elastic strain in concrete

$\varepsilon_{cr}(t,t_o)$ = creep strain at time t due to loading at time t_o

$\varepsilon_{sh}(t)$ = shrinkage strain at time t

ε_{shu} = ultimate shrinkage strain

f'_c = compressive strength of concrete

f_r = modulus of rupture of concrete

f_t = tensile strength of concrete

f_{pu} = tensile strength of strand

σ_o = sustained stress

v_u = ultimate creep coefficient

$v(t)$ = creep coefficient at time t

γ_c = correction factor for creep

γ_{sh} = correction factor for shrinkage

u_{tu} = ultimate cracking displacement at which stress is equal to zero

G_f = fracture energy for concrete

L_o = characteristic crack length

$\alpha(t)$ = thermal expansion coefficient at time t

$T(t)$ = temperature at time t

E_{eff} =effective elastic modulus of concrete

P = concentrated load applied (i.e., double-tee loads)

L = span length of spandrel

b = web width of spandrel

h =depth of spandrel

c = support width on spandrel ledge (or pocket)

s = distance from inner face of spandrel web to loading point

e_c = eccentricity, distance from centerline of spandrel web to loading point

u =lateral displacement

v =vertical displacement

u_{middle} =lateral displacement at mid-depth of spandrel

v_{middle} =vertical displacement at mid-depth of spandrel

u_{top} =lateral displacement at top of spandrel

v_{top} =vertical displacement at top of spandrel

u_{bottom} =lateral displacement at bottom of spandrel

v_{botom} =vertical displacement at bottom of spandrel

λ = multiplier for additional deflection due to long-term effects

P = concentrated load applied (i.e., double-tee loads)

RL = position immediately after release of strands

ST = position immediately after the application of permanent loads

LT = position at the end of two years

ξ = time-dependent factor for sustained load

ρ' = compression reinforcement ratio

Bibliography

[1] SIMULIA. 2010. *ABAQUS version 6.10 Documentation, Theory Manual*. Dassault Systèmes Simulia Corp., Providence, RI.

[2] Lucier G, Rizkalla S, Zia P, and Klein G. 2007. "Precast concrete, L-shaped spandrels revisited: Full-scale tests." *PCI Journal*, 52(2): 62-76.

[3] Hassan T, Lucier G, Rizkalla S, Zia P. 2007. "Modeling of L-shaped, precast, prestressed concrete spandrels." *PCI Journal*, 52 (2):78-92.

[4] Raths, C. H. (1984). "Spandrel Beam Behavior and Design." *PCI Journal*, 29(3).

[5] Klein, G. J. (1986). *Design of Spandrel Beams*, Research Project No. 5, PCI, Chicago, IL.

[6] Lucier, G., Rizkalla, S., Zia, P., and Klein, G. (2007). "Precast concrete, L-shaped spandrels revisited: Full-scale tests." *PCI Journal*, 52(2).

[7] Hansell, W., and Winter, G. (1959). "Lateral Stability of Reinforced Concrete Beams." *ACI Journal, Proceedings*, 56(3).

[8] Sant, J. K., and Bletzacker, R. W. (1961). "Experimental Study of Lateral Stability of Reinforced Concrete Beams." *ACI Journal, Proceedings*, 58(6).

[9] Marshall, W. T. (1969). "A Survey of the Problem of Lateral Instability in Reinforced Concrete Beams." *Proceedings, Institution of Civil Engineers*, 43.

[10] Revathi, P. and Menon, D. (2006). "Estimation of Critical Buckling Moments in Slender Reinforced Concrete Beams." *ACI Structural Journal*, 103(2).

[11] Revathi, P. and Menon, D. (2007). "Slenderness Effects in Reinforced Concrete Beams." *ACI Structural Journal*, 104(4).

[12] Kalkan, I. (2009). *Lateral Torsional Buckling of Rectangular Reinforced Concrete Beams*, PhD Dissertation, Georgia Institute of Technology.

[13] Timoshenko, S. P. and Gere, J. M. (1961). *Theory of Elastic Stability*, McGraw-Hill, Inc., New York, NY.

[14] Bleich, F. (1952). *Buckling Strength of Metal Structures*, Mc-Graw-Hill, Inc., New York, NY.

[15] Galambos, T. V., Lin, F. J., and Johnston, B. G. (1996). *Basic Steel Design with LRFD*, Prentice-Hall, Upper Saddle River, New Jersey.

[16] Gaylord, E. H., Gaylord, C. N., and Stallmeyer, J. E. (1992). *Design of Steel Structures, 3rd Ed.*, Mc-Graw-Hill, Inc.

[17] Salmon, C. G., and Johnson, J. E. (1996). *Steel Structures, Design and Behavior*, Harper-Collins Publishing, Inc., New York, NY.

[18] Wan, G., Fleischman, R.B., and Zhang, D. (2011). "Effect of Spandrel Beam to Double Tee Connection on Flexure-Controlled Precast Diaphragms," *Journal of Structural Engineering, ASCE*, doi:10.1061/(ASCE)ST.1943-541X.0000426.

[19] SIMULIA. ABAQUS version 6.8 Documentation, Theory Manual. Dassault Systèmes Simulia Corp., Providence, RI. 2008.

[20] Park, R. and Paulay, T. (1975). *Reinforced Concrete Structures*, J. Wiley & Sons, Inc., New York, NY, 769 pp.

[21] SIMULIA. ABAQUS version 6.8. Dassault Systèmes Simulia Corp., Providence, RI. 2008.

[22] SIMULIA. ABAQUS version 6.8 Documentation, Theory Manual. Dassault Systèmes Simulia Corp., Providence, RI. 2008.

[23] Chen WF and Han DJ. Plasticity for structural engineers, NY: Springer-Verlag, 1988.

[24] Chen WF. Plasticity in reinforced concrete, FL: J.Ross, 2007.

[25] Lubliner J, Oliver J, Oller S, and Onate E. A plastic-damage model for concrete. Int J Solids and Struct 1989; 25(3): 299-326.

[26] Lee J and Fenves GL. A plastic-damage model for cyclic loading of concrete structures. J Engng Mech ASCE 1998; 124: 882-900.

[27] Gopalaratnam VS and Shah SP. Softening response of plain concrete in direct tension. ACI Journal 1985; 82(3):310-323.

[28] Janney, J.R., Hognestad, E. and McHenry, D. (1956). "Ultimate flexural strength of prestressed and conventionally reinforced concrete beams." Journal of the American Concrete Institute, 52, pp601-620.

[29] Kupfer, H., Hilsdorf, H.K., and Rusch, H. (1969). "Behavior of concrete under biaxial stresses."ACI Journal, 66, pp656-666.

[30] Charles HR. Spandrel beam behavior and design. PCI Journal 1984; 29(2): 62-131.

[31] Klein GJ. Design of spandrel beams. Chicago (IL): Precast/Prestressed Concrete Institute; 1986.

[32] Lucier G, Rizkalla S, Zia P, and Klein G. Precast concrete, L-shaped spandrels revisited: Full-scale tests. PCI Journal 2007; 52(2): 62-76.

[33] Hassan T, Lucier G, Rizkalla S, Zia P. Modeling of L-shaped, precast, prestressed concrete spandrels. PCI Journal 2007; 52 (2):78-92.

[34] Logan DR. L-spandrels: Can torsional distress be induced by eccentric vertical loading? PCI Journal 2007; 52(2): 46-61.

[35] Hansell W and Winter G. Lateral stability of reinforced concrete beams. J of the

American Conc Inst 1959; 31(3): 193-213.

[36] Massey C. Lateral instability of reinforced concrete beams under uniform bending. ACI Journal 1967; 64(3): 164-172.

[37] Revathi P and Menon D. Estimation of critical buckling moments in slender reinforced concrete beams. ACI Struct J 2006; 103(2): 296-303.

[38] Revathi P and Menon D. Slenderness effects in reinforced concrete beams. ACI Struct J 2007; 104(4): 412-419.

[39] Sant JK and Bletzacker RW. Experimental study of the lateral stability of reinforced concrete beams. ACI J Proceed 1961; 58(12): 713-736.

[40] Kofod-Olsen M and Nielsen MP. Lateral stability of reinforced concrete beams. The Danish Soc for Struct Sci and Engng 1997; 68(4): 115-146.

[41] ABAQUS Version 6.6 Documentation: Hibbitt, Karlsson and Sorensen, Inc, 2006.

[42] ACI 318. Building code requirements for structural concrete (ACI 318-08). Farmington Hills (MI): American Concrete Institute; 2008.

[43] Cook RD, Malkus DS, Plesha ME, and Witt RJ. Concept and applications of finite element analysis, fourth edition, NY: John Wiley & Sons, Inc, 2002.

[44] Chen WF and Han DJ. Plasticity for structural engineers, NY: Springer-Verlag, 1988.

[45] Chen WF. Plasticity in reinforced concrete, FL: J.Ross, 2007.

[46] Lubliner J, Oliver J, Oller S, and Onate E. A plastic-damage model for concrete. Int J Solids and Struct 1989; 25(3): 299-326.

[47] Lee J and Fenves GL. A plastic-damage model for cyclic loading of concrete structures. J Engng Mech ASCE 1998; 124: 882-900.

[48] Lee J and Fenves GL. A plastic-damage concrete model for earthquake analysis of dams. Earthquake Engng Struct Dyn 1998; 27: 937-956.

[49] Marzouk H and Chen ZW. Fracture energy and tension properties of high-strength concrete. J of Materials in Civ Engng 1995; 7(2): 108-116.

[50] Nayal R and Rasheed HA. Tension stiffening model for concrete beams reinforced with steel and FRP bars. ASCE J of Materials in Civ Engng 2006; 18(6): 831-841.

[51] Gopalaratnam VS and Shah SP. Softening response of plain concrete in direct tension. ACI Journal 1985; 82(3):310-323.

[52] Grassl P. Modelling of dilation of concrete and its effect in triaxial compression. Finite Elements in Analysis and Design 2004; 40: 1021-1033.

[53] SIMULIA. ABAQUS version 6.8. Providence, RI: Dassault Systèmes Simulia Corp; 2008.

[54] SIMULIA. ABAQUS version 6.8 Documentation, Theory Manual. Dassault Systèmes Simulia Corp., Providence, RI. 2008.

[55] Wagoner RH and Chenot JL. Metal Forming Analysis. Cambridge University Press; 2005.

[56] Riks E. An incremental approach to the solution of snapping and buckling problems. International Journal of Solids and Structures 1979; 15: 529-551.

[57] Crisfield MA. A fast incremental/iteration solution procedure that handles snap-through. Computers and Structures 1981; 13: 55–62.

[58] Prinja NK and Shepherd D. Simulating structural collapse of a PWR containment. The 17th International Conference on Structural Mechanics in Reactor Technology 2003; H04-6.

[59] Thevendran V, Chen S, Shanmugam NE and Richard Liew JY. Nonlinear analysis of steel-concrete composite beams curved in plan. Finite Elements in Analysis and Design 1999; 32: 125-139.

[60] Bathe KJ. Finite Element Procedures. New Jersey: Prentice Hall; 1996.

[61] Sun JS, Lee KH, and Lee HP. Comparison of implicit and explicit finite element methods for dynamic problems. Journal of Materials Processing Technology 2000; 105: 110-118.

[62] Kawakami M and Ito T. Nonlinear finite element analysis of prestressed concrete members using ADINA. Computers and Structures 2003; 81: 727-734

[63] Kennedy JB and Abdalla H. Static response of prestressed girders with openings. Journal of Structural Engineering (ASCE) 1992; 118(2): 488-504.

[64] Abdalla H and Kennedy JB. Dynamic analysis of prestressed concrete beams with openings. Journal of Structural Engineering (ASCE) 1995; 121(7): 1058-1068.

[65] Broo H, Lundgren K. and Engström B. Shear and torsion interaction in prestressed hollow core units. Magazine of Concrete Research 2005; 57(9): 521-533.

[66] Hassan T, Lucier G, Rizkalla S, and Zia P. Modeling of L-shaped, precast, prestressed concrete spandrels. Precast/Prestressed Concrete Institute Journal 2007; 52 (2): 78-92.

[67] Malm R. Shear cracks in concrete structures subjected to inplane stresses. Licentiate thesis. Sweden: Royal Institute of Technology; 2006.

[68] Chen WF. Plasticity in Reinforced Concrete. New York: McGraw-Hill; 1982.

[69] Kwak HG, Filippou FC. Finite element analysis of reinforced concrete structures under monotonic loads. Report no UCB/SEMM-90/14. California: Department of Civil Engineering, University of California Berkeley. 1990.

[70] Mercan B, Stolarski HK, Schultz AE. Finite element modeling of prestressed concrete spandrel beams. Submitted to Engineering Structures 2008.

[71] Lubliner J, Oliver J, Oller S, and Onate E. A plastic-damage model for concrete. International Journal of Solids and Structures 1989; 25(3): 299-326.

[72] Lee J and Fenves GL. A plastic-damage model for cyclic loading of concrete

structures. Journal of Engineering Mechanics (ASCE) 1998; 124: 882-900.

[73] Lee J and Fenves GL. A plastic-damage concrete model for earthquake analysis of dams. Earthquake Engineering and Structural Dynamics 1998; 27: 937-956.

[74] Gopalaratnam, V.S. and Shah, S.P. Softening response of plain concrete in direct tension. American Concrete Institute Journal 1985; 82(3): 310-323.

[75] Nayal R and Rasheed HA. Tension stiffening model for concrete beams reinforced with steel and FRP bars. Journal of Materials in Civil Engineering (ASCE) 2006; 18(6): 831-841.

[76] Hillerborg A, Mooder M and Peterson PE. Analysis of crack formation and crack growth in concrete by means of fracture mechanics and finite element. Cement and Concrete Research 1976; 6(6): 773-792.

[77] Marzouk H and Chen ZW. Fracture energy and tension properties of high-strength concrete. Journal of Materials in Civil Engineering (ASCE) 1995; 7(2): 108-116.

[78] Lucier G, Rizkalla S, Zia P, and Klein G. Precast concrete, L-shaped spandrels revisited: Full-scale tests. Precast/Prestressed Concrete Institute Journal 2007; 52(2): 62-76.

[79] ACI 318. Building code requirements for structural concrete (ACI 318-08). Farmington Hills (MI): American Concrete Institute; 2008.

[80] Raths, C. H. 1984. Spandrel Beam Behavior and Design. *PCI Journal*, Vol. 29, No. 3, Mar.-April.

[81] Klein, G. J. 1986. Design of Spandrel Beams. PCI Research Project No. 5, Chicago, IL.

[82] Cleland, N. C. 1984. Identification of Secondary Behavior in Combined Bending, Shear, and Torsion of Reinforced Concrete Ledger Beams. Ph.D. diss., University of Virginia.

[83] Lucier, G., Rizkalla, S., Zia, P., and Klein G. 2007. Precast concrete, L-shaped spandrels revisited: Full-scale tests. *PCI Journal*, 52(2): 62-76.

[84] Hassan, T, Lucier, G., Rizkalla, S., and Zia, P. 2007. Modeling of L-Shaped, Precast, Prestressed Concrete Spandrels. *PCI Journal*, 52(2): 78-92.

[85] Mercan, B., Schultz, A.E. and Stolarski, H.K. 2010. Finite Element Modeling of Prestressed Concrete Spandrel Beams. *Engineering Structures*, V. 32, Issue 9, September: 2804-2813.

[86] Allos, A.E. and Rashid, A.H. 1989. Prestressed Concrete Rectangular Beams Subjected to Sustained Torque. *ACI Journal*, V. 86, No. 4, July-August.

[87] Bennett, E.W. and Lee, K. H. 1985. Deflection of Partially Prestressed Beams under a Combination of Long-Time and Short-Time Loading. *ACI Journal*, Special Publication 86-8: 185-214.

[88] Branson, D.E. and Ozell, A.M. 1961. Camber in Prestressed Concrete Beams. *ACI*

Journal, V. 32, No. 12, June.

[89] Branson, D.E. and Shaikh, A.F. 1985. Deflection of Partially Prestressed Members. *ACI Journal*, Special Publication 86-14: 323-364.

[90] Gesund, H. 1962. Shrinkage and Creep Influence on Deflections and Moments of Reinforced Concrete Beams. *ACI Journal*, V.59, No. 5, May.

[91] Corley, W.G. and Sozen, M.A. 1966. Time-dependent Deflections of Reinforced Concrete Beams. *ACI Journal*, V. 63, No. 3, March.

[92] Christiansen, K. 1988. Eight-year Deformation Tests on Reinforced Concrete Beams. *Materials and Structures/ MatOriaux et Constructions*, 21: 172-178.

[93] Paulson, K.A., Nilson, A.H., and Kenneth, C.H. 1991. Long-term Deflection of High-strength Concrete Beams. ACI Materials Journal, V.88, No. 2, March-April.

[94] Alwis, W.A.M., Olorunnivo, A. and Ang, K.K. 1994. Long-term Deflections of RC Beams. *Journal of Structural Engineering,* Vol. 120, No. 7, July.

[95] Samra, R.M. 1997. Renewed Assessment of Creep and Shrinkage Effects in Reinforced Concrete Beams. *ACI Structural Journal*, V. 94, No. 6, November-December.

[96] Alwis, W.A.M. 1999. Long-term Deflection of RC Beams under Constant Loads. *Engineering Structures*, 21: 168–175.

[97] Gutiérrez, S.E., Cudmani, R.O., and Danesi, R.F. 1996. Time-Dependent Analysis of Reinforced and Prestressed Concrete Members. *ACI Structural Journal*, V. 93, No. 4, July-August.

[98] Mercan, B., Schultz, A.E., Stolarski, H.K., ?????? and Magaña, R. A. 2010. Elastic Solutions for Eccentrically Loaded, Slender, Precast and Prestressed Concrete Spandrel Beams. Submitted to ASCE Journal of Structural Engineering for publication.

[99] ACI Committee 318. 2008. Building Code Requirements for Structural Concrete (ACI 318-08) and Commentary. *American Concrete Institute*, Farmington Hills, MI.

[100] Prestressed/Precast Concrete (PCI). 2004. PCI Design Handbook, 6th Edition. *PCI Publication* MNL-120-04, Chicago, IL.

[101] SIMULIA. ABAQUS version 6.8 Documentation, Theory Manual. Dassault Systèmes Simulia Corp., Providence, RI. 2008.

[102] Neville, A.M. 1955. Theories of Creep in Concrete. *ACI Journal*, V. 27, No. 1.

[103] Lyse, I. 1960. Shrinkage and Creep of Concrete. *ACI Journal*, V.31, No. 8.

[104] Hansen, T.C. and Mattock, A.H. 1966. Influence of Size and Shape of Member on the Shrinkage and Creep of Concrete. *ACI Journal*, V. 63, No. 2, Feb.

[105] Hannant, D.J. 1969. Creep and Creep Recovery of Concrete Subjected to Multiaxial Compressive Stress. *ACI Journal*, Digest paper, May.

[106] Kawamura, M. 1969. Shrinkage Stresses in Concrete as a Viscoelastic Material.

ACI Journal, digest paper, December.

[107] Gopalakrishnan, K.S., Neville, A.M., and Ghali, A. 1970. A hypothesis on Mechanism of Creep of Concrete with Reference to Multiaxial Compression. *ACI Journal*, Title No. 67-3, January.

[108] Hope, B.B. 1975. A Model for the Creep of Concrete. *Cement and Concrete Research*, V. 5: 577-586.

[109] Ngap, A.S., M.M., and Nilson, A.H. 1981. Creep and Shrinkage of High Strength Concrete. *ACI Journal*, July-August.

[110] Smadi, M.M., Slate, F.O. and Nilson, A.H. 1987. Shrinkage and Creep of High-, Medium-, and Low-Strength Concretes, including overloads. *ACI Material Journal*, May-June.

[111] Bryant, A.H. and Vadhanavikkit, C. 1987. Creep, Shrinkage-size and Age at Loading Effects. *ACI Materials Journal*, March-April.

[112] Collins, T.M. 1988. Proportioning High-Strength Concrete to Control Creep and Shrinkage. ACI Materials Journal, V. 86, No.6, November-December.

[113] Kolver, K. 1995. Interdependence of Creep and Shrinkage for Concrete under Tension. *Journal of Materials in Civil Engineering*, V. 7, No. 2. , May.

[114] Mokhtarzadeh, A. and French, C. 2000. Time-Dependent Properties of High-Strength Concrete with Consideration for Precast Applications. *ACI Materials Journal*, V. 97, No. 3. May-June.

[115] Mokhtarzadeh, A. and French, C. 2000. Mechanical Properties of High-Strength Concrete with Consideration for Precast Applications. *ACI Materials Journal* , V. 97, No. 2, March-April.

[116] N. J. Gardner and M. J. Lockman. 2001. Design Provisions for Drying Shrinkage and Creep of Normal-Strength Concrete. *ACI Materials Journal*, V. 98, No. 2, March-April.

[117] Pons,G., Munoz,P. and Escadeillas, G. 2003. Determination of Concrete Total Deformations under Load as Function of Shrinkage Value. *ACI Materials Journal*, V. 100, No. 1, January-February.

[118] Bažant, Z.P. and Li, G.H. 2008. Comprehensive Database on Concrete Creep and Shrinkage. *ACI Materials Journal*, V.105, No.6, November-December.

[119] ACI Committee 209. 1997. Prediction of Creep, Shrinkage, and Temperature Effects in Concrete Structures (ACI 209R-92). *American Concrete Institute*, Farmington Hills, MI.

[120] CEB-FIB Model. 1991. CEB-FIB Model Code, Design Code. The Comité Euro-International du Béton, EPF CH 1015 Lausanne, Switzerland.

[121] Bažant, Z. P. and Murphy, P. 1995. Creep and shrinkage prediction model for analysis and design of concrete structures - model B3. *Materials and Structures*, 28: 357-365.

[122] Popovics, S. 1970. A review of stress strain relationships for concrete. *ACI Journal*, 67-14, March.

[123] Hillerborg, A., Modeer, M., and Petersson, P-E. 1976. Analysis of crack formation and crack growth in concrete by means of fracture mechanics and finite elements. *Cement and Concrete Research*, Vol. 6, pp. 773-782.

[124] Gopalarantnam, V. S. and Shah, S.P. 1985. Softening response of plain concrete in tension. *ACI Journal*, 82-27, March-April.

[125] Scott, R.H. and Beeby, A.W. 2005. Long-Term Tension-Stiffening Effects in Concrete. *ACI Structural Journal*, V. 102, No. 1, January-February.

[126] Gilbert, R.I. and Mickleborough, N.C. 1990. *Design of Prestressed Concrete*. Spon Press, Abingdon, Oxon.

[127] Branson, D.E. and Shaikh, A.F. 1967. *Favorable and unfavorable effects of non-tensioned steel in prestressed concrete beams*. PhD. Diss. Department of Civil Engineering, University of Iowa, Iowa City, June.